N_ d'ordre NNT : 2018-LYSEC008

THESE de DOCTORAT DE L'UNIVERSITE DE LYON opérée au sein de l'Ecole Centrale de Lyon

Ecole Doctorale N° 162
Mécanique Energétique Génie Civil Acoustique

Soutenue publiquement le 12/03/2018, par :

MENG HAN

Acoustic Properties of Novel Multifunctional Sandwich Structures and Porous Absorbing Materials

Devant le jury composé de :

Philippe Leclaire	Professeur	Université de Bourgogne Franche Comté - DRIVE EA1859 - 58000 Nevers, **Président**
Noureddine Atalla	Professeur	Dept. Of Mech. Eng. - Université de Sherbrooke, QC – Canada
Zichen Deng	Professeur	Northwestern Polytech Univ - Xian - 710072 Shaanxi - Chine
Shilin Xie	Professeur	Xi'An Jiao Tong Univ - Sch Aerosp - Xian 710049 - Chine
Feng Jin	Professeur	Xi'An Jiao Tong Univ - Sch Aerosp - Xian 710049 – Chine
Xiaoshan Cao	Professeur	Xi'An University of Technology - Xian 710049 - Chine
Olivier Bareille	Maître de Conférences	Laboratoire de Tribologie et Dynamique des Systèmes - Ecole centrale de Lyon
Didier Dragna	Maître de Conférences	Laboratoire de Mécanique des Fluides et Acoustique - Ecole centrale de Lyon

Sous la direction de :

Tianjian Lu	Professeur	Xi'An Jiao Tong Univ - MOE –KLMMS- Xian 710049 - Chine
Marie-Annick Galland	Professeur	Laboratoire de Mécanique des Fluides et Acoustique - Ecole centrale de Lyon
Mohamed Ichchou	Professeur	Laboratoire de Tribologie et Dynamique des Systèmes - Ecole centrale de Lyon

ABSTRACT

Implementation of acoustic materials is an effective and popular noise reduction method during propagation. Acoustic properties of novel multifunctional sandwich structures and porous absorbing materials are studied in the dissertation. The main contributions of the dissertation are given as,

Sandwich panels generally have excellent mechanical properties and good sound transmission loss (STL), but no sound absorption ability. Novel multifunctional sandwich structures are developed by integrating micro perforations and porous absorbing materials to the conventional structurally-efficient corrugated and honeycomb sandwich panels to achieve good SAC and STL at low frequencies.

Low frequency sound absorption and sound transmission loss (STL) of corrugated sandwich panels with different perforation configurations are evaluated both numerically and experimentally. Finite element (FE) models are constructed with considerations of acoustic-structure interactions and viscous and thermal energy dissipations inside the perforations. The validity of FE calculations is checked against experimental measurements with the tested samples provided by additive manufacturing. Compared with the classical corrugated sandwich panels without perforation, the perforated corrugated sandwich panels (PCSPs) with perforations in its face plate not only exhibits a higher SAC at low frequencies but also a better STL as a consequence of the enlarged SAC. The enlargement of SAC and STL should be attributed to the acoustical resonance induced by the micro perforations. It is also found that the PCSPs with perforations in both the face plates and corrugated cores have the lowest resonance frequencies of all the PCSPs. Besides, the acoustic properties of honeycomb sandwich panels with microperforated faceplate are also explored. An analytical model is presented with the assumption that displacements of the two faceplates are identical at frequencies below the faceplate resonance frequency. The analytical model is subsequently verified by finite element models and existing experimental results. Unlike classical honeycomb sandwich panels which are poor sound absorbers, perforated honeycomb sandwiches (PHSPs) lead to high SAC at low frequencies, which in turn brings about increment in the low frequency STL. Influences of core configuration are investigated by comparing PHSPs with different honeycomb core configurations.

In order to enlarge the SAC bandwidth of perforated sandwich panels, porous absorbing materials are added to the cores of novel perforated sandwich panels. FE models are set up to estimate the SAC and STL of perforated sandwich panels with porous materials. Results show that perforated sandwich panels with porous material can provide SAC with broader bandwidth and lower resonance frequency than that without porous materials. Whereas the peak values in the SAC and STL curves are reduced due to the weakened acoustical resonance by the porous materials.

Porous materials are popular sound absorbing materials with wideband sound absorption at high frequencies. To improve the sound absorption coefficient (SAC) of porous materials at low and middle frequencies, graded porous materials are introduced and optimized in the present dissertation. Two typical porous materials, sintered fibrous metals and semi-open cellular metals, are modeled and fabricated with geometrical parameter gradients. The anisotropic acoustic properties of sintered fibrous materials in the direction normal and parallel to their surface are obtained theoretically based on that of randomly distributed parallel fibers with additional shape factors introduced. Experiments were conducted to validate the theoretical model. The following parameter study shows that the sintered fibrous metals exhibit better sound absorption performance in the parallel direction than in the normal direction. Graded sintered fibrous materials are subsequently manufactured by stacking multilayer of homogeneous sintered fibrous materials, with their sound absorption estimated by the aforementioned analytical model. Distributions of porosity and fiber diameter in the graded sintered fibrous metals are optimized separately on the basis of the theoretical model. Optimization problems for either a sole frequency or a pre-specified frequency range are later solved using a genetic algorithm method. With regard to the graded semi-open cellular metals, an analytical is developed to evaluate their sound absorption properties. The pores in the semi open cellular metals are idealized as regularly spaced uniform spherical pores with pore openings at their joints. For validation, the model predictions are compared with existing experimental results, with good agreement achieved. Optimal design is conducted using the same optimizing method as that for graded sintered fibrous metals. Graded porous materials hold great potential for noise control applications particularly when stringent restriction is placed on the total volume and/or weight of sound absorbing material allowed to use.

Existing investigations of porous materials are mostly based on porous materials with smooth inner walls, it is expected that the SAC of porous materials can be improved by surface roughness on the inner walls. To account for influences of surface roughness on the sound absorption of porous materials, a theoretical model is proposed to evaluate the sound propagation performance of submillimeter sized micro pores containing micron sized surface mounted roughness elements based on the velocity and temperature distributions. Finite element models are then set up to validate the theoretical model. Results show that surface roughness can dramatically increase the sound energy consumed by viscous effect, which results in enlarged sound absorption.

KEY WORDS: Sound absorption Coefficient; Sound transmission loss; Microperforated sandwich panel; Graded porous materials; Surface roughness

RÉSUMÉ

La mise en œuvre de matériaux acoustiques est une méthode efficace et très utilisée pour réduire le bruit le long de sa propagation. Les propriétés acoustiques de nouvelles structures sandwich multifonctionnelles et de matériaux absorbants poreux sont étudiées dans la thèse. Les principales contributions de la thèse sont les suivantes:

Les panneaux sandwich ont généralement d'excellentes propriétés mécaniques et un bon indice de perte en transmission sonore (STL), mais aucune capacité d'absorption acoustique. De nouvelles structures sandwich multifonctionnelles sont développées en intégrant des micro-perforations et des matériaux absorbants poreux aux panneaux sandwich ondulés et en nid d'abeilles conventionnels, structurellement efficaces pour obtenir de bons STL et de bonnes absorptions en basses fréquences.

Le coefficient d'absorption acoustique (SAC) et la perte en transmission (STL) des panneaux sandwich ondulés sont évalués numériquement et expérimentalement en basse fréquence pour différentes configurations de perforations. Les modèles éléments finis (EF) sont construits en tenant compte des interactions vibro-acoustiques sur les structures et des dissipations d'énergie, visqueuse et thermique, à l'intérieur des perforations. La validité des calculs FE est vérifiée par des mesures expérimentales avec les échantillons testés obtenus par fabrication additive. Par rapport aux panneaux sandwich ondulés classiques sans perforation, les panneaux sandwich perforés (PCSPs) avec des perforations dans leur plaque avant présentent non seulement un SAC plus élevé aux basses fréquences, mais aussi un meilleur STL, qui en est la conséquence directe. L'élargissement des courbes des indices d'absorption et de transmission doit être attribué à la résonance acoustique induite par les micro-perforations. Il est également constaté que les PCSPs avec des perforations dans les plaques avant et les parois internes onduleés ont les fréquences de résonance les plus basses de tous les PCSPs. En outre, les performances acoustiques des panneaux sandwich en nid d'abeilles avec une plaque avant microperforée sont également examinées. Un modèle analytique est présenté avec l'hypothèse que les déplacements des deux plaques sont identiques aux fréquences inférieures à la fréquence de résonance des plaques. Le modèle analytique est ensuite validé par des modèles d'éléments finis et des résultats expérimentaux existants. Contrairement aux panneaux sandwich en nid d'abeilles classiques qui sont de piètres absorbeurs de bruit, les sandwichs en nid d'abeilles perforés (PHSPs) conduisent à un SAC élevé aux basses fréquences, ce qui entraîne en conséquence un incrément dans le STL basse fréquence. Les influences de la configuration du noyau sont étudiées en comparant les PHSPs avec différentes configurations de noyaux en nids d'abeilles.

Afin d'élargir la bande passante en absorption des panneaux sandwich perforés, des matériaux absorbants poreux sont ajoutés dans les noyaux des nouveaux panneaux sandwich perforés. Les modèles FE sont réalisés pour estimer le SAC et le STL de telles structures. Les résultats montrent que les panneaux sandwich perforés avec un matériau poreux peuvent conduire à une absorption plus large-bande et une fréquence de résonance inférieure à celle sans matériaux poreux. Cependant, les valeurs maximales dans les courbes SAC et STL sont réduites en raison de la résonance acoustique affaiblie par les matériaux poreux.

Les matériaux poreux sont utilisés habituellement pour absorber les bruits large-bande en hautes fréquences. Pour améliorer le coefficient d'absorption acoustique (SAC) des matériaux poreux à basse et moyenne fréquence, des matériaux poreux sont introduits et optimisés dans la présente thèse. Deux matériaux poreux typiques, les métaux fibreux frittés et les métaux cellulaires semi-ouverts, sont modélisés et fabriqués avec des gradients dans leurs paramètres géométriques. Les propriétés acoustiques anisotropes des matériaux fibreux frittés dans la direction normale et parallèle à leur surface sont théoriquement basées sur celle de fibres parallèles distribuées aléatoirement avec des facteurs de forme supplémentaires introduits. Des expériences ont été menées pour valider le modèle théorique. L'étude des paramètres suivante montre que les métaux fibreux frittés présentent une meilleure performance d'absorption acoustique dans la direction parallèle que dans la direction normale. Les matériaux fibreux frittés à gradient sont ensuite fabriqués en empilant une multicouche de matériaux fibreux frittés homogènes, leur absorption acoustique étant estimée par le modèle analytique susmentionné. Les distributions de la porosité et du diamètre des fibres dans les métaux fibreux frittés gradués sont optimisées séparément sur la base du modèle théorique. Les problèmes d'optimisation pour une fréquence unique ou une gamme de fréquence pré-spécifiée sont résolus ensuite en utilisant une méthode d'algorithme génétique. En ce qui concerne les métaux cellulaires semi-ouverts à gradient, une analyse est développée pour évaluer leurs propriétés d'absorption acoustique. Les pores dans les métaux cellulaires semi-ouverts sont modélisés par des pores sphériques uniformes régulièrement espacés avec des ouvertures de pores à leurs jonctions. Les prédictions du modèle sont comparées aux résultats expérimentaux existants et un bon accord est obtenu. La conception optimale est réalisée en utilisant la même méthode d'optimisation que pour les métaux fibreux frittés gradués. Les matériaux poreux à gradient offrent un grand potentiel pour les applications de contrôle du bruit, en particulier lorsqu'une contrainte forte est mise sur le volume total et/ou le poids du matériau absorbant insonorisant autorisé à utiliser.

Les études existantes sur les matériaux poreux sont principalement basées sur des matériaux poreux avec des parois intérieures lisses. Afin de tenir compte des influences de la rugosité de surface sur l'absorption acoustique des matériaux poreux, un modèle théorique est proposé pour évaluer les performances de propagation du son des micro pores submillimétriques contenant des éléments de rugosité montés en surface de taille micrométrique. Des modèles d'éléments finis sont ensuite mis en place pour valider le modèle théorique. Les résultats montrent que la rugosité de la surface peut augmenter considérablement l'énergie sonore dissipée par effet visqueux, ce qui entraîne un élargissement de la bande d’absorption.

MOTS CLÉS: Coefficient d'absorption acoustique; Perte en transmission; Panneau sandwich microperforé; Matériaux poreux à gradient; Rugosité de surface

Contents

1 Introduction

1.1 Background

Noise pollution has become one of the main pollutants that disrupt the natural rhythm of life. People are surrounded by noises from big machine of industries, activities of human beings, vehicles, even electrical appliances at home, etc. It has been difficult to escape from noises in our life today. Although the noise pollution is invisible, it has far reaching consequences. The adverse effects of noise pollution on the health of people and environment are quite severe. Noise pollution can result in damage to our ears, bring sleeping disorders, affect work efficiency. Excessive noise level even causes psychological problems, high blood pressure and cardiovascular diseases. Measures should be taken to prevent noise pollution. Implementation of the acoustic materials is an effective and easy method for sound attenuation during the propagation.

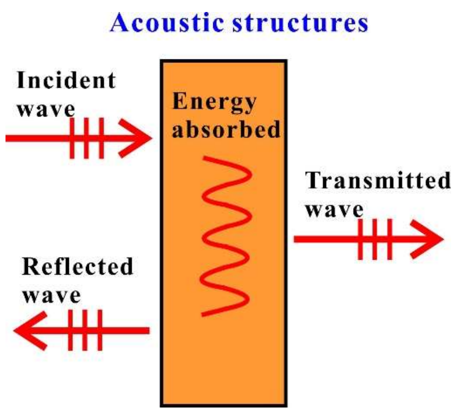

Fig. 1-1 Schematic of sound absorption and transmission loss by acoustic materials

Sound absorption and transmission loss are two important acoustic issues for investigators in the field of acoustic materials in the past decades. As shown in Fig. 1-1, sound absorption coefficient (SAC) means the proportion of consumed sound energy inside the acoustic materials to the total incident sound energy during the propagation. To improve the SAC, the sound absorbing materials should offer impedances match that of ambient medium to prevent reflection. Sound absorbing acoustic materials can be classified into two types, porous absorbing materials and resonant absorbing materials. Resonant absorbing materials are generally composed of micro pores or panels/membranes with resonant cavity, such as Helmholtz resonator, micro-perforated panel, membrane absorbers, et al. The resonant absorbing material can be analogous to a mechanical vibration system. The air in the small pores or the vibrating panel/membrane is equivalent to the mass, and the air in the cavity is equivalent to a spring. The resonant absorbing materials have high values of SAC at low frequencies but with a narrow bandwidth. The porous absorbing materials contain plenty of connected micro pores, channels, interstices, whose sizes are generally at the scale of micrometer to millimeter. The sound absorption inside the porous absorbing materials occurs due to the viscous and thermal effects of the saturated air. The viscous effect means that the viscosity of the fluid saturated in the porous materials changes the fluid motion with the tangible velocity being zero at the fluid-interface boundary, while the thermal effect represents that the expansion and compression of the fluid gives rise to the temperature fluctuations inside the pores. For elastic porous absorbing materials, the force mechanical oscillations of the elastic skeletons by the sound waves also consume part of the sound energy. The porous materials are wideband absorbing materials especially for sound absorbing at middle and high frequencies.

Sound transmission loss (STL) represents the ratio between the incident and transmitted sound energy (Fig. 1-1). It is noted that when the acoustic materials are backed by rigid walls, the STL doesn't exist. The acoustic materials for transmission loss are hence dense and heavy to reduce transmission and improve reflection. Sandwich panels are widely applied sound insulating materials. When sound waves impinge on the panels, a great deal of sound energy is reflected. The STL of the panels is related to their configurations, stiffness, boundary conditions, etc. For panels of infinite size, the low frequency STL is typically decided by the surface densities. Increasing the low frequency STL without increment of mass can be a challenging and important problem for both academic and industries.

1.1.1 Developing porous materials with higher SAC

Although the porous materials are wideband absorbing materials, there is still room for improvement especially in low frequency range where their sound absorption capability is relatively poor. Graded porous materials are manufactured by stacking multilayer homogeneous porous materials with different microstructures together. The graded porous material has attracted attention because it can have better impedance matching between the air and the materials and higher SAC with properly designed microstructures than homogeneous porous absorbing materials[1-3]. Therefore, it is meaningful to develop and optimize graded porous materials to obtain higher SAC.

Besides, even though plenty of investigations have been proposed for porous materials, the pores, tubes or interstices in the investigated porous materials have in principle smooth inner walls. It is expected that when their wall surfaces contain micro-scale structures (i.e., surface roughness), fluid flow and sound propagation in the tube will both be affected. SAC of micro pores or tubes with surface roughness deserves further research for developing better porous materials.

1.1.2 Designing and modelling of acoustic materials with both good SAC and STL

Even though the sound absorption is different from the transmission loss, both of them are important for noise reduction. Especially, acoustic materials with both good SAC and STL are required simultaneously for many applications, such as room acoustics. Nonetheless, despite sound absorbing materials are effective for sound absorption, they are incapable of transmission loss. On the contrary, the sound insulating materials can successfully applied for settling the issue of transmission loss, they are useless with regard to sound absorption.

Development of acoustic materials with both good SAC and STL at the same time is of great importance for industries as well as academics.

In recent years, a few researchers built composite panels by microperforated panels (MPP) and plates, the coupled MPP-air cavity-plate structures could have both effective SAC and STL[4-7]. The MPP layer and backed cavity constituted a resonating sound absorption system, while the backed plate acted as sound insulation barriers. These investigations proved the feasibility of developing acoustic structures with both good SAC and STL by combing sound absorbing and insulating materials. Sandwich structures made of multiple-layer panels and cores are the most appealing structures for STL, therefore it is interesting to design combinations with sandwich panels and sound absorbing materials, including microperforated structures, porous materials, *et al*.

1.2 Literature review

1.2.1 Porous and resonant sound absorbing materials

(1) Review of porous absorbing materials

The porous absorbing materials fall into 3 main types according to their micro configurations, foam and cellular materials, fibrous materials and granular materials[8]. Foam and cellular materials refer to porous materials with integrated frames and regular or fractal pores, such as open cell polyurethane and metal foams. The frames of fibrous materials are made of natural or synthetic fibers with diameters range from micrometer to millimeter. The granular materials consists of consolidated or unconsolidated particles and their internal voids.

The most popular theory for modelling porous materials is Biot's theory[9-12]. Biot proposed a theory for sound propagation in elastic porous materials that considered the dynamic behaviors of both the elastic solid phase and fluid phase. Many researchers used Biot's theory in their investigations of elastic porous materials. For instance, Allard *et al.* [13] adapted Biot's theory to interpreter the acoustic problems of foams. Khurana et al.[14] carried out a description of transversely isotropic porous materials in terms of transfer matrix method by Biot's theory for anisotropic materials. Many researchers used finite element models based on Biot's theory for the acoustic properties of single and multilayer poroelastic materials[15-19]. Deckers *et al.*[20] further presented a wave based method instead of finite element method to solve the vibro-acoustic problems of poroelastic materials on the basis of Biot's theory. Dazel *et al.*[21] and Becot and Jaouen[22] developed alternative formulations for the elastic porous materials by making modification to Biot's theory. Except from Biot's theory, other theories exist for the acoustic properties of elastic porous materials. Gao et al.[23,24] and Yamamoto[25] proposed homogeneous methods to reveal the relations between the macroscopic acoustic properties and microstructures of poroelastic materials, taking both the solid motion and visco-thermal dissipation of the fluid into consideration. Moreover, empirical models have also been derived and validated to determine the acoustic properties of several specific elastic porous materials[26,27].

Since the frame of porous materials can be regarded as motionless for most cases, researchers attached more importance to rigid frame porous materials than elastic porous materials[24,28]. The acoustic properties of rigid frame porous materials have been more extensively investigated than that of elastic porous materials. Models for rigid frame porous materials can be divide into two types, empirical models and phenomenological models. The most popular and widely used empirical model for rigid frame porous materials was proposed by Delany and Bazley[29], in which simple power-law functions for characteristic impedance and propagation constant were formulated by flow resistivity. As a modification, Miki[30] and Komatsu[31] gave new expressions for acoustic impedance and propagation constant based on Delany and Bazley's experimental data. Voronina[32-35] and Narang[36] proposed a series of empirical models for the acoustic properties of rigid frame and fibrous porous materials based on the porosity and pore diameters. Bies and Hansen[37] developed an empirical model to estimate the flow resistivity, acoustic impedance and sound absorption coefficient of polyester fibrous materials by the bulk density and fiber diameter. Empirical models are popular models with only a small number of parameters required. Whilst the empirical models as mentioned above may give accurate predictions in specific cases, they cannot be applicable for every common porous material. Compared with empirical models, phenomenological models have attracted even more attentions and applications. Phenomenological models are usually proposed on the basis of more parameters, and at least one of these parameters are related to the pore morphologies.

As a pioneer, Kirchhoff[38] proposed an exact solution for sound propagation in circular tubes of arbitrary diameter by considering the effects of both air viscosity and thermal conductivity. To provide more straightforward solutions, Zwikker and Kosten[39] restricted Kirchhoff's model to limited frequency and radius range and first treated the viscous effect and the thermal effect separately in their model. Attenborough[40] presented a theoretical model to estimate the acoustical properties of rigid absorbent soils and sands with five parameters involved. Attenborough's model gave good predictions for soils and sands with high flow resistivity at low frequencies. By approximating the relaxation characteristic, Wilson[41] developed a simple model for the complex density and bulk modulus of a porous medium with various pore shapes and fractal pore surfaces by four parameters. Johnson *et al*.[42] constructed an analytical model to evaluate the dynamic tortuosity of fluid-saturated porous media. Champoux and Allard[43] proposed formulae to calculate the dynamic bulk modulus of air-saturated porous media by introducing the concept of characteristic length. The famous Johnson-Champoux-Allard (JCA) model was formulated based on the Johnson *et al*.' model for the effective mass density and Champoux and Allard' model for the dynamic bulk modulus. Five parameters are needed in JCA model including the porosity, static flow resistivity, high frequency limit tortuosity, viscous and thermal characteristic lengths. The JCA model is a general model that applicable for all rigid frame porous materials. In addition to general phenomenological models, attempts have also been made to develop phenomenological models for specific porous materials, such as fibrous materials. For example, Tarnow[44,45] calculated the compressibility and dynamic resistivity by treating the fibrous material as array of periodically arranged parallel fibers, while Dupere *et al*.[46,47] modeled sound propagation both normal and parallel to array of parallel fibers and rigid spheres. Sun et al.[48] established that the model of Dupere *et al.* was suitable for sintered fibrous metal materials for high temperature applications. Kirby and Cumming[49] presented an improved model based on parallel fiber microstructure, targeting in particular sound absorbing properties at low frequencies.

Graded porous materials are investigated by a few researchers for the purpose of improving the sound absorption performance of porous materials[2,3,50]. Built upon a microstructural acoustic model, Dupere *et al.*[50] concluded that the sound absorption capability of cellular acoustic materials over a wide range of frequency would be substantially improved with graded porosity and pore size. Experimentally, Huang *et al.*[3] investigated the effect of pore size distribution in semi-open cellular metals on SAC and found that graded pore size led to enhanced sound absorption properties. Tang *et al.*[2] also proved that the low frequency SAC can be improved by graded metal fibrous materials by experiment.

Few studies exist on sound propagation in porous materials containing surface roughness elements. Built upon the classical approach of Johnson *et al.*[42], Cortis *et al.*[51] studied the high frequency behavior of fluid velocity patterns in both smooth and pore channels with wedge-shaped roughness elements, while Achdou and Avellaneda[52] analyzed the influence of pore roughness on the dynamic permeability of porous media. More recently, Ren *et al.*[53] fabricated an open-cell Al foam containing randomly distributed micrometer fibers on cell edges and experimentally investigated its acoustic properties. However, none of these investigations clearly reveals how sound propagation in the pores is affected by surface roughness.

(2) Review of resonant absorbing materials

Resonant absorbing materials have attracted much attention recently because of their prospects of low frequency SAC. Panel/membrane absorbers, Helmholtz absorbers and micro perforated panels are the three most mentioned resonant absorbers in both research and practical applications.

Panel/membrane absorbers consist of flexible panels/membranes with backed air cavity. The backed air cavity is usually partly or fully filled with porous absorbing materials. Panel/membrane absorbers are widely applied for low frequency SAC in constructions. Sakagami *et al.*[54-56] presented a system of theoretical study for infinite sized membrane absorbers. The acoustic properties of infinite sized membrane absorbers depend on the mass of the membrane/plate and the thickness of air cavity. Different from infinite sized absorbers, the finite sized absorbers are determined by both the mass and cavity as well as the shapes and boundary conditions of the panel/membranes. Ford and Cormick[57] first developed a theory for the acoustic impedance of clamped square panel absorbers, porous maetrials were introduced to the cavity. Arenas and Ugarte[58] theoretically and experimentally investigate sound absorbing of clamped circular plate for low frequency SAC. Thomas and Hurst[59] studied the acoustic performance of stretched circular membranes with partly filled fiberglass blanket and found the membrane absorbers effective for the SAC except at the anti-resonant frequencies. Wang *et al.*[60] used clamped panel absorbers to the sidewall of a duct to reduce the low frequency duct noise. Except from the clamped panel/membrane, simply supported elastic panel absorbers were modeled by a model analysis solution in Mechel's research[61]. Besides, Oldfield[62] adjusted the mounting conditions of a finite panel absorber with which the panel absorber could be approximately modeled by treating it as a piston oscillator.

The Helmholtz resonators are classical resonators that have been investigated for more than 100 years. A Helmholtz resonator is generally composed of an air cavity and connected pore opening whose size is much smaller than the air cavity. The Helmholtz resonators were first modeled by mass-spring system and lumped circuit[63]. The resonance frequencies of Helmholtz resonators were shown to be determined by the cross section areas and lengths of the orifices and volume of the cavities by the modeling theories. Ingard[64] and Ih[65] then modified the early models by adding end corrections to the acoustic impedance equations. Helmholtz resonators with cavities and orifices of simple and regular geometries were dealt with in early studied[64,66,67]. Alster[68], Chanaud[69,70] then compared Helmholtz resonators with different cavity and orifice geometries. In the later research, Tang[71], Li et al.[72-74], Cai *et al*.[75,76], and Lee *et al*.[77] tried to improve the low frequency acoustic properties of Helmholtz resonators by replacing the straight orifices and cavities by that with specially designed shapes, such as tapered, extended, spiral and T-shaped. The Helmholtz resonator has found wide applications in the design of new low frequencies sound attenuators, such as mufflers, sound filters, duct silencers, etc[78-83].

The most famous MPP is actually an example of distributed Helmholtz resonators sharing the same cavity. MPPs are usually comprised of plates with submillimeter pores and an air cavity. The sound absorption performance of the MPPs has been investigated, both theoretically and experimentally, by many investigators. Applying the method of electroacoustic analogy, Maa[84,85] first proposed an analysis model for the SAC of single and double MPPs. While Atalla and Sgard[86] attempted to evaluate the SAC of MPPs by employing rigid frame porous material models, Rao and Munjal[87] and Lee and Kwon[88] used an empirical impedance model to estimate the SAC of MPPs. The MPPs can be made of metal, plastic, plywood, acryl glass and sheet material, thus suitable for many environments including even severe conditions. For example, Asdrubali and Pispola[89] applied transparent MPPs as noise barriers, Li and Mechefske[90] experimentally investigated the application of MPPs in magnetic resonance imaging scanners, Sakagami *et al*.[91] presented investigations of MPP absorbers as room interior surface. Apart from the MPP with motionless panels, flexible panels with the consideration of panel vibration were also studied by many researchers. Sakagami *et al*.[92] introduce the vibration of the panels to Maa's eletroacoustic analogy model by dealing the panel vibration as a simple mass reactance. Kang and Fuches[93] and Sakagami *et al*.[94] used a more sophisticated model in which the panel vibration is counted by both mass reactance and vibrational resistance. The sound induced vibration of the panels were shown to reduce the resonance frequencies of the MPP. Toyoda *et al*.[95], Lee *et al*.[96,97] further proposed models for SAC of finite sized flexible MPPs and found the panel vibration absorption was indeed independent of the air-mass absorption of the MPPs and expanded the absorption bandwidth of the MPP.

1.2.2 Sandwich panels for sound transmission loss

The STL of a sandwich panel, for instance, has attracted numerous investigations. These investigations can be classified by the configuration of core inside the sandwich panel. The simplest sandwich panel is made of double walls with internal air layer. London[98], Antonio *et al.*[99], Chazot and Guyader[100], and Wang *et al.*[101] calculated the STL of both infinite and finite sized double walls separated by air gaps using analytical modeling and statistical energy analysis. To improve the sound insulation capacity, porous elastic materials are added to fill the gap between the two walls (faceplates), and the lined porous material can be either bounded or unbouned to the faceplates. Bolton *et al.*[102,103], Panneton and Atalla[16], Kang and Bolton[104], Liu and Daudin[105], Liu and He[106] presented theoretical and numerical investigations for the STL of double panels lined with porous materials, with the latter described using the Biot theory. They found that the highest STL can be obtained if the porous material is bounded to one faceplate and separated from the other one. Except from porous elastic materials, Chazot and Guyader[107], Doutres and Atalla[108] also conducted analytical investigations for acoustic properties of double panels with poro-granular materials and multilayer porous blankets, while Zielinski *et al.*[109] and Hu *et al.*[110] numerically investigated the sound insulation and transmission properties of active hybrid sandwich panels with porous absorbent material layers in either active or passive mode. Compared with double panels separated by air, sandwich panels filled with porous sound absorbing materials have better sound insulation. However, due to their intrinsically low stiffness, the low-frequency STL of sandwich panels filled with porous materials is yet sufficient. Therefore, many investigators resorted to sandwich panels cored with solid connecting structures to achieve higher stiffness and better low frequency STL, including sandwich panels with stiffened faceplates, corrugated and honeycomb cores. Mead[111], Wang *et al.*[112], Craik and Smith[113,114] proposed various theories to investigate the STL of double panels connected by parallel plates. Xin and Lu[115] and Shen *et al.*[116] extended the theories for double plates reinforced with parallel rib stiffeners to orthogonal rib stiffeners. With excellent mechanical efficiency, sandwich panels with honeycomb cores are widely used in applications, it is therefore natural that the STL of honeycomb sandwich panels has been extensively investigated[117-124]. Jung *et al.*[121] presented a theory to predict the STL of honeycomb sandwich by assuming the core is homogeneous orthotropic. Griese *et al.*[122] numerically calculated the STL performance of honeycomb sandwiches and analyzed the effect of core geometry. Zhou and Crocker[119] presented STL calculations of foam-filled honeycomb sandwich panels by statistical energy analysis. Rajaram *et al.*[123] investigated the effects of panel design parameters on the STL of honeycomb sandwiches. Tang *et al.*[120] presented a model to estimate the STL of cylindrical sandwich shell with honeycomb core. Sandwich panels with corrugated cores are also appealing alternatives in the transportation industry (e.g., high speed train) due to excellent mechanical performance with limited thickness, simple two-dimensional configuration, structural stability and easy manufacture procedure. Shen *et al.*[125] and Xin and Lu[126] presented analytical STL investigations of corrugated sandwich panels by modelling the corrugated core as translational and rotational springs. Bartolozzi *et al.*[127] calculated the STL of sandwich panels with sinusoidal corrugated cores by treating the corrugated cores as an equivalent homogenous material. Nonetheless, despite the success applications of sandwich panels for STL, they are incapable of sound absorption.

1.2.3 Composite structures for both sound transmission loss and sound absorption

Nowadays, to obtain lightweight structures with good absorption and insulation properties, combinations of MPPs and sandwich panels come into view of a few researchers. Perforated pores in the face plates of the sandwich panels can provide effective sound absorption as MPP layers, while the backed plates and core structures can act as sound insulation barriers. Dupont *et al*.[4] first investigated the acoustic properties of a MPP coupling with a flexible plate both analytically and experimentally. It was found that the coupled MPP-air cavity-plate system could increase the STL while maintaining a good SAC. To improve the STL at mid frequencies, Toyoda and Takahashi[7] subdivided the air cavity of the MPP-air cavity-plate system by inserting honeycomb structures to the air cavity. Bravo *et al*.[5,6] proposed a fully coupled modeling approach to calculate the SAC and STL of single or multi-layer MPPs and plates. It was shown that the SAC and STL at resonance frequencies were controlled by the relative velocities of air-frame and the MPP-back panel. Mu *et al*.[128] added MPP layer both to the source and the transmitted side of double leaf panels and found that the MPP layer weakened the mass-air-mass resonance.

The previous investigations prove that the combination of sandwich panels with MPPs and other sound absorbing materials might be a possible solution for obtaining both the sound transmission loss and sound absorption structures.

1.3 Objective and dissertation outline

Porous materials for higher SAC and composite structures for both good SAC and STL are developed, modeled and optimized in the present dissertation. The dissertation is organized as follows:

Chapter 2-4 developed theoretical models for two typical rigid frame porous materials, sintered fibrous metal and semi-open cellular metal. Graded porous materials are further explored and optimized on the basis of the two proposed models by adopting the genetic algorithm method. Experiments are conducted with both homogeneous and graded porous materials to validate the theoretical results.

Chapter 5 investigated the influence of surface roughness on the SAC of micro pores. Based on the calculated velocity and temperature fields, a theoretical model is built to evaluate the sound propagation performance in micro-pores containing periodical fibrous surface roughness elements. Finite element models are also developed to validate the theoretical model.

Chapter 6 and 7 proposed acoustic structures made of microperforations and honeycomb and corrugated sandwich panels to obtain both good SAC and STL at low frequencies. The porous materials are then filled in the cores of sandwich panels for the purpose of enlarging the bandwidth of SAC in Chapter 8.

Chapter 9 presents the conclusions of the present thesis and future work.

2 Anisotropic Acoustic Properties of Sintered Fibrous Metals

2.1 Introduction of sintered fibrous metals

Lightweight sintered fibrous metals are typically fabricated using metal fibers (stainless steel, FeCrAl, etc.) with micro-size diameters. The metal fibers are firstly cut into 10~50 mm long pieces, then arranged to form 2D (two-dimensional) random overlapping metal fiber felt (e.g., in a purposely-designed mould with external compressive force applied), and finally sintered at high temperature, followed by naturally cooling down in the furnace. Compared with conventional fibrous materials (polyester, wood, etc.), sintered metal fiber felts exhibit many advantages: simple manufacturing process, high porosity (e.g., 80% or higher) and sound absorption ability, good mechanical and thermal (e.g., conductive and convective heat transfer) properties, and high temperature resistance, etc. As a result, sintered fibrous metals are particularly applicable for noise control in extreme circumstances, such as acoustical liner of turbofan engine inlet[48,129-131].

Photographs of sintered fibrous metals are shown in Fig. 2-1. As the metal fibers having equal diameter randomly lie in parallel planes, the fibrous metal may be regarded as a transversely isotropic material. In the present study, for convenience, the plane parallel to all the fibers is referred to as the "fiber plane". With reference to Figs. 2-1(a) and (b), the acoustical properties of the sintered fibrous metal in the direction normal to the fiber plane are expected to be different from those in the direction parallel to it. Since the stiffness and density of the metal fibers are much larger than that of the fluid (air in the current study) saturated in the fibrous metal, the fibers are regarded as rigid bodies.

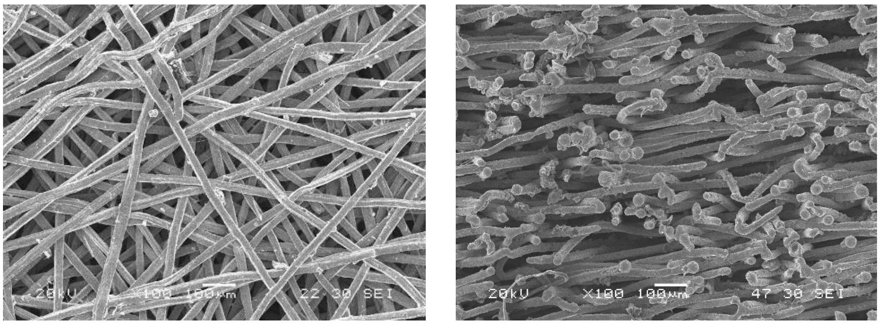

(a) (b)

Fig.2-1 Photographs of sintered fibrous metal: (a) surface parallel to fiber plane; (b) surface normal to fiber plane.

Although numerous studies have been carried out to explore the acoustical properties of rigid fibrous materials as mentioned in Chapter 1, none concerned the acoustic anisotropy of fibrous materials. A combined theoretical and experimental approach is employed to reveal the anisotropic acoustical properties of sintered fibrous metals in the present chapter.

2.2 Theoretical model for acoustic anisotropy in terms of sound absorption coefficient (SAC)

The viscous effect and thermal effect of the fibrous materials are represented by the dynamic density and effective bulk modulus respectively[39]. To quantify the SAC of the sintered fibrous metals, the dynamic density and effective bulk modulus should be calculated.

The dynamic densities of the sintered fibrous metal in different directions are estimated based on the array of randomly placed parallel fibers as shown in Fig. 2-2(a). The dash lines marked around the fibers are called Voronoi polygons, which represent the interaction of adjacent fibers in the parallel fiber array. For simplicity, each Voronoi polygon is approximated by a circle having the same area; see Fig. 2-2(b). The porosity of the parallel fiber array is identical to that of the considered sintered fibrous metal.

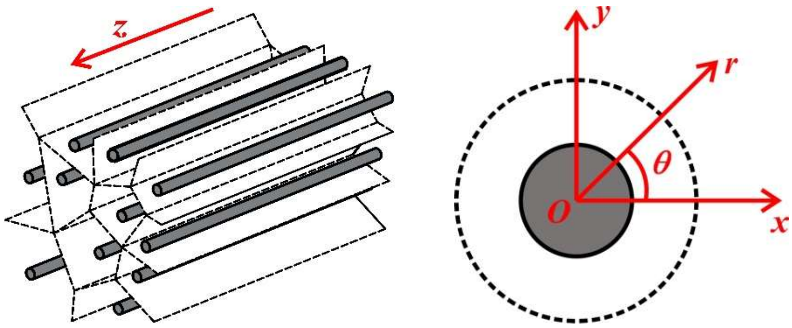

(a) (b)

Fig. 2-2 (a) Schematic illustration of parallel fiber array with Voronoi outer boundaries; (b) cross section of one cell with approximated circular outer boundary

Consider first sound propagating parallel to the parallel fiber array, namely, parallel to the z-direction of Fig. 2-2. Since the void space among these fibers is small, the viscosity of the saturated fluid is significant and should be taken into account in acoustic modeling. The fluid motion is governed by the viscous Navier-Stokes equation, as:

$$\nabla^2 u_z - \frac{i\omega\rho_0}{\eta} u_z = \frac{1}{\eta}\frac{\partial p}{\partial z} \tag{2-1}$$

where u_z is the fluid velocity in the z-direction, ω is the angular frequency, η denotes the dynamic viscosity of air, p is the sound pressure and ρ_0 is the air density. By approximating the Voronoi polygons by circles having the same area[45], the general solution for Eq. (2-1)can be written in the form[132]:

$$u_z(r,\omega) = A_0 Ke_0\left(\sqrt{\frac{\omega}{\nu}}r\right) + B_0 Be_0\left(\sqrt{\frac{\omega}{\nu}}r\right) - \frac{1}{i\rho\omega}\frac{\partial p}{\partial z} \tag{2-2}$$

where $Ke_m(x) = \mathrm{ker}_m(x) + i\mathrm{kei}_m(x)$, $Be_m(x) = \mathrm{ber}_m(x) + i\mathrm{bei}_m(x)$, ker_m, kei_m, ber_m, bei_m are the Kelvin functions, (r, θ) are the polar coordinates (Fig. 2-2), and A_0 and B_0 are unknown coefficients to be determined by applying relevant boundary conditions.

Due to the viscosity of the fluid, the velocity at the interface between the fluid and the fiber is zero:

$$u_z(r,\omega)\big|_{r=a} = 0 \tag{2-3}$$

where a is the fiber radius. Besides, no shear stresses exist on the outer boundaries of the fibers, therefore, for a circle with radius r_{out}, the boundary condition is[46]:

$$\left.\frac{\partial u_z(r,\omega)}{\partial r}\right|_{r=r_{out}} = 0 \tag{2-4}$$

Upon substitution of Eq. (2-2) into Eqs. (2-3) and (2-4), the coefficients A_0 and B_0 are obtained as:

$$A_0 = \frac{1}{Ke_0(R_0) - \frac{Ke_1(R_1)}{Be_1(R_1)} Be_0(R_0)} \frac{1}{\rho i\omega} \frac{\partial p}{\partial z} \tag{2-5}$$

$$B_0 = \frac{-1}{Ke_0(R_0) - \frac{Ke_1(R_1)}{Be_1(R_1)} Be_0(R_0)} \frac{Ke_1(R_1)}{Be_1(R_1)} \frac{1}{\rho i\omega} \frac{\partial p}{\partial z} \tag{2-6}$$

The velocity u_z is determined by substituting Eqs. (2-5) and (2-6) into Eq. (2-2), from which the mean velocity $\bar{u}_z$ is calculated as:

$$\bar{u}_z(r_{out},\omega) = \frac{1}{S}\iint_S u_z(r,\omega)\,dS = \frac{1}{\pi r_{out}^2 - \pi a^2}\int_a^{r_{out}} u_z(r,\omega)\,2\pi r dr \tag{2-7}$$

where $S = \pi r_{out}^2 - \pi a^2$ is the area occupied by the fluid in one cell.

For the parallel fiber array of Fig. 2-2(a), the Voronoi polygon with area S has a probability $p(S)dS$ in the interval between S and $S + dS$ [45]:

$$p(S) = \frac{1}{\bar{S}} \frac{\alpha^\alpha}{\Gamma(\alpha)} \left(\frac{S}{\bar{S}}\right)^{\alpha-1} \exp\left(-\alpha \frac{S}{\bar{S}}\right) \tag{2-8}$$

where $\Gamma(\alpha)$ is the gamma function with $\alpha = 3.61$, $\bar{S} = \dfrac{\pi a^2}{1-\Omega}$ is the mean area of the polygons for parallel fibers, and Ω is the porosity (i. e. the fraction of the volume of voids over the total volume) of the parallel fiber array. Therefore, with the random distribution of fibers accounted for, the mean velocity of fluid flow in the z-direction is

$$\bar{u}_z'(\omega) = \int_S \bar{u}_z(r_{out},\omega) p(S)\,dS = \int_a^\infty \bar{u}_z(r_{out},\omega) p\left(\pi r_{out}^2\right) 2\pi r_{out} dr_{out} \tag{2-9}$$

Finally, the longitudinal (z-direction) dynamic density of the parallel fiber array is obtained as:

$$\rho_{\parallel}(\omega) = \frac{-1}{i\omega}\frac{\partial p}{\partial z}\frac{1}{\bar{u}_z'(\omega)} \tag{2-10}$$

For sound propagating normal to the fiber axis (i.e., x-direction in Fig. 2-2), the fluid velocity is governed by the viscous Navier-Stokes equation as:

$$\nabla^2\mathbf{u}-\frac{i\omega\rho_0}{\eta}\mathbf{u}=\frac{1}{\eta}\frac{\partial p}{\partial x} \tag{2-11}$$

where $\mathbf{u}(r,\theta)$ is the fluid velocity vector, which has two components, u_r and u_θ, in the (r,θ) polar coordinates (Fig. 2-2). The velocity should be zero on the fiber surface, yielding:

$$\mathbf{u}(r,\theta)\big|_{r=a}=0 \tag{2-12}$$

Also, the vorticity should be zero on the outer boundary[46]:

$$\mathrm{curl}\mathbf{u}\big|_{r=r_{out}}=0 \tag{2-13}$$

From Eqs. (2-11), (2-12) and (2-13), the fluid velocity can be obtained as[46]:

$$\begin{aligned}u_r&=\left[\frac{Ke_1(R_0)-R_0Ke_1'(R_0)}{Ke_1(R_0)+R_0Ke_1'(R_0)}\left(\frac{a^2}{r^2}\right)+1-\frac{2(a/r)Ke_1\left(\sqrt{\frac{\omega\rho_0}{\eta}}r\right)}{Ke_1(R_0)+R_0Ke_1'(R_0)}\right]\frac{\partial p}{\partial x}\frac{-1}{i\omega\rho_0}\cos\theta e^{i\omega t}\\u_\theta&=\left[\frac{Ke_1(R_0)-R_0Ke_1'(R_0)}{Ke_1(R_0)+R_0Ke_1'(R_0)}\left(\frac{a^2}{r^2}\right)-1+\frac{2\sqrt{\frac{\omega\rho_0}{\eta}}aKe_1'\left(\sqrt{\frac{\omega\rho_0}{\eta}}r\right)}{Ke_1(R_0)+R_0Ke_1'(R_0)}\right]\frac{\partial p}{\partial x}\frac{-1}{i\omega\rho_0}\sin\theta e^{i\omega t}\end{aligned} \tag{2-14}$$

where $R_0=\sqrt{\frac{\omega\rho_0}{\eta}}a$. The mean velocity in the x-direction can hence be calculated as:

$$\bar{u}_x(r_{out},\omega)=\frac{1}{S}\iint_S u_x r dr d\theta=\frac{1}{\pi\left(r_{out}^2-a^2\right)}\int_0^{2\pi}\int_a^{r_{out}}\left(u_r\cos\theta-u_\theta\sin\theta\right)r dr d\theta \tag{2-15}$$

Further, given the random distribution of the parallel fibers, the mean velocity in the x-direction is given by:

$$\bar{u}_x'(\omega)=\int_S\bar{u}_x(r_{out},\omega)p(S)dS=\int_a^\infty\bar{u}_x(r_{out},\omega)p\left(\pi r_{out}^2\right)2\pi r_{out}dr_{out} \tag{2-16}$$

Finally, the transversal dynamic density of the parallel fiber array is calculated as:

$$\rho_\perp(\omega)=\frac{-1}{i\omega}\frac{\partial p}{\partial x}\frac{1}{\bar{u}_x'(\omega)} \tag{2-17}$$

Next, to calculate the effective bulk modulus of the sintered fibrous metal, the distribution of temperature in the parallel fiber array of Fig. 2-2 should be obtained. The temperature distribution is independent of sound propagation direction, governed by the thermal conduction equation as[133]:

$$k_t\nabla^2T-i\omega\rho_0c_pT=-i\omega p \tag{2-18}$$

where T is the temperature rise, k_t is the thermal conductivity of air, and c_p is the specific heat per unit mass at constant pressure.

With isothermal condition assumed, the temperature rise at the fiber surface is zero:

$$T(r,\omega)\big|_{r=a}=0 \tag{2-19}$$

The thermal flux should also be zero on the outer boundary. For a circular boundary with radius r_{out}, this becomes:

$$\left.\frac{\partial T(r,\omega)}{\partial r}\right|_{r=r_{out}}=0 \tag{2-20}$$

Due to the similarity between Eqs. (2-1) and (2-18), the solution of temperature rise can be expressed by using the velocity solution of Eq. (2-1). The mean velocity $\bar{u}_z'(\omega)$ can be expressed as $\bar{u}_z'(\omega)=\frac{-1}{\rho i\omega}\frac{\partial p}{\partial z}\varphi(\omega)$, then the mean temperature rise can be given by:

$$\bar{T}'(\omega)=\frac{p(\omega)}{\rho_0 c_p}\varphi(\mathrm{Pr}\,\omega) \tag{2-21}$$

where $\mathrm{Pr}=c_p\eta/k_t$ is the Prandtl number. Correspondingly, the effective bulk modulus is calculated as:

$$K_{eff}=\frac{p(\omega)}{\mathrm{d}\rho/\rho_0}=\frac{\gamma P_0}{\gamma-(\gamma-1)\dfrac{\rho_0 c_p}{p(\omega)}\bar{T}'(\omega)} \tag{2-22}$$

where γ is the specific heat ratio of the fluid, and P_0 is the static ambient pressure of air, and according to the state equation, $\mathrm{d}\rho/\rho_0=p/P_0-\bar{T}'(\omega)/T_0$, T_0 is the ambient temperature of air.

As shown in Fig. 2-1, when a sound wave propagates normal to the fiber plane, the sound is perpendicular to all the fibers in the fibrous metal. Therefore, the dynamic density of the fibrous metal may be approximated by the transversal dynamic density of the parallel fiber array, as:

$$\rho_N\approx\rho_\perp \tag{2-23}$$

In reality, as the fibers are not parallel but overlapped in the fibrous metal as shown in Fig. 2-1, a modified factor considering the microstructure of the fibrous material is added to the dynamic density, yielding:

$$\rho_N'\approx m_N\rho_N \tag{2-24}$$

where m_N is assumed equal to the square root of the tortuosity of the sintered fibrous metal in the direction normal to the fiber plane. Depending upon the microstructure of the fibrous metal, the tortuosity may be obtained by applying the self-consistent approximation method. Thus, in the direction normal to the fiber plane, the tortuosity is determined by[134]:

$$\tau_{\infty N}=\left.\left(\frac{c_0}{c_N(\omega)}\right)^2\right|_{\omega\to\infty} \tag{2-25}$$

where $c_N(\omega)$ is the sound speed in the fibrous metal in the direction normal to the fiber plane. This sound speed can be estimated by:

$$c_N(\omega)=\frac{\omega}{\mathrm{Re}\left(k_N(\omega)\right)} \tag{2-26}$$

where $k_N(\omega)$ is the complex wave number in the fibrous material, given by:

$$k_N(\omega)=\omega\sqrt{\frac{\rho'_N(\omega)}{K_{eff}(\omega)}} \tag{2-27}$$

Therefore, the tortuosity in the direction normal to the fiber plane can be written as:

$$\tau_{\infty N}=\mathrm{Re}\left(\frac{\rho'_N(\omega)}{K_{eff}(\omega)}\right)c_0^{\ 2}\Bigg|_{\omega\to\infty} \tag{2-28}$$

Equations (2-24) and (2-28) are solved by an iterative process. First, a value for $\tau_{\infty N}$ is chosen, for example $\tau_{\infty N}=1.5$, then the corresponding value of the dynamic mass density ρ'_N is computed by Eq. (2-24). Based on this value of ρ'_N, a new value of $\tau_{\infty N}$ is obtained by Eq. (2-28) from which a new value of ρ'_N is calculated. This iteration process is repeated until a stable value of $\tau_{\infty N}$ is obtained.

It has been established that the in-plane permeability of two-dimensional (2D) cross-plies and 2D randomly overlapping fiber structures is close to the averaged value of the transversal and longitudinal permeabilities of parallel fiber arrays[135,136]. As the dynamic density is inversely proportional to the permeability, in the present study, the averaged value of the transversal and longitudinal dynamic densities of the parallel fiber array is employed to approximate the dynamic density of the sintered fibrous material in the direction parallel to the fiber plane:

$$\rho_P\approx\frac{\rho_{\parallel}+\rho_{\perp}}{2} \tag{2-29}$$

Further, due to the complex architecture of the sintered fibrous metal (see Fig. 2-1), the concept of modified factor is applied to calculate more accurately the dynamic density in the direction parallel to the fiber plane, as:

$$\rho'_P\approx m_P\rho_P \tag{2-30}$$

where m_P is the modified factor that is equal to the square of tortuosity in the direction parallel to the fiber plane. Similar to the above iterative process for $\tau_{\infty N}$, m_P can also be determined using the self-consistent approximation approach.

Once the dynamic mass densities ρ'_P and ρ'_N as well as the effective bulk modulus K_{eff} are known, the wavenumbers (k_P, k_N) and the characteristic impedances (Z_P, Z_N) for sound propagation parallel and normal to the fiber plane can be obtained as:

$$Z_P=\sqrt{\rho'_P K_{eff}},\ Z_N=\sqrt{\rho'_N K_{eff}} \tag{2-31}$$

$$k_P=\omega\sqrt{\frac{\rho'_P}{K_{eff}}},\ k_N=\omega\sqrt{\frac{\rho'_N}{K_{eff}}} \tag{2-32}$$

Correspondingly, the sound speed and attenuation in the two directions are given by:

$$c_N = \frac{\omega}{\mathrm{Re}(k_N)},\ c_P = \frac{\omega}{\mathrm{Re}(k_P)}$$
$$\delta_N = -\mathrm{Im}(k_N),\ \delta_P = -\mathrm{Im}(k_P) \tag{2-33}$$

For a rigid-backed sintered fibrous metal sample with its surface normal to the fiber plane, its SAC for normal incident sound is:

$$\alpha_N = 1 - \left| \frac{Z_{sN} - \rho_0 c_0}{Z_{sN} + \rho_0 c_0} \right|^2 \tag{2-34}$$

where $Z_{sN} = -iZ_N \cot(k_N d_N)$ is the surface impedance of the sample and d_N is the thickness of the sample.

Similarly, for a rigid-backed sintered fibrous metal sample with its surface parallel to the fiber plane, its SAC for normal incident sound is:

$$\alpha_P = 1 - \left| \frac{Z_{sP} - \rho_0 c_0}{Z_{sP} + \rho_0 c_0} \right|^2 \tag{2-35}$$

where $Z_{sP} = -iZ_P \cot(k_P d_P)$ is the surface impedance of the sample and d_P is the thickness of the sample.

2.3 Experimental validation

2.3.1 Tested samples

The proposed theoretical model for sound propagation in sintered fibrous metals is validated against experimental measurement results. In total, four groups of sintered fibrous metal samples having the same porosity (90%) and fiber diameter ($50\ \mu\mathrm{m}$) are measured. From group to group, the thickness of the samples varies as 20 mm, 27 mm, 35 mm and 57 mm. As shown in Fig. 2-4, each group contains two different kinds of samples. The surface of one kind of sample is parallel to the fiber plane, while the surface of the other is normal to it. The physical parameters of the test samples are listed in Table 2-1. In the present study, the sintered fibrous metal is manufactured using randomly distributed stainless steel fibers of different length (10 mm~ 50 mm) but same diameter which are bonded to constitute a whole sample via furnace sintering. Thus the fiber diameter is known in the manufacturing process, while the porosity of the sample is obtained by comparing its density with that of the fibers.

Fig. 2-3 Test samples of sintered fibrous metal

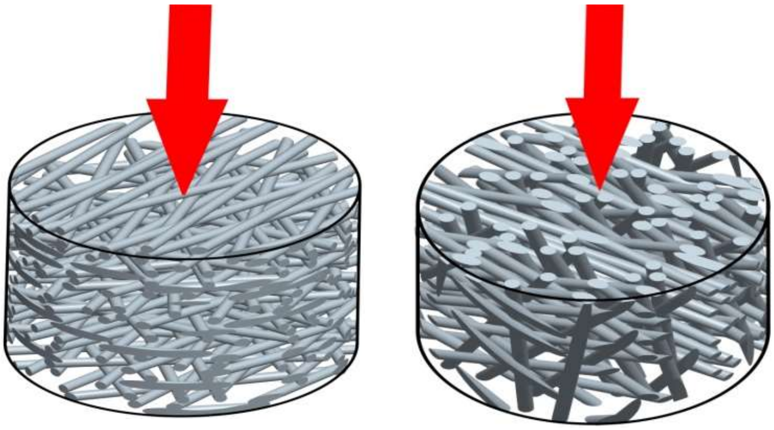

(a) (b)

Fig. 2-4 Schematic illustration of sintered fibrous metal: (a) sound incidence normal to fiber plane; (b) sound incidence parallel to fiber plane

Table 2-1 Physical parameters of sintered fibrous metal samples

Physical parameter	Value
Air density	$\rho_0 = 1.21\ \mathrm{kg/m^3}$
Specific ratio	$\gamma = 1.4$
Thermal conductivity of air	$k_t = 0.026\ \mathrm{W}/(\mathrm{m}\cdot\mathrm{K})$
Sound speed in air	$c = 343\ \mathrm{m/s}$
Dynamic viscosity	$\eta = 1.72\times10^{-5}\ \mathrm{Pa}\cdot\mathrm{s}$
Ambient pressure of air	$P_0 = 1.0132\times10^{5}\ \mathrm{Pa}$
Ambient temperature	$T_0 = 293.15\ \mathrm{K}$
Specific heat at constant pressure	$c_p = 1009\mathrm{J}/(\mathrm{kg}\cdot\mathrm{K})$
Fiber diameter	$a = 50\ \mu\mathrm{m}$
Porosity	Ω =90%

2.3.2 Experimental measurement

The SAC of sintered fibrous metal samples (Fig. 2-3) are measured in the B&K 4206 impedance tube by applying the transfer function method. As shown in Fig. 2-5, the tested sample is mounted at one end of the tube with the rigid back, while plane sound waves are generated at the other end of the impedance tube. The sound pressures in the impedance tube are measured by two wall-mounted microphones at two fixed locations. The reflection coefficient and sound absorption coefficient can then be calculated by the measured sound pressures[137].

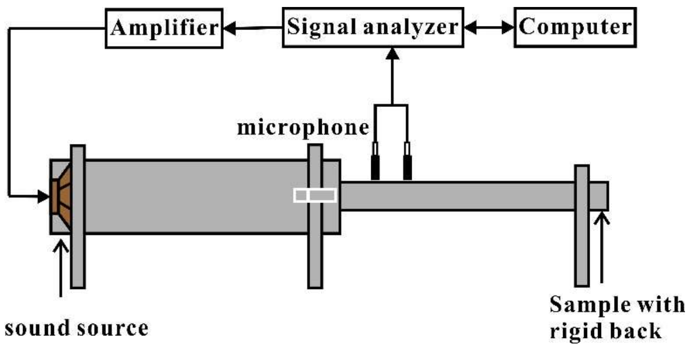

(a)

(b)

Fig. 2-5 (a) Schematic illustration and (b) Photograph of B & K impedance tube for sound absorption measurement

2.3.3 Comparison between theoretical and experimental results

The experimentally measured and theoretically predicted SACs are compared in Fig. 2-6 for all the four groups of sintered fibrous metal samples. The theoretical curves exhibit the same trends as those of the measured ones, capturing in particular all the peaks and dips. The discrepancies between the experimental and theoretical results may be attributed to the idealized handling of the connections between the fibers in the theoretical model. It can also be seen from Fig. 2-6 that the samples with incident surfaces parallel to the fiber plane always have a bigger SAC than that with incident surface normal to the fiber plane. In order to explain this trend, the sound speed and attenuation of sintered fibrous metals predicted using the theoretical model for sound incidence parallel and normal to the fiber plane are compared in Fig. 2-7.

As shown in Fig. 2-7, the speed of sound propagation parallel to the fiber plane is smaller than that normal to it at low frequencies, approaching the latter as the frequency exceeds about

1000 Hz. Correspondingly, within the considered frequency range, the attenuation of sound propagation parallel to the fiber plane is bigger than that normal to it. Together with the sound absorption comparison in Fig. 2-6, the present results demonstrate that the sound absorption ability of the sintered fibrous metal is better in the direction parallel to the fiber plane than that in the direction normal to it.

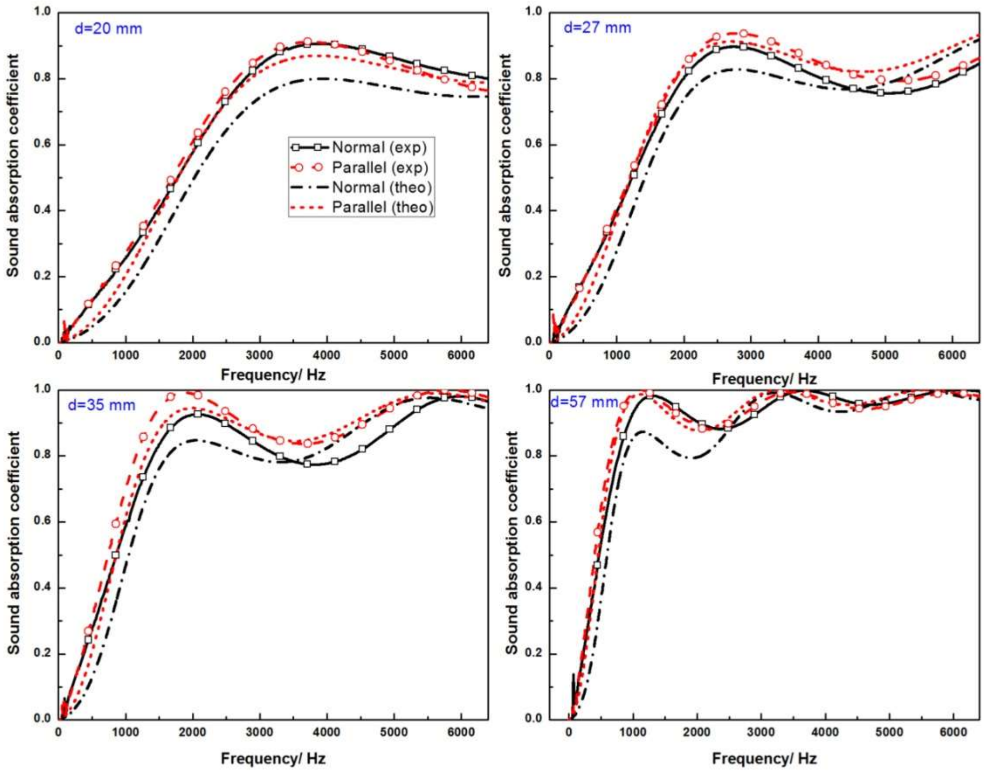

Fig. 2-6 Comparison between experimental measurements and model predictions for SAC of rigid-backed sintered fibrous stainless steel samples having different thicknesses

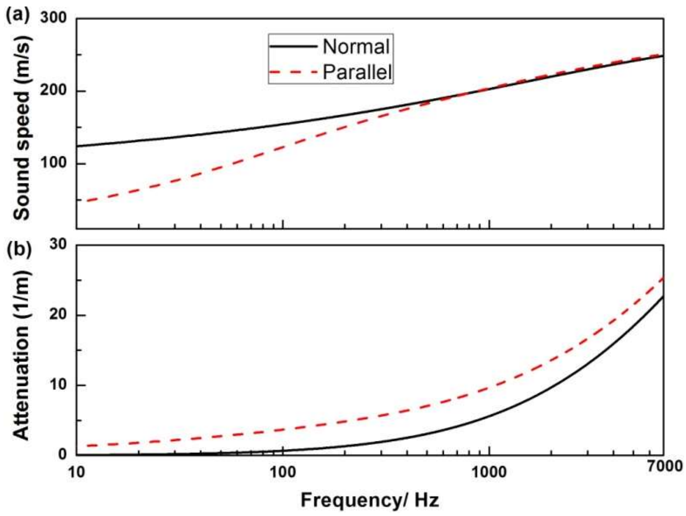

Fig. 2-7 Sound speed and attenuation coefficient of sintered fibrous metal for sound incidence parallel and normal to the fiber plane

2.4 Anisotropic acoustic properties of sintered fiber metal

In this section, the proposed theoretical model, validated against experimental measurements, is employed to investigate the effects of morphological parameters (fiber diameter and porosity in particular) of the sintered fibrous metal on its anisotropic acoustical properties. A more fundamental understanding on sound propagation in this kind of materials is provided.

2.4.1 Influence of fiber diameter

Figure 2-8 plots the predicted SAC of rigid-backed sintered fibrous stainless steel sheet as a function of frequency for three different fiber diameters, 40 μm, 50 μm and 60 μm, both for sound propagating normal and parallel to the fiber plane. For the plotting, the porosity and sheet thickness are fixed at 90% and 20 mm, respectively. It can be seen from Fig. 2-8 that the SAC increases as the fiber diameter is decreased. For the cell shown in Fig. 2-2(b), the specific contact area between the saturated fluid and fibers in the fibrous metal is:

$$S_c = \frac{2(1-\Omega)}{a} \tag{2-36}$$

The specific contact area is the contact area between the fluid and fibers in unit volume of the material. It can be deduced from Eq. (2-36) that the specific contact area between the fluid and fibers grows as the fiber diameter decreases for a given porosity. The viscous effect is intensified as the specific contact area is increased, beneficial for enhanced sound absorption.

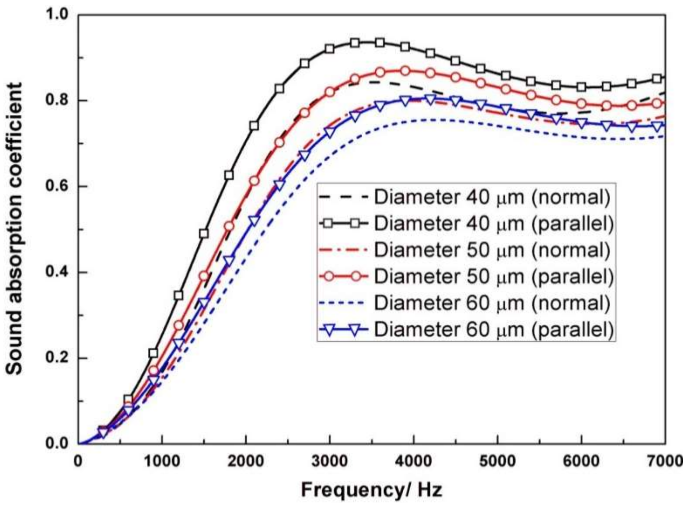

Fig. 2-8 SAC of sintered fibrous metal sheet for selected fiber diameters with fixed porosity of 90% and sheet thickness of 20 mm

Figure 2-9 plots the sound speed and attenuation coefficient as functions of frequency for selected fiber diameters (porosity 90% and sheet thickness 20 mm). The results of Fig. 2-9 show that the sound speed decreases while the attenuation coefficient increases with decreasing fiber diameter. These trends can also be attributed to the increased viscous effect as the fiber diameter is decreased. Figures 2-8 and 2-9 also reveal the difference in acoustical properties between normal and parallel incidence when the fiber diameter is varied. Here we define three parameters to represent the difference in acoustical properties:

Sound absorption difference:

$$\chi_{\alpha}(\omega) = \frac{|\alpha_P(\omega) - \alpha_N(\omega)|}{\alpha_P(\omega)} \tag{2-37}$$

Sound speed difference:

$$\chi_{sp}(\omega) = \frac{|c_P(\omega) - c_N(\omega)|}{c_P(\omega)} \tag{2-38}$$

Attenuation difference:

$$\chi_{at}(\omega) = \frac{|\delta_P(\omega) - \delta_N(\omega)|}{\delta_P(\omega)} \tag{2-39}$$

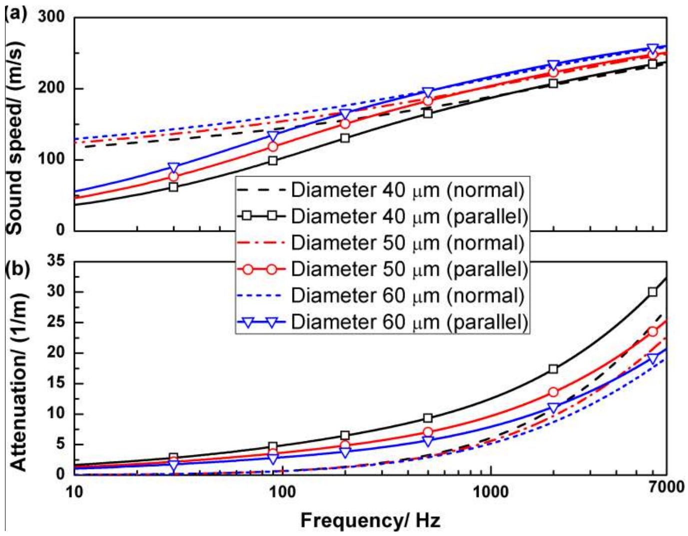

Fig. 2-9 Sound speed and attenuation coefficient of sintered fibrous metal sheet for selected fiber diameters with fixed porosity of 90% and sheet thickness of 20 mm

The sound absorption difference, sound speed difference and attenuation difference is able to characterize the relative differences of the acoustic properties in the two principle directions of sintered fibrous metals. It can be seen from Fig. 2-10 that the acoustical property differences all decrease as the fiber diameter is increased, implying that the acoustic anisotropy of the sintered fibrous metal is weakened by increasing the fiber diameter. As the fiber diameter is increased while the porosity is fixed, the space between the fibers is enlarged, which weakens the interaction among the fibers. Therefore, fiber distribution plays a less important role in the acoustical properties of the sintered fibrous metal.

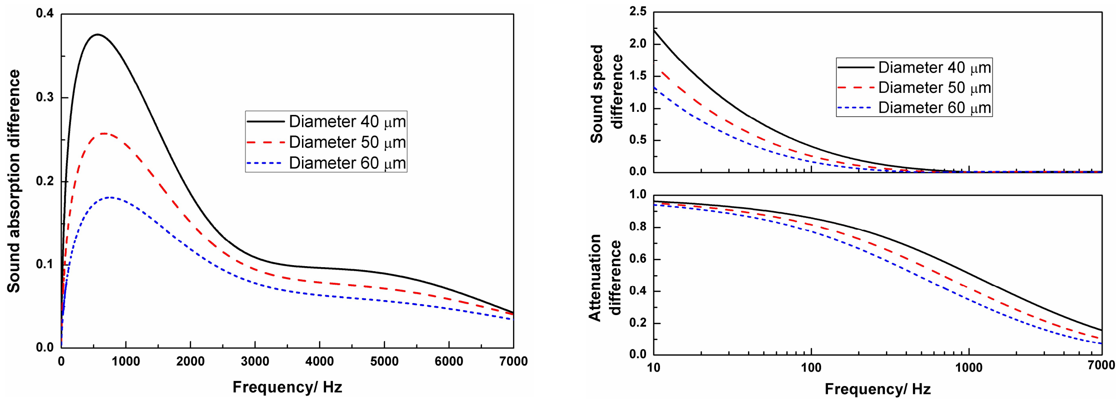

(a) (b)

Fig. 2-10 Anisotropic acoustic properties of sintered fibrous metal sheet for selected fiber diameters (porosity 90% and sheet thickness 20 mm): (a) sound absorption difference; (b) sound speed and attenuation differences

2.4.2 Influence of porosity

Figure 2-11 plots the predicted SAC of rigid-backed sintered fibrous stainless steel sheet as a function of frequency for three different porosities, 0.8, 0.85 and 0.9, both for sound propagating normal and parallel to the fiber plane. The fiber diameter and sheet thickness are fixed at $50\ \mu\text{m}$ and 20 mm, respectively. As the porosity is decreased, the SAC curve shifts to lower frequency as a whole. This can be explained by comparing the sound speeds calculated with different porosities shown in Fig. 2-12 (a). As is known, the sound absorption peak appears when the distance between the incidence and reflected sound is equal to 1/4 wavelength, namely:

$$d = \frac{1}{4}\lambda_p = \frac{1}{4}\frac{c}{f_p} \tag{2-40}$$

where λ_p is the wavelength of sound at the peak frequency f_p, and c is sound speed in the fibrous metal. From Fig. 2-11(a) it is seen that the sound speed decreases with decreasing porosity, causing reduced peak frequency. In addition, Fig. 2-11(b) presents the variation trend of the attenuation coefficient with porosity. The attenuation coefficient decreases as the porosity is increased. As shown in Eq. (2-36), the specific contact area decreases with increasing porosity and fixed fiber diameter, weakening therefore the viscous effect. Correspondingly, the sound speed increases while the attenuation coefficient decreases.

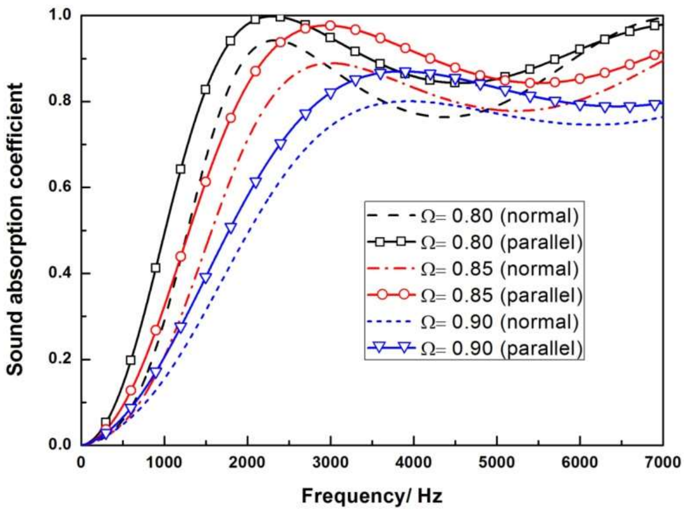

Fig. 2-11 SAC of sintered fibrous metal sheet for selected porosities with fixed fiber diameter of $50\ \mu m$ and sheet thickness of 20 mm

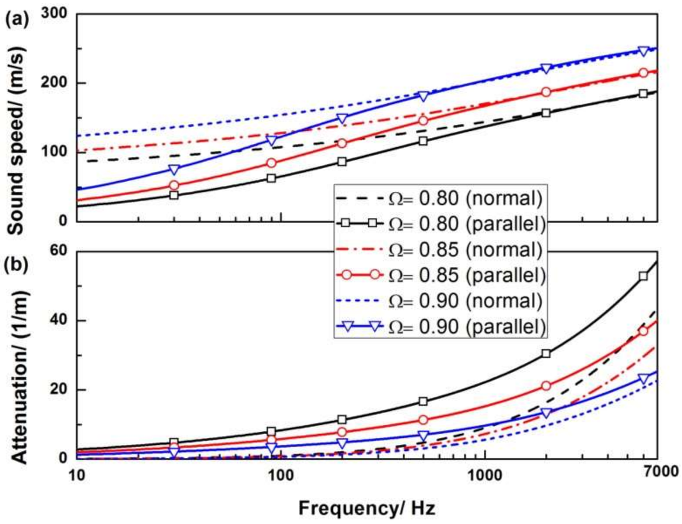

Fig. 2-12 Sound speed and attenuation coefficient of sintered fibrous metal sheet for selected porosities with fixed fiber diameter of $50\ \mu m$ and sheet thickness of 20 mm

It can be seen from Fig. 2-13 that the difference in acoustical properties shown in Figs. 2-11 and 2-12 decreases in general with increasing porosity except that the difference in sound speed fluctuates in the high frequency range (> 1500 Hz). As the porosity is increased, the space between adjacent fibers is enlarged. As aforementioned, the acoustic anisotropy of the sintered fibrous metal is weakened as the space between fibers is increased. Given that the sound absorption peaks at quarter-wavelength resonance, it is thus understandable for the fluctuation appearing in Fig. 2-13 (a).

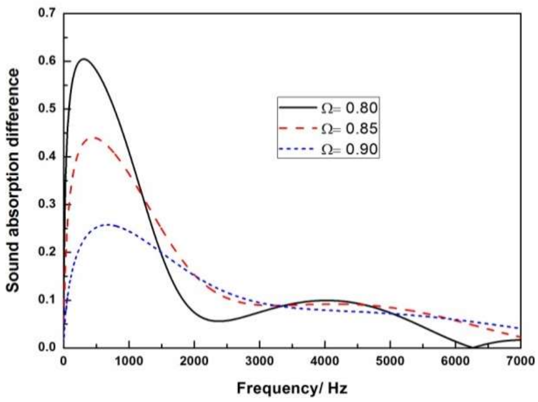

(a)

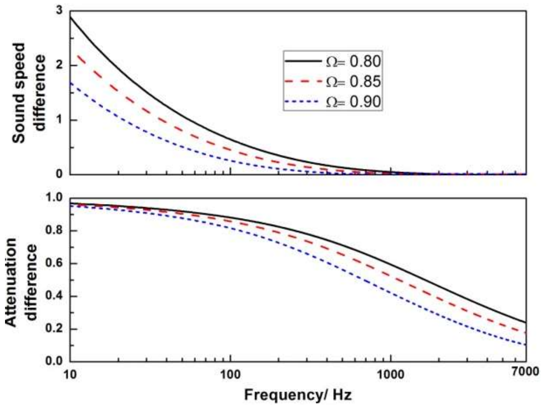

(b)

Fig. 2-13 Anisotropic acoustic properties of sintered fibrous metal with different porosities (fiber diameter 50 μm and sheet thickness 20 mm): (a) sound absorption difference; (b) sound speed and attenuation difference

2.5 Conclusions

The anisotropic acoustical properties of sintered fibrous metal (stainless steel) are investigated both theoretically and experimentally. Built upon the idealized model of randomly placed parallel fiber array, the dynamic mass density and effective bulk modulus of sound propagation both normal and parallel to the fiber plane are calculated by solving the velocity and temperature fields in the array. Acoustical properties including sound absorption, sound speed and attenuation coefficient of sintered fibrous metal sheets are obtained as functions of morphological parameters such as porosity, fiber diameter and sheet thickness. Experimental measurements are carried out to validate the theoretical model predictions, with good agreement achieved. The model is subsequently employed to quantify the influence of fiber diameter and porosity on the acoustic anisotropy of the sintered fibrous metal. The main findings are summarized as follows:

1) As the fiber diameter (other relevant parameters fixed) is decreased, the SAC of sintered fibrous metal increases due mainly to enhanced viscous effect,
2) The SAC decreases with increasing porosity (other relevant parameters fixed) due to shift of sound absorption peak towards low frequency.
3) The sintered fibrous metal exhibits anisotropic acoustical properties, having higher sound absorption/attenuation coefficient and lower sound speed in the direction parallel to the fiber plane than those in the direction normal to it. The difference in acoustic properties between parallel and normal directions decreases with increasing fiber diameter or increasing porosity due to reduced fiber distribution effect (i.e., fiber interaction effect).

3 Sound Absorption Coefficient Optimization of Gradient Sintered Fibrous Metal

3.1 Sound absorption of gradient multilayer sintered fibrous metal

The gradient sintered fibrous metal is produced to provide better acoustic properties based on the uniform (homogeneous) sintered fibrous metal. A gradient sintered fibrous metal can be fabricated by sintering several fibrous felt layers having different morphological parameters that are stacked on top of each other.

For a gradient sintered fibrous metal composed of n layers of different uniform fibrous metal felts backed by a rigid wall shown in Fig. 3-1, the recursion formula for surface impedance under normal incident sound wave is

$$Z_s\left(x_n\right)=Z_{n-1}\frac{Z_s\left(x_{n-1}\right)\coth\left(\mathrm{i}k_{n-1}d_{n-1}\right)+Z_{n-1}}{Z_s\left(x_{n-1}\right)+Z_{n-1}\coth\left(\mathrm{i}k_{n-1}d_{n-1}\right)} \tag{3-1}$$

where Z_{n-1}, d_{n-1} and k_{n-1} are the characteristic impedance, thickness and the wave number of the $(n-1)$th layer, respectively. The characteristic impedance and propagation constant are calculated by Eqs. (2-31) and (2-32). The normal incident SAC of the gradient sintered fibrous metal can be obtained as

$$\alpha_N=1-\left|\frac{Z_s\left(x_n\right)-\rho_0c_0}{Z_s\left(x_n\right)+\rho_0c_0}\right|^2 \tag{3-2}$$

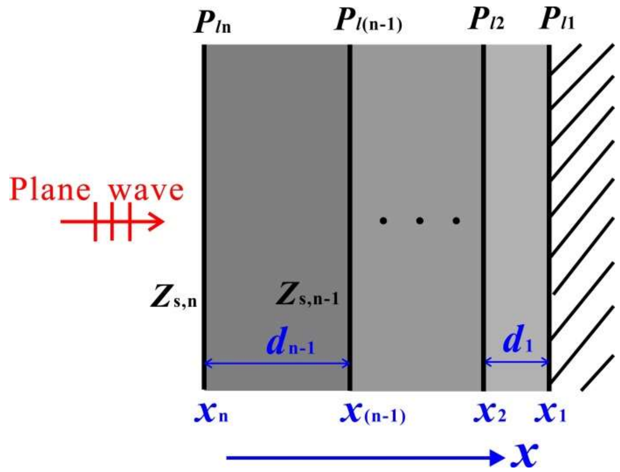

Fig. 3-1 Schematic of sound incident on gradient (multilayer) sintered fibrous metal felt

The theoretical model for the gradient sintered fibrous metal is further validated by the experimental results. The measured SAC of 2 gradient sintered fibrous metal samples using the impedance tube method are compared with the theoretical predictions in Fig. 3-2. The physical parameters of the tested samples are listed in Table 3-1. Overall, the SAC predicted by the theoretical model fit well with the test data. The model is then applied in the next section to perform systematic optimization studies on gradient sintered fibrous metal felts.

Table 3-1 Physical parameters of sintered fibrous metal samples

Sample number	Layer	Fiber diameter (μm)	Porosity (%)	Thickness of layer (mm)
	1st	100	73	10
a#	2nd	50	73	10
	3rd	25	77	10
	1st	6.5	90	5
b#	2nd	12	90	5
	3rd	20	90	5

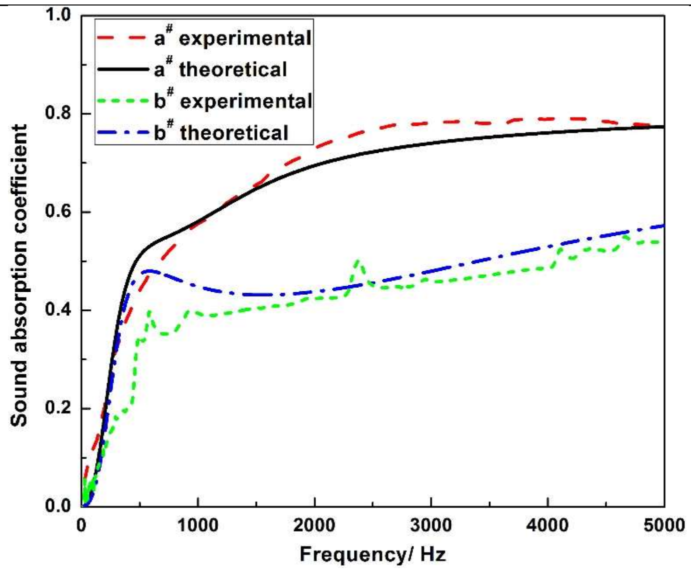

Fig. 3-2 SAC of gradient sintered fibrous metal samples: comparison between model predictions and experimental measurements.

3.2 Sound absorption optimization of gradient sintered fibrous metal

A SAC optimization procedure is presented for gradient sintered fibrous metal felts in this section. It can be seen from the theoretical model that the SAC of a sintered fibrous metal sample is determined by its fiber diameter and porosity. The most obvious and effective way for the improvement of SAC is to optimize the key topological parameters influencing sound propagating in the fibrous metal.

In certain practical applications where weight and/or volume are of critical concern, a limit is usually placed upon the amount (e.g., thickness of layer) of fibrous sound absorbing material that is allowed to use. A good example is the vibration damping and acoustic shielding of key electronic devices in aerospace technologies. Therefore, an optimization method of SAC is proposed in the following section for gradient sintered fibrous metal felt (Fig. 3-1) under the restriction that its total thickness is fixed. Relevant objective functions and constraints are proposed for porosity optimization, fiber diameter optimization.

3.2.1 Optimization of porosity distribution

1) Optimization at a sole frequency

To optimize the distribution of porosity in a multi-layered sintered fibrous metal felt (Fig. 3-1) at a sole frequency, the objective function for SAC α may be written as:

$$\max\ f\left(\Omega_1,h_1,\ldots\Omega_n,h_n\right)=\alpha\left(\Omega_1,h_1,\ldots\Omega_n,h_n\right) \tag{3-3}$$

where $\alpha\left(\Omega_1,h_1,\ldots\Omega_n,h_n\right)$ is the SAC of the multilayer fibrous metal, Ω_i and h_i ($i=1,2,\ldots,n$) represent the porosity and thickness of the ith layer, and n is the total number of layers. The diameter of all fibers in the metal fiber is fixed.

The porosity should be bigger than zero but smaller than unity, while the thickness of each layer should be bigger than the diameter of fibers in the layer. For the case that the volume of the material is fixed, the total thickness of the sample is pre-specified. Therefore, the constraints of the objective function are:

$$\begin{aligned} s.t.\quad & 0<\Omega_i<1 \\ & d<h_i<h_p \\ & \sum_{i=1}^{n} h_i = h_p \\ & i=1,2,\ldots,n \end{aligned} \tag{3-4}$$

where h_p is the expected sample thickness.

2) Optimization within a frequency range

For porosity optimization within a pre-specified frequency range, the objective function should be the sum of SAC in the pre-specified frequency range, as:

$$\max\ f\left(\Omega_1,h_1,\ldots\Omega_n,h_n\right)=\int_{f_l}^{f_u}\alpha\left(\Omega_1,h_1,\ldots\Omega_n,h_n\right)df \tag{3-5}$$

where f_l and f_u are the lower and upper bound of the pre-specified frequency range. The constraints are the same as those detailed in Eq. (3-4) for the case of sole-frequency optimization.

3.2.2 Optimization of fiber diameter distribution

1) Optimization at a sole frequency

To optimize the distribution of fiber diameter at a single frequency, the objective function may be written as:

$$\max\ f\left(d_1,h_1,\ldots d_n,h_n\right)=\alpha\left(d_1,h_1,\ldots d_n,h_n\right) \tag{3-6}$$

where $\alpha\left(d_1,h_1,\ldots d_n,h_n\right)$ is the SAC and d_i is the diameter of fibers in the ith layer. In this case, the porosity of the multilayer fibrous metal is fixed.

Although in theory the fiber diameter may vary from infinitely small to infinitely large, in practice there is a lower bound of fiber diameter as set by the particular type of manufacturing technology employed to fabricate the fibrous metal. In the present study, the smallest fiber diameter is set to be $6.5\ \mu\text{m}$. The constraints of the objective function are thence:

$$\begin{aligned} s.t.\quad & d_i \geq 6.5\times10^{-6} \\ & d_i < h_i < h_p \\ & \sum_{i=1}^{n} h_i = h_p \\ & i = 1,2,\ldots,n \end{aligned} \tag{3-7}$$

2) Optimization within a frequency range

For fiber diameter optimization within a pre-specified frequency range, the objective function is:

$$\max\ f\left(d_1,h_1,\ldots d_n,h_n\right)=\int_{f_l}^{f_u}\alpha\left(d_1,h_1,\ldots d_n,h_n\right)df \tag{3-8}$$

subjected to the same constraints of (3-7) for the case of sole-frequency optimization.

Since the objective functions presented above are all complex multimodal non-differentiable functions, a genetic algorithm (GA) optimization strategy (see appendix) is applied to solve the optimization problem.

3.3 Numerical Results and Discussion

On the basis of the theoretical model presented in Section 3.1 and the optimization method detailed in Section 3.2, selected numerical results are presented in this section to demonstrate the feasibility of the proposed optimization approach.

3.3.1 Optimized porosity distribution

To optimize the porosity distribution, the multilayer fibrous metal sample as shown in Fig. 3-1 has a fixed total thickness of 10 mm, which is relatively small, and a fixed fiber diameter of 20 μm, which is typical for sintered fibrous metal felts. For illustration, the expected frequency is selected as 500 Hz for the case of sole-frequency optimization, while the expected frequency range is set to be 500~1000 Hz for the case of frequency-range optimization.

Figure 3-3(a) compares the SAC of non-optimized (uniform and linearly gradient) fibrous metal samples with that of sole frequency optimized sample. In particular, results for the case of linear porosity distribution are included to highlight the effect of porosity distribution optimization on SAC. Relevant physical parameters employed for the comparison are listed in Table 3-2. Corresponding results for frequency-range optimization are presented in Fig. 3-3(b). It is seen from Figs. 3-3 (a) and (b) that, for both sole frequency and frequency-range optimization, the SAC of sintered fibrous metal felt is greatly enhanced by optimizing the distribution of its porosity.

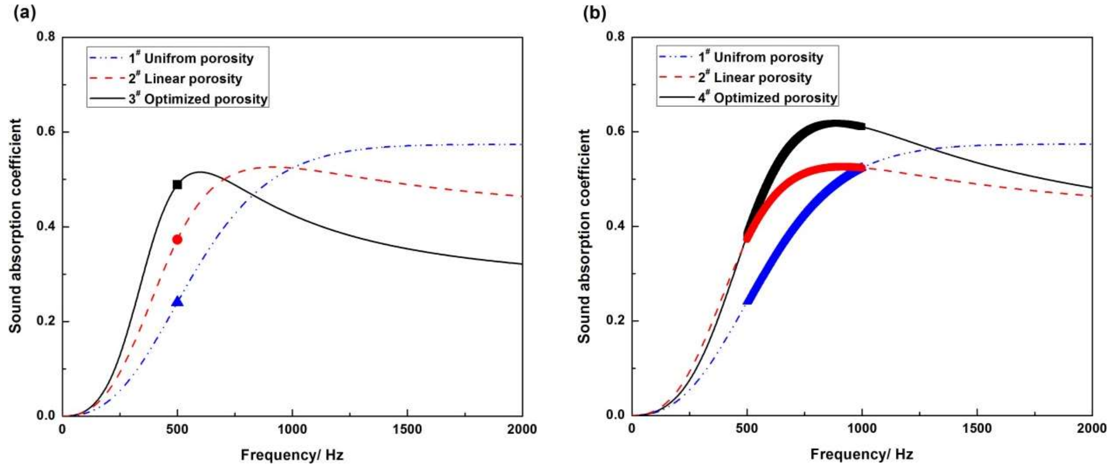

Fig. 3-3 Comparison of SAC among sintered fibrous metal samples with optimized, uniform and linearly gradient porosity distributions: (a) sole frequency (500 Hz) optimization and (b) frequency-range (500~1000 Hz) optimization

To reveal the details of porosity distribution, the porosity of each layer is displayed in Figs. 3-4(a) and (b), for sole frequency and frequency-range optimized samples, respectively. Here, Layer 1 in the multilayer sample (Table 3-2) is the layer placed immediately next to the rigid wall (Fig. 3-1). It is seen from Fig. 3-4 that, even though the optimized samples for sole frequency and frequency range are composed of different numbers of layers, the porosities of both samples first increase then decrease with increasing distance from the incident plane. For instance, in the frequency-range optimized sample (Fig. 3-4b), the first layer (Layer 6) has a porosity lower than that of the last layer (Layer 1) while the third layer (Layer 4) has the highest porosity.

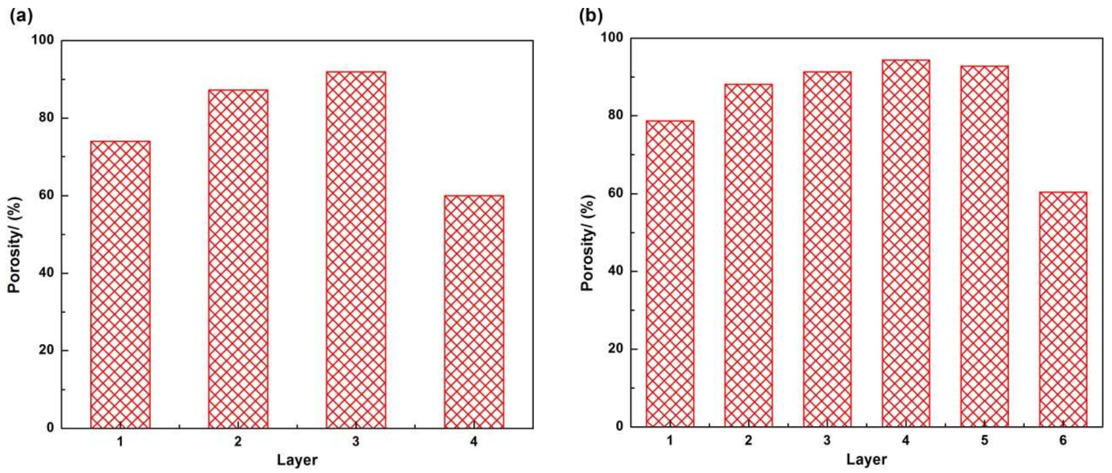

Fig. 3-4 Porosity distribution in porosity optimized fibrous metal sample: (a) sole frequency optimization (Sample $3^{\#}$ in Fig. 3-7a) and (b) frequency-range optimization (Sample $4^{\#}$ in Fig. 3-3b)

Table 3-2 Physical parameters of porosity optimized and non-optimized sintered fibrous metal samples

Sample	Layer	Porosity	Fiber	Thickness of

number	**arrangement**	**(%)**	**diameter (μm)**	**layer (mm)**
1#	Single layer	78.3	20	10.0
	1st	95	20	2.57
	2nd	85	20	5.0
2#	3rd	75	20	1.82
	4th	65	20	0.61
	1st	74	20	2.57
	2nd	87.2	20	5.0
3#	3rd	91.9	20	1.82
	4th	60	20	0.61
	1st	78.7	20	2.39
	2nd	88.1	20	2.83
	3rd	91.3	20	2.83
4#	4th	94.3	20	1.02
	5th	92.8	20	0.5
	6th	60.4	20	0.43

3.3.2 Optimized fiber diameter distribution

To optimize the distribution of fiber diameter, the target multilayer sample has a fixed thickness of 10 mm and a fixed porosity of 90%. Similar to the case of porosity optimization, 500 Hz and 500~1000 Hz are selected for sole frequency and frequency-range optimization, respectively.

As shown in Fig. 2-8 (Chapter 2), the SAC of sintered fibrous metal felt decreases with increasing fiber diameter at low frequencies. Therefore, for sole frequency (500 Hz) optimization, the optimized fiber diameter should be the lower bound 6.5 μm. For frequency-range optimization, the SAC of optimized, uniform and linearly gradient sintered fibrous metal samples are compared in Fig. 3-5. Corresponding physical parameters of these samples are listed in Table 3-3. For the optimized multilayer sample, Fig. 3-6 presents the distribution of fiber diameter across its thickness (10 mm).

The results of Fig. 3-5 indicate that, within the frequency range considered, the optimized fibrous sample absorbs sound better than other samples. Further, as shown in Fig. 3-6, the fiber diameter first increases then decreases as the distance from the incident plane is increased.

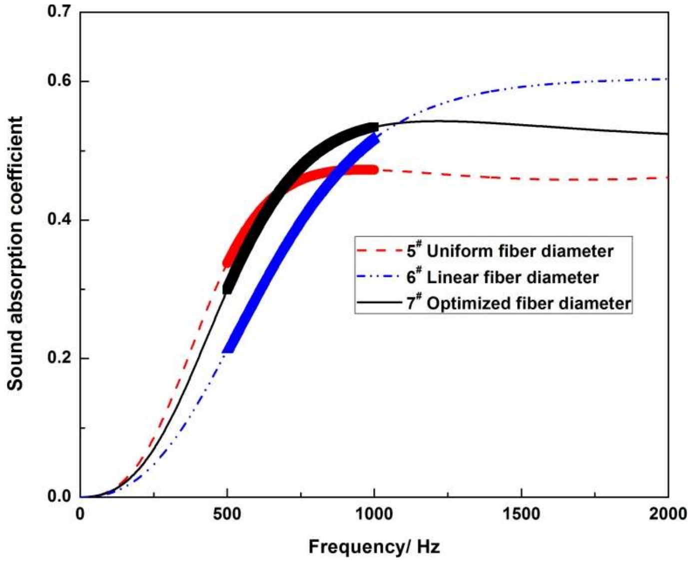

Fig. 3-5 Comparison of SAC among sintered fibrous metal samples with uniform, linearly gradient and frequency range (500~1000 Hz) optimized fiber diameter distributions

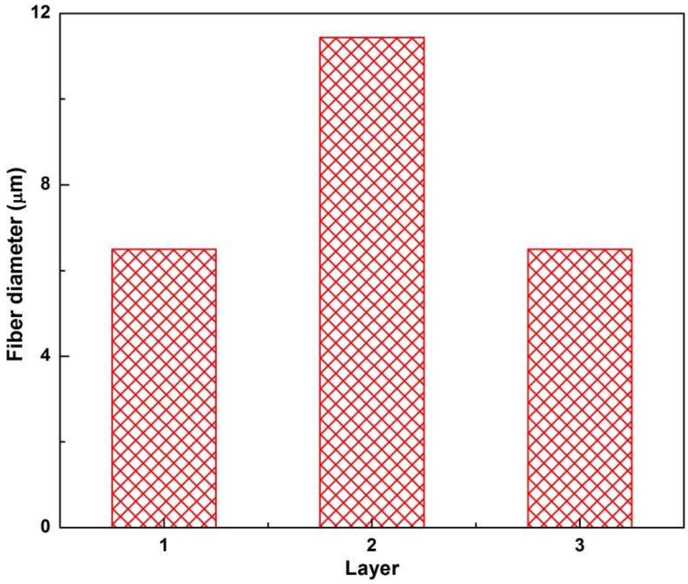

Fig. 3-6 Distribution of fiber diameter in fibrous metal sample with frequency-range optimized fiber diameters (Sample $7^{\#}$ in Fig. 3-5)

Table 3-3 Physical parameters of metal fiber samples with optimized (frequency range) and non-optimized fiber diameter distributions

Sample number	**Layer**	**Porosity (%)**	**Fiber diameter (μm)**	**Thickness of the layer (mm)**
$5^{\#}$	Single layer	90	6.5	10.0
	1st	90	7	1.84
$6^{\#}$	2nd	90	8	4.33
	3rd	90	9	3.83

	1st	90	6.5	1.84
7#	2nd	90	11.44	4.33
	3rd	90	6.5	3.83

3.4 Conclusions

A theoretical method of SAC optimization is presented for sintered fibrous metal felts based upon the proposed sound absorption model in Chapter 2. The SAC of graded (multi-layer) sintered fibrous metal samples are measured. Comparison between theoretical predictions and experimental results confirms the accuracy of the theoretical model in evaluating the SAC of sintered fibrous metal felts. Objective functions and constraint conditions are subsequently set up for porosity and fiber diameter at a sole frequency or within a predefined frequency range. It is demonstrated that sintered fibrous metal felts with optimized gradient morphologies exhibit superior sound absorption behavior over non-optimized samples at relatively low frequencies.

4 Sound Absorption Optimization of Graded Semi-open Cellular metals

4.1 Introduction of semi-open cellular metal

Semi-open cellular metals refer to a special kind of porous materials manufactured by the infultration processing method[138,139]. The molten metals are first infiltrated into the apertures of stacking water-soluble particales (millimeter scale) with a controlled high pressure, the particales are subsequently removed by water and the semi-open cellular metal remains. The sperical pores inside the semi-open cellular metal are connected by submillimeter sized pore openings. A typical cellular morphology of the material is presented in Fig. 4-1.

Due to the simple construction, pore morphology designability and convenient manufacturing procedures, semi-open cellular metals have attracted increasing attention as a sound absorbent material. As a key geometric parameter of the material, the degree of pore opening (DPO) is closely related to the infiltration process[139]. By applying the principle of electroacoustic analogy, Lu *et al.*[138] proposed a theoretical model based on idealized pore morphologies to evaluate the SAC of this material, and compared model predictions with experimental measurements. Further sound absorption measurements have been conducted to examine the effects of pore size, pore opening and pore opening density[140]. The underwater sound absorption behavior of the material was also experimentally investigated by Cheng *et al.*[141] using the pulse tube method. The theoretical and experimental results demonstrated that the sound absorption properties of semi-open cellular metals are strongly affected by geometrical parameters such as porosity, pore size and degree of pore opening. This suggests the feasibility of further improving the sound absorption performance of the material by tuning the distributions of key geometrical parameters.

Despite these efforts, hitherto there is yet a systematic study focusing on the effects of graded distributions of key geometrical parameters (*e.g.*, porosity, pore size and degree of pore opening) upon the sound absorbing capability of semi-open cellular metals. Also, an efficient optimization strategy is needed to provide optimal acoustic design in terms of actual engineering requirements. These deficiencies are squarely addressed in the present study. Based upon idealized cellular morphology consisting of circular apertures and cylindrical cavities as well as the principle of electroacoustic analogy, an impedance acoustic model is firstly proposed for graded (multi-layered) semi-open cellular metal. The model is subsequently employed together with an optimization strategy by virtue of the genetic algorithm method to provide optimal solutions for graded semi-open cellular metals as a sound absorbing material.

4.2 Theoretical model and validation for graded semi-open cellular metals

Based on the acoustic impedance recursion formula, a theoretical model is established in this section to characterize the SAC of semi-open cellular metal. To this end, following Lu *et al.*[138], the pores in semi-open cellular metal may be idealized as regularly spaced uniform spherical pores, with uniform circular pore openings at the joints between the pores. For sound vertically incident into the cellular metal, the spherical pores may be further approximated as a regular hexagonal lattice with circular pore opening on each of its eight surfaces as shown in Fig. 4-1. The modeled porous material is characterized by pore size *D*, pore opening *d*, and porosity Ω. Note that the cell has a coordination number of 8, which is close to the experimentally measured value of 7.0–7.5. Also, although hexagonal arrangement of the pore openings is assumed, the effect of other arrangements such as regular square array or random distribution upon the sound absorption performance of the model material is expected to be small[138].

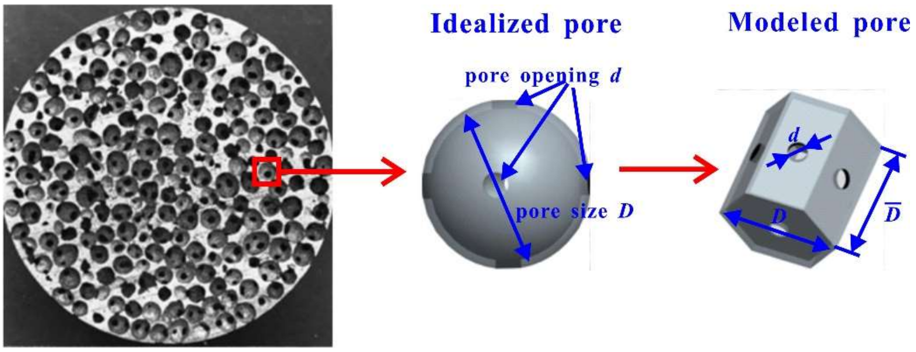

Fig. 4-1 Idealized unit cell and arrangement for cellular metals having semi-open cells

The diameter of the circumcircle of the hexagonal lattice is equal to the diameter of the spherical pore D, whilst the height of the hexagonal lattice $\overline{D}$ is set to ensure that the volume of the hexagonal lattice is equal to that of the spherical pore, so that:

$$\overline{D} = 0.806D \tag{4-1}$$

With reference to Fig. 4-1, $\overline{D}$ is the distance between the middle planes of end walls of the unit cell in the longitudinal direction. For simplicity, the diameter of the circular openings on the surfaces of the unit cell is assumed equal to that of the pore opening of a real porous metal, and that the porosity of the model material is identical to that of the real material. Besides, uniform cell-wall thickness is assumed and each cell wall is assumed to have identical thickness *t*. Further, the cell walls are assumed to be sufficiently thin so that $t << D$. In terms of pore diameter D and porosity Ω, the cell-wall thickness may be expressed as[138]: $t \approx (1\text{-}\Omega)D\Big/\left(3.55\text{-}6\left(d/D\right)^2\right)$. Finally, since the density and stiffness of the metal skeleton are much larger than those of air, the skeleton is regarded as motionless as sound propagates across the cellular metal.

Consider first a model cellular metal with only one cell in the thickness direction (also the direction of sound propagation). With the wavelength of the sound traveling in air assumed much larger than *D* and that the sound wave is normally impinging upon the cellular metal surface, the impedance z_0 of the circular pore opening may be calculated by applying the principle of electroacoustic analogy and the relevant formula for the acoustic impedance of a small, circular orifice in a thin plate, as[84,138]:

$$z_0 = R_0 + iM_0 \tag{4-2}$$

where R_0 and M_0 are functions of parameter $\beta = \sqrt{\omega\rho_0 / \eta}d / 2$, the latter determined by the quotient of pore diameter and viscous layer thickness in the pore. Here, d is the diameter of the pore opening (Fig. 4-1). For $\beta < 1$ (low-frequency range or small circular opening):

$$R_0 = 32\eta t / d^2 \tag{4-3}$$

$$M_0 = (4/3)\omega\rho_0 t \tag{4-4}$$

When $1 < \beta < 10$ (intermediate frequency range):

$$R_0 = \frac{32\eta t}{d^2}\sqrt{1+\beta^2/32} \tag{4-5}$$

$$M_0 = \omega\rho_0 t\left\{1+1/\sqrt{9+\beta^2/2}\right\} \tag{4-6}$$

When $\beta > 10$ (high-frequency range or large circular opening):

$$R_0 = 8\eta t\beta / \sqrt{2}d^2 \tag{4-7}$$

$$M_0 = \left(8\eta t\beta / \sqrt{2}d^2 + \omega\rho_0 t\right) \tag{4-8}$$

Since the end effect of the pore openings should be considered for short tubes [142,143], the cell-wall thickness t needs to be corrected by an end correction $a = 8d/3\pi$ when $\beta < 1$ or $\beta > 10$. Thus t is replaced by the effective thickness t', as[143]:

$$t' = t + a \tag{4-9}$$

Accordingly, Eqs. (4-3) and (4-4) become:

$$R_0 = 32\eta\left(t+\frac{8d}{3\pi}\right)/d^2 \tag{4-10}$$

$$M_0 = (4/3)\omega\rho_0\left(t+\frac{8d}{3\pi}\right) \tag{4-11}$$

whilst Eqs. (4-7) and (4-8) become:

$$R_0 = 8\eta\left(t+\frac{8d}{3\pi}\right)\beta/\sqrt{2}d^2 \tag{4-12}$$

$$M_0 = 8\eta\left(t+\frac{8d}{3\pi}\right)\beta/\sqrt{2}d^2 + \omega\rho_0\left(t+\frac{8d}{3\pi}\right) \tag{4-13}$$

Similarly, with the end effect added to Eqs. (4-5) and (4-6) for $1 < \beta < 10$, the acoustic impedance of the pore opening becomes[84]:

$$R_0 = \frac{32\eta t}{d^2}\left\{\sqrt{1+\beta^2/32} + \sqrt{\beta d/4t}\right\} \tag{4-14}$$

$$M_0 = \omega\rho_0 t\left\{1+1/\sqrt{9+\beta^2/2} + 0.85d/t\right\} \tag{4-15}$$

In addition to the acoustic impedance of pore openings, the impedance of air inside the hexagonal cells Z_D needs to be determined. To this end, the hexagonal prismatic pore of Fig. 4-1 is modeled by a circular cylindrical pore of equal cross-sectional area, so that its diameter $\overline{D_c} = 0.909D$. Under such conditions:

$$Z_D = -i\rho_0 c_0 \cot\left(\omega \overline{D_c} / c_0\right) \tag{4-16}$$

Consider next a semi-open cellular metal sample consisted of k layers of unit cells, as shown in Fig. 4-2, with total thickness L. As graded cellular metal are of concern, the unit cell may vary from one layer to another. With the sample backed by a rigid wall, its acoustic impedance may be calculated by employing the recursion formula, as[138]:

$$Z^{(k)} = \begin{cases} Z_0^{(k)} + \dfrac{1}{\dfrac{1}{Z_D^{(k)}} + \dfrac{1}{Z^{(k\text{-}1)}}}, & k \geq 2 \\ Z_0^{(1)} + Z_D^{(1)}, & k=1 \end{cases} \tag{4-17}$$

where $Z_0^{(k)} = z_0^{(k)} \left(\bar{D}_c^{(k)} / d^{(k)}\right)^2$ is the relative specific acoustic impedance of air in the pore openings of the kth layer with $D_c^{(k)}$ and $d^{(k)}$ representing the equivalent cylindrical pore diameter and the pore opening diameter of the kth layer, respectively, $z_0^{(k)}$ is the impedance of circular pore openings of the kth layer, $Z_D^{(k)}$ is the impedance of air in the cells of the k th layer, and $Z^{(k\text{-}1)}$ is the impedance of the sample made of k-1 layers.

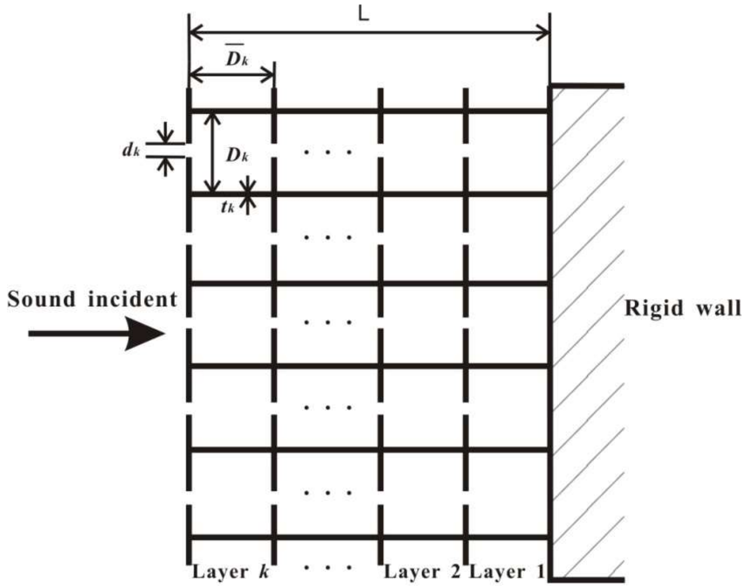

Fig. 4-2 Schematic of a semi-open cellular metal sample with k layers backed by rigid wall

Finally, the SAC α of the semi-open cellular metal sample made of k layers (Fig. 4-2) is obtained as:

$$\alpha = \frac{4R/\rho_0 c_0}{\left(1 + R/\rho_0 c_0\right)^2 + \left(M/\rho_0 c_0\right)^2} \tag{4-18}$$

where $R = \mathrm{Re}\left(Z^{(k)}\right)$ and $M = \mathrm{Im}\left(Z^{(k)}\right)$ are the resistance and reactance of the impedance for the whole k layers, respectively.

To validate the theoretical model as formulated above, Fig. 4-3 compares the predicted SAC for a 6-layer graded semi-open cellular metal sample with the experimental results of Huang *et al*.[3]. The sample was backed by a rigid wall (*i.e.*, no air gap between the sample and the back plate). The geometrical parameters used are identical to those provided in reference[3]: the pore size of the 6-layer graded cellular metal varies as (0.8, 1.0, 1.2, 1.4, 1.8 and 2.2) mm; each layer containing uniform pores has a fixed thickness of 3 mm and a fixed porosity of 66%. The results shown in Fig. 4-3 demonstrate that overall the model predictions agree well with experimental measurements, capturing accurately the peak at 2000 Hz and the dip at 4000 Hz. The small discrepancy between theory and experiment may be attributed to the idealized nature of the theoretical model used to describe the actual graded semi-open cellular metal.

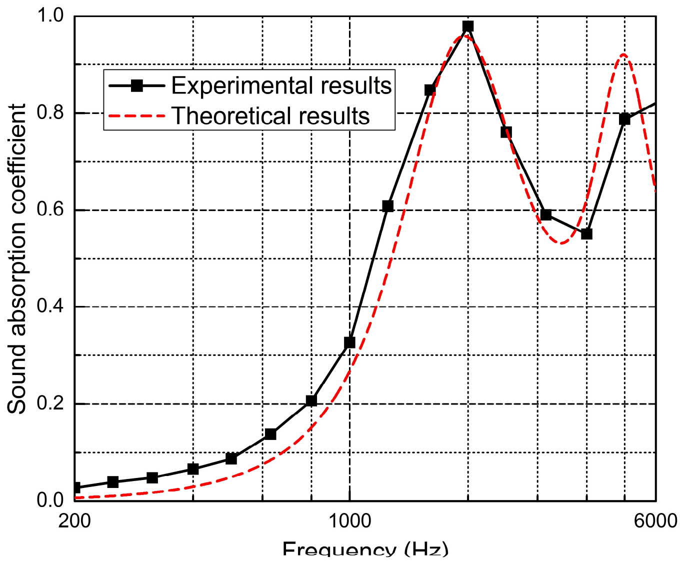

Fig. 4-3 SAC of 6-layer graded semi-open cellular metal: comparison between model predictions and experimental measurements [3]

4.3 Optimization of graded semi-open cellular metals

Built upon the theoretical model detailed in the previous section, we present here a sound absorption optimization procedure for graded cellular metals having semi-open cells. The effects of relevant geometric parameters upon SAC are firstly examined to determine the key optimal design variables. Suitable objective functions and constraints are subsequently developed, whilst the method of genetic algorithm (GA) is adopted to solve the corresponding optimization problems (see appendix).

It can be drawn from the present theoretical model that the sound absorption property of a semi-open cellular metal is mainly determined by three geometric parameters, *i.e.*, circular pore opening diameter d, spherical cell diameter D, and porosity Ω, which provide a broad space for sound absorption optimization of the cellular metal. However, since the degree of pore opening (DPO) $\delta = d/D$ is frequently used during material processing [139], d is replaced here by the dimensionless δ .

Before proceeding further, with the volume (height) and weight of semi-open cellular metal samples fixed, the distribution of one of the three design variables (porosity, pore size, and degree of pore opening) in the sample is varied whilst the two others remain unchanged (Table 4-1) so as to explore towards which direction optimal sound absorption may be achieved. The results are shown in Figs. 4-4 to 4-6 in terms of SAC versus frequency curves. All the samples are backed by a rigid wall, as illustrated schematically in Fig. 4-2.

Table 4-1. Geometrical parameters of semi-open cellular metal samples

Samples	Porosity Ω (%)	Pore size D (mm)	DPO δ	Thickness H (mm)
a	60	1.24	0.3	10
b	50|70	1.24	0.3	10
c	40|60|80	1.24	0.3	10
d	60	1.04|1.44	0.3	10
e	60	0.84|1.24|1.64	0.3	10
f	60	1.24	0.25|0.35	10
g	60	1.24	0.2|0.3|0.4	10

Notes: "|" denotes the boundary between two different layers.

As can be seen from Fig. 4-4, how porosity is distributed in the semi-open cellular metal affects significantly its sound absorption performance. Within the frequency range of interest, the SAC is noticeably increased as the porosity gradation level (*e.g.*, towards continuously graded distribution in the case of infinite number of layers) is increased. Similarly, the results of Figs. 4-5 and 4-6 demonstrate that the distribution of pore size or DPO also plays an important role, with SAC increasing as the gradation level of each parameter is increased, particularly so in the case of DPO. It appears therefore that there exists a large design window to tune the distribution(s) of porosity, pore size and DPO so that the sound absorption performance of a semi-open cellular metal may be optimized, as discussed in detail next. It is worth noting here that whilst sole frequency optimization is preferable for simplicity, it is also meaningful to perform optimization over a certain frequency range. Both possibilities will be explored.

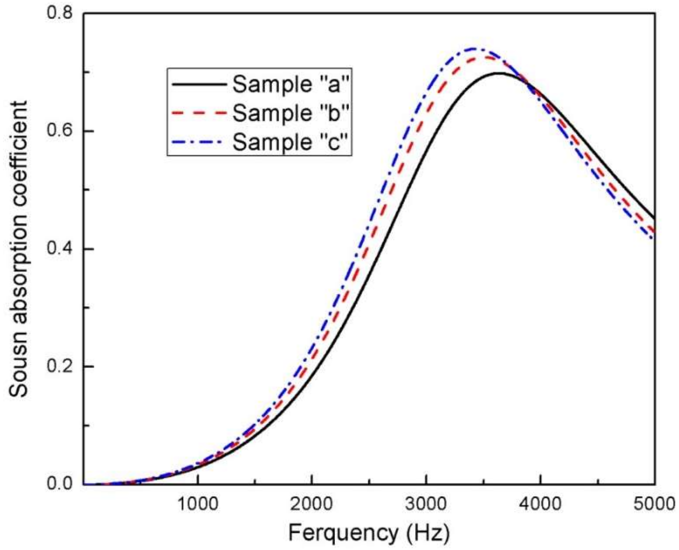

Fig. 4-4 Comparison of SAC between semi-open cellular metal samples having different porosity distributions

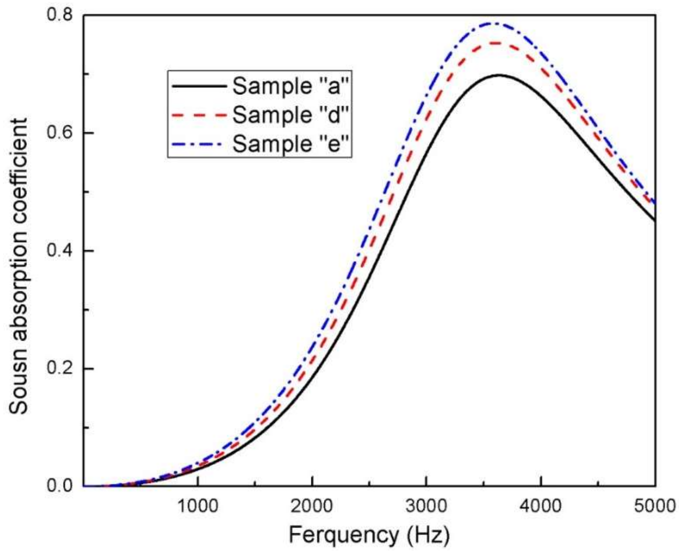

Fig. 4-5 Comparison of SAC between semi-open cellular metal samples having different pore size distributions

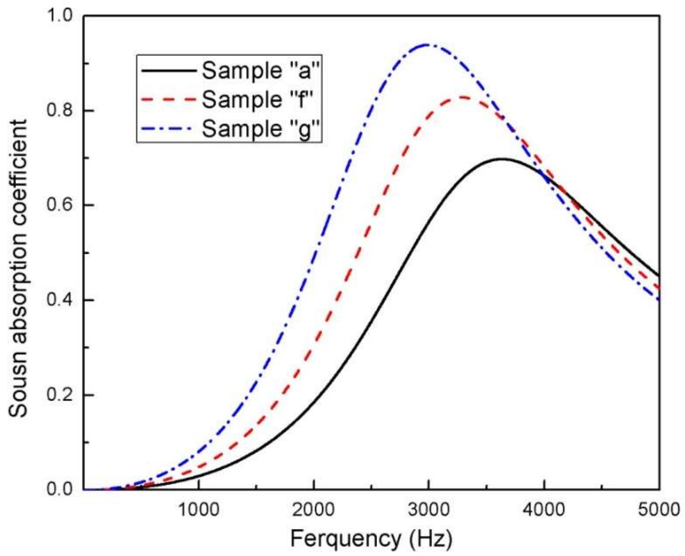

Fig. 4-6 Comparison of SAC between semi-open cellular metal samples having different DPO distributions

4.3.1 Optimization of porosity distribution

To optimize the distribution of porosity in multi-layered semi-open cellular metals at a sole frequency, the objective function for SAC α may be written as:

$$\min\ f(\mathbf{\Omega}) = 1 - \alpha(\mathbf{\Omega}) \tag{4-19}$$

where $\mathbf{\Omega}=[\Omega_1, \Omega_2, \Omega_3, ..., \Omega_n\ ]$ represents the porosity of each layer and n is the total number of layers.

Given an expected porosity of a graded sample, the restriction of same mass and volume as the uniform (ungraded) sample requires that the average of the optimized porosity is equal to the expected porosity. Besides, the porosity should be bigger than zero but smaller than one. Therefore, the constraints of the objective function may be written as:

$$\begin{aligned} s.t.\quad & 0<\Omega_1, \Omega_2, ..., \Omega_n<1 \\ & \sum_{i=1}^{n} \Omega_i \Big/ n \approx \Omega \end{aligned} \tag{4-20}$$

where Ω is the expected averaged porosity since both the mass and volume of the sample are fixed.

As to porosity optimization within a pre-specified frequency range, the objective function may be developed by minimizing the margin of calculated SAC within the frequency range, as:

$$\min\ f\left(\alpha_1(\mathbf{\Omega}), \alpha_2(\mathbf{\Omega}), \alpha_3(\mathbf{\Omega}), ..., \alpha_m(\mathbf{\Omega})\right) = \sqrt{\sum_{i=1}^{m}\left(\alpha_i(\mathbf{\Omega}) - 1\right)^2} \tag{4-21}$$

The constraints are the same as the case of sole frequency optimization, Eq. (4-20).

4.3.2 Optimization of pore size distribution

The optimization of pore size distribution is conducted exactly as the optimization of porosity distribution. The objective function for sole frequency optimization is:

$$\min\ f(\mathbf{D})=1-\alpha(\mathbf{D}) \tag{4-22}$$

where $\mathbf{D}=[D_1, D_2, D_3, \ldots, D_n\ ]$ represents the pore size of each layer.

In order to compare with a uniform sample with identical mass and volume, there should exist a geometric constraint between the sum of the optimized pore size and the expected sample thickness. Moreover, whilst the lower bound of the pore size is 0 mm in theory, the manufacturing process of the material dictates that the pore size cannot be too small because of the surface tension of the molten metal. Practically, for semi-open aluminum foams considered in the present study, the minimum pore size was approximately 0.8 mm[3]. Thus, the constraints of the objective function for pore size optimization are:

$$\begin{aligned} s.t.\quad & 0.806\sum_{i=1}^{n} D_1 \approx H \\ & D_1, D_2, \ldots\ldots, D_n > 0.8 \end{aligned} \tag{4-23}$$

where H is the expected sample thickness.

For optimization within a certain frequency range, the objective function is:

$$\min\ f\left(\alpha_1(\mathbf{D}), \alpha_2(\mathbf{D}), \alpha_3(\mathbf{D}), \ldots, \alpha_m(\mathbf{D})\right)=\sqrt{\sum_{i=1}^{m}\left(\alpha_i(\mathbf{D})-1\right)^2} \tag{4-24}$$

which is subjected to the same constraints of Eq. (4-23).

4.3.3 Optimization of degree of pore opening distribution

The objective function for DPO optimization at a sole frequecy may be written as:

$$\min\ f(\boldsymbol{\delta})=1-\alpha(\boldsymbol{\delta}) \tag{4-25}$$

where $\boldsymbol{\delta}=[\delta_1, \delta_2, \ldots\ldots, \delta_n]$ represents the DPO of each layer.

Since the circular pore opening has a diameter d smaller than that of the spherical pore D, the DPO should be bigger than zero but smaller than one. Further, the wall thickness of the unit cell should be bigger than zero but smaller than the radius of the pore. Therefore, the constraints are:

$$\begin{aligned} s.t.\quad & 0<\delta_1, \delta_2, \ldots\ldots, \delta_n < 1 \\ & 0<t_i \approx \frac{(1-\Omega)D}{3.55-6\delta_i^{\,2}} < \frac{D}{2},\quad i=1,2,\ldots\ldots,n \end{aligned} \tag{4-26}$$

For DPO optimization within a certain frequency range, the objective function is:

$$\min\ f\left(\alpha_1(\boldsymbol{\delta}), \alpha_2(\boldsymbol{\delta}), \alpha_3(\boldsymbol{\delta}), \ldots, \alpha_m(\boldsymbol{\delta})\right)=\sqrt{\sum_{i=1}^{m}\left(\alpha_i(\boldsymbol{\delta})-1\right)^2} \tag{4-27}$$

subjected to the same constraints of (4-26).

4.4 Numerical Results and Discussions

On the basis of the proposed acoustic model for multi-layer semi-open cellular metals and the optimization strategy, numerical calculations are carried out below to evaluate the feasibility of the theoretical model as well as the GA optimization strategy.

4.4.1 Optimized Porosity Distribution

This part aims to identify the porosity distribution in a cellular metal sample that may maximize its SAC subjected to the constraints of identical mass and volume. Here, the semi-open cellular metal sample to be optimized is 10 mm thick, with fixed pore size of 1.24 mm and fixed DPO of 0.2 for each layer, while the expected averaged porosity is 70%. The number of the layers is:

$$n \approx \frac{L}{0.806D} = \frac{10}{0.806 \times 1.24} = 10 \tag{4-28}$$

The optimization of porosity distribution is conducted following the process of the GA strategy outlined in the Appendix. The final optimization results are presented in Table 4-2, both for the sole frequency of 2000 Hz and the frequency range of 2000-2500 Hz. For comparison, results corresponding to uniform as well as linear porosity distributions are also given in Table 4-2. Built upon the porosity distributions listed in Table 4-2, Fig. 4-7 compares the SAC as a function of frequency for samples having uniform porosity distribution, linear porosity distribution and sole-frequency optimized porosity distribution, respectively. The corresponding results for porosity distribution optimized within the frequency range of 2000-2500 Hz are compared with non-optimized results in Fig. 4-8. Here, the simplest graded porosity distribution (*i.e.*, linear porosity distribution) is selected to highlight the superiority of the present optimization strategy based on the GA method.

It can be seen from Fig. 4-7 that, relative to samples having either uniform or linear porosity distribution, the sample having sole-frequency optimized porosity distribution exhibits not only higher SAC at the sole frequency of 2000 Hz but also within a wide frequency range of interest (approximately below 2700 Hz). The same conclusion holds for samples having frequency-range optimized porosity distributions, as shown in Fig. 4-8.

Table 4-2 Typical porosity distributions for semi-open cellular metal samples

Layer	1	2	3	4	5	6	7	8	9	10
Uniform (%)	70	70	70	70	70	70	70	70	70	70
Linear (%)	61	63	65	67	69	71	73	75	77	79
Optimized at 2000 Hz (%)	70	89	89	89	89	89	90	18	61	18
Optimized at 2000-2500 Hz (%)	66	89	98	90	84	71	87	57	29	27

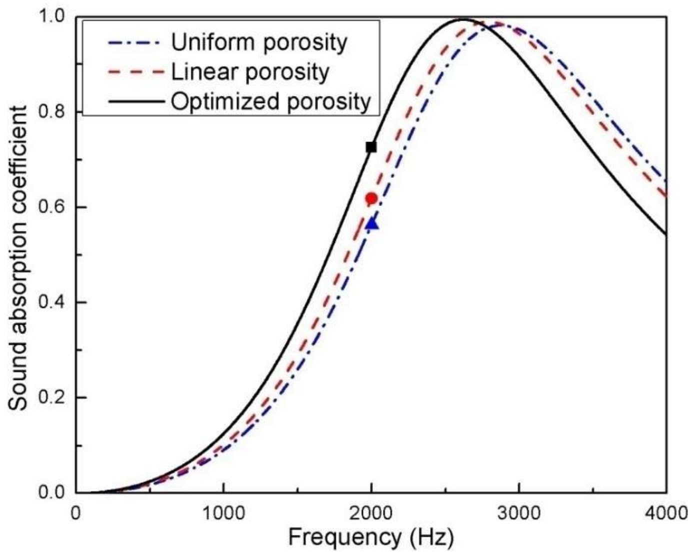

Fig. 4-7 Predicted SAC plotted as a function of frequency for semi-open cellular metal: comparison amongst uniform, linear, and sole-frequency (2000 Hz) optimized porosity distributions

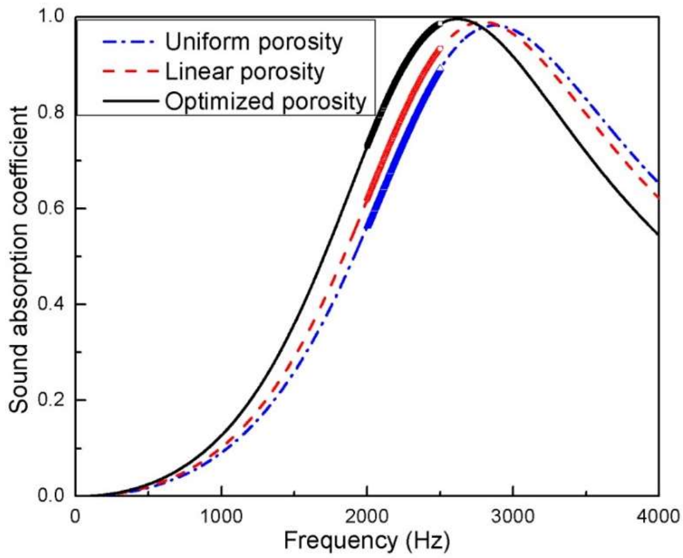

Fig. 4-8 Predicted SAC plotted as a function of frequency for semi-open cellular metal: comparison amongst uniform, linear, and frequency-range (2000-2500 Hz) optimized porosity distributions

To clearly show the optimized porosity distributions, the porosity of each layer is displayed in Figs. 4-9 (a) and (b), for sole frequency and frequency-range optimization respectively. Here, Layer 1 is the rear layer next to the rigid wall, and Layer 10 is the top layer where sound wave impinges on. It can be seen that the porosities of the top layers are the smallest of all the layers. Even though the porosities of the middle layers appear undulate, they are bigger than that of top and rear layers.

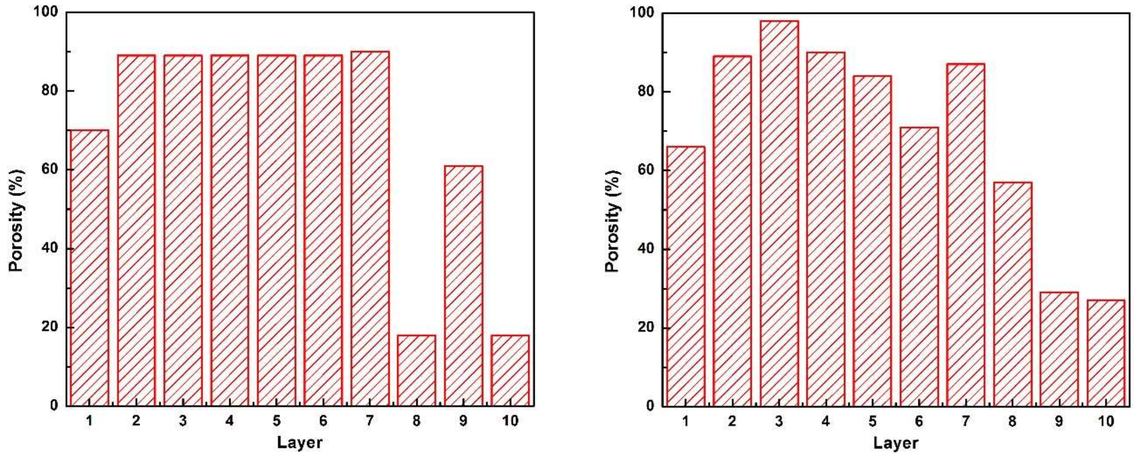

(a) (b)

Fig. 4-9 Porosity distribution in porosity optimized semi-open cellular metals: (a) sole frequency optimization and (b) frequency-range optimization

4.4.2 Optimized Pore Size Distribution

Consider next the optimal design of pore size distribution for 10 mm thick semi-open cellular samples having fixed porosity of 70%, fixed DPO of 0.2 for each layer and a total of 10 layers. Given the objective function and the constraint conditions of Eqs. (4-22) and (4-23), the GA method can effectively search for the optimal pore size distribution. The final results for both sole-frequency (2000 Hz) and frequency-range (2000-2500 Hz) optimization are listed in Table 4-3, together with the results for samples having uniform and linear pore size distributions. Note that for a uniform sample, the thickness of each layer is 1 mm, so that the pore size of each layer can be calculated by Eq. (4-29) as:

$$D_{aver} = \frac{1}{0.806} = 1.24 \text{ mm} \tag{4-29}$$

For a sample with optimized pore size distribution, however, the thickness of each layer becomes unequal since the pore size of each layer is altered to some extent as a result of optimization. Nonetheless, the thickness of each layer may still be estimated using Eq. (4-29).

Table 4-3. Typical pore size distributions for semi-open cellular metal samples

Layer	1	2	3	4	5	6	7	8	9	10
Uniform (mm)	1.24	1.24	1.24	1.24	1.24	1.24	1.24	1.24	1.24	1.24
Linear (mm)	1.69	1.59	1.49	1.39	1.29	1.19	1.09	0.99	0.89	0.79
Optimized at 2000 Hz (mm)	5.2	1.79	0.8	0.8	0.8	0.8	0.8	0.8	0.8	0.8
Optimized at 2000-2500 Hz (mm)	5.2	0.8	0.8	1.78	0.82	0.8	0.8	0.81	0.8	0.8

With the pore size distributions listed in Table 4-3, the predicted SAC of semi-open cellular metals are presented in Figs. 4-10 and 4-11 for sole-frequency optimization and frequency-range optimization, respectively. The optimized pore size distribution enhances significantly the sound absorption capability not only at the selected frequencies (*i.e.*, 2000 Hz in Fig. 4-10 and 2000-2500 Hz in Fig. 4-11) but also over a wide frequency range, especially at low frequencies (below 2500 Hz). Moreover, the noticeable increase of SAC implies that the pore size can be taken a key design parameter for this kind of sound absorbing porous material.

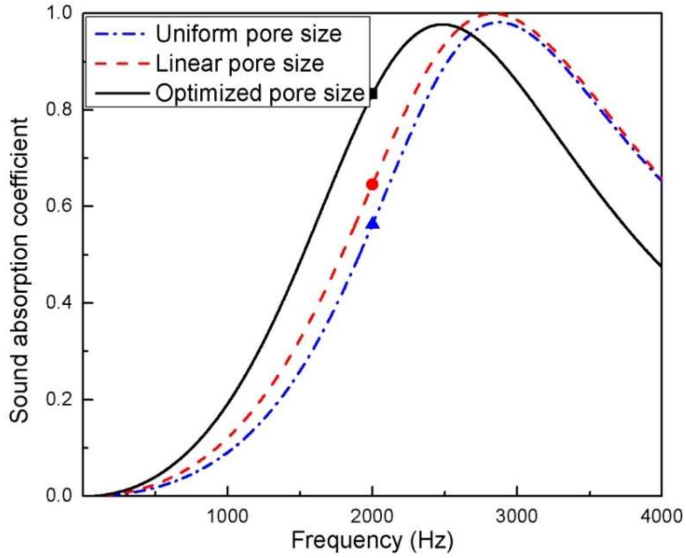

Fig. 4-10 SAC of semi-open cellular metal material: Comparison amongst uniform, linear and sole-frequency (2000 Hz) optimized pore size distributions

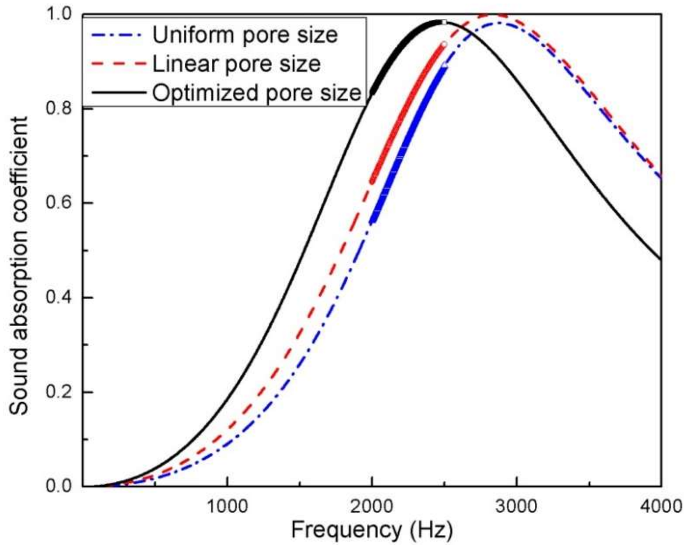

Fig. 4-11 SAC of semi-open cellular metal material: Comparison amongst uniform, linear and frequency-range (2000-2500Hz) optimized pore size distributions

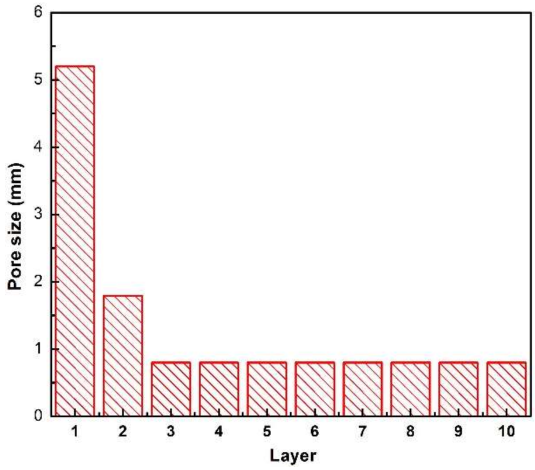

(a)

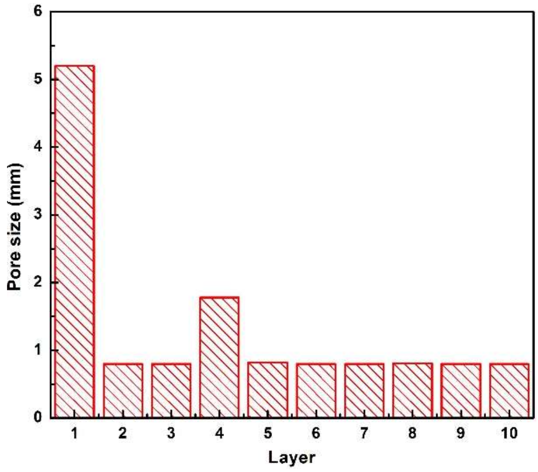

(b)

Fig. 4-12 Pore size distribution in pore sized optimized semi-open cellular metals: (a) sole frequency optimization and (b) frequency-range optimization

The pore sized distributions of the two pore sized optimized semi-open cellular metal samples are plotted in Figs. 4-12(a) and (b). The pore size of the sample with sole frequency optimization shows a trend of increase from the rear layer (Layer 10) to the top layer (Layer 1). Pore sizes of Layers 3-10 are equal to the lower bound 0.8 mm, and pore size of the rear layer are much bigger than that of other layers. Similar trends happen to the sample with frequency-range optimization, except from that a small bulge arises in the middle layer (Layer 4).

4.4.3 Optimized DPO Distribution

Consider next the degree of pore opening (DPO) as a design parameter for semi-open cellular metal samples having 10mm in thickness, with fixed porosity of 70% and fixed pore size of 1.24 mm. Under such circumstances, the number of layers in each sample is estimated as 10. Table 4-4 lists the sole-frequency (2000 Hz) and frequency-range (2000-2500 Hz) optimization results for DPO distribution. For comparison, the corresponding results for uniform and linear DPO distributions are also presented in Table 4-4.

Table 4-4. Typical DPO distributions for semi-open cellular metal samples

Layer	1	2	3	4	5	6	7	8	9	10
Uniform	0.24	0.24	0.24	0.24	0.24	0.24	0.24	0.24	0.24	0.24
Linear	0.33	0.31	0.29	0.27	0.25	0.23	0.21	0.19	0.17	0.15
Optimized at 2000Hz	0.26	0.2	0.63	0.26	0.23	0.2	0.14	0.24	0.11	0.14
Optimized at 2000-2500Hz	0.24	0.2	0.52	0.37	0.26	0.38	0.20	0.11	0.14	0.17

Based upon the DPO distributions of Table 4-4, the predicted SAC of different semi-open cellular metal samples are plotted in Figs. 4-13 and 4-14 for sole-frequency optimization and frequency-range optimization, respectively. Relative to uniform and linear DPO distributions, the most significant trend of the curve corresponding to the case of DPO distribution is the dramatic increase of the SAC over the wide frequency range (approximately below 2400 Hz). This again displays the superiority of the developed optimization strategy, which can not only achieve enhanced SAC at the selected sole frequency but also over the frequency range of interest.

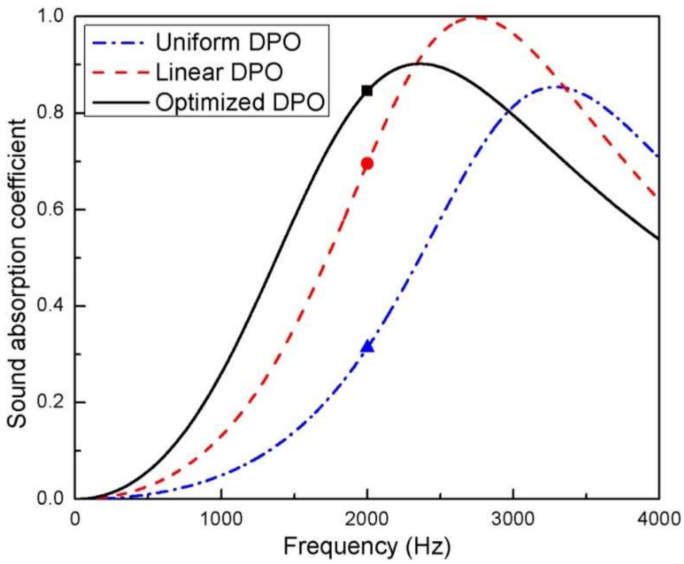

Fig. 4-13 SAC of semi-open cellular metal: Comparison amongst uniform, linear and sole-frequency (2000 Hz) optimized DPO distributions

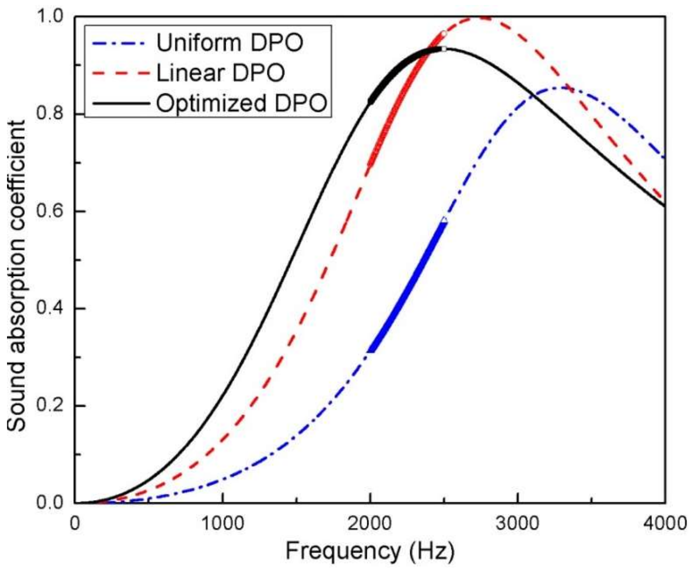

Fig. 4-14 SAC of semi-open cellular metal: Comparison amongst uniform, linear and frequency-range (2000-2500Hz) optimized DPO distributions

It should be pointed out that, the SAC of the linear case within the frequency range of 2400-2500 Hz is higher than that of the optimized case (see Fig. 4-14), which actually falls into the optimized frequency range of 2000-2500 Hz. However, this does not violate the optimal objective for maximum SAC because, within the optimized frequency range of 2000-2500 Hz, the averaged SAC of the optimized case still exceeds that of the linear case.

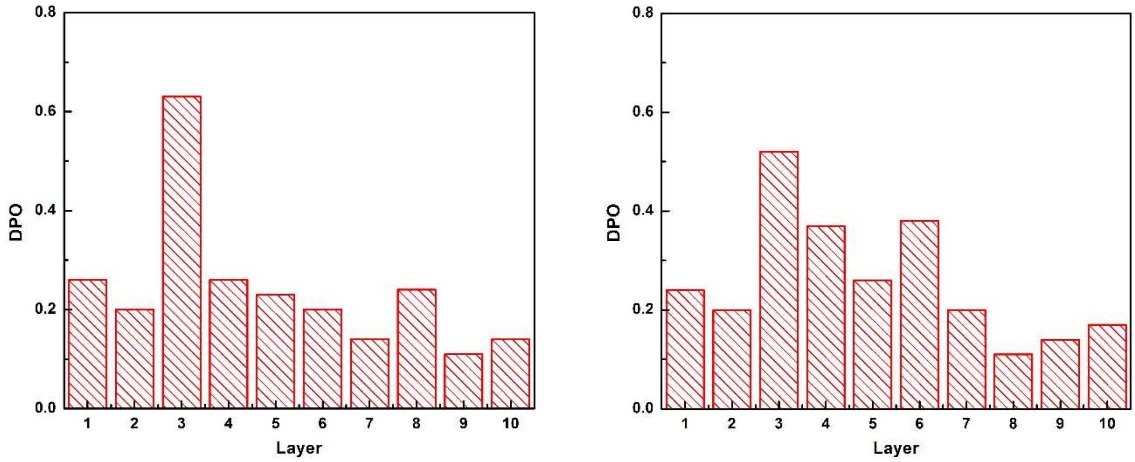

(a) (b)

Fig. 4-15 DPO distribution in DPO optimized semi-open cellular metals: (a) sole frequency optimization and (b) frequency-range optimization

The DPO distributions of the two DPO optimized semi-open cellular metal samples are shown in Figs. 4-15(a) and (b). It can be seen that DPOs fluctuate around 0.2 for all the layers of two optimized samples except Layer 3. The DPOs of Layer 3 of the two samples are much bigger than that of other layers.

4.5 Conclusions

Built upon the acoustic impedance of circular apertures and cylindrical cavities as well as the principle of electroacoustic analogy, an impedance model is proposed to describe the sound absorption performance of semi-open cellular metal having semi-open cells; the model predictions agree well with existing experimental measurements. To optimize the acoustic property of graded semi-open cellular metals, an optimization strategy on the basis of the genetic algorithm method is developed to define the objective functions and geometric constraint conditions in terms of key morphological parameters as design variables, including the porosity, the pore size and the degree of pore opening (DPO). To highlight the efficiency of the optimization strategy, uniform and linear distributions of the design variables are also considered subjected to the constraint of same mass and volume. It is demonstrated that, in terms of SAC, the graded distribution of each design variable is superior to uniform or linear distribution not only in the optimized frequency range but also in a wide frequency range of interest.

5 Sound Propagation In Micro Pores with Micron-sized Fiber Roughness

5.1 Introduction to micro pores with surface mounted fiber roughness

Sound propagation in cylindrical pores has been extensively investigated in the past century, due to its generalization to cover a wide range of porous acoustic materials. For instance, built upon the theoretically estimated influence of viscous and thermal effects on sound propagation in a cylindrical tube, a large number of theoretical models for sound propagation and absorption in porous materials have been developed. Therefore, to explore the influences of the surface roughness on the sound absorption of porous materials and their underlying mechanisms, a cylindrical micro-tube containing identical cylinders that are periodically distributed on its inner surface along both circumferential and axial directions (Fig. 5-1) is considered. Since the current study aims to reveal the influence of surface roughness on the acoustic properties of porous materials, the diameter of the micro-tube has sub-millimeter scale, approximating the pore size of typical acoustic materials. The length of the micro-tube (e.g., millimeter scale) is much larger than its diameter, so that end effects can be ignored for the micro-tube. The height and radius of the surface cylinders are smaller than the radius of the micro-tube so that they may be regarded as roughness elements here.

5.2 Theoretical and numerical models

For a cylindrical tube containing cylindrical roughness elements on its surface (Fig. 5-1), the tube may be divided into two distinct regions as shown in Fig. 5-1(b). Region I is the cylindrical part inside the dashed line, and region II is the part containing roughness elements located outside the dashed line.

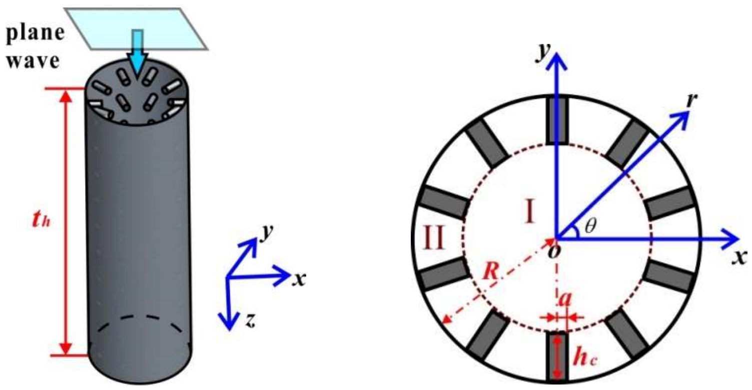

(a) (b)

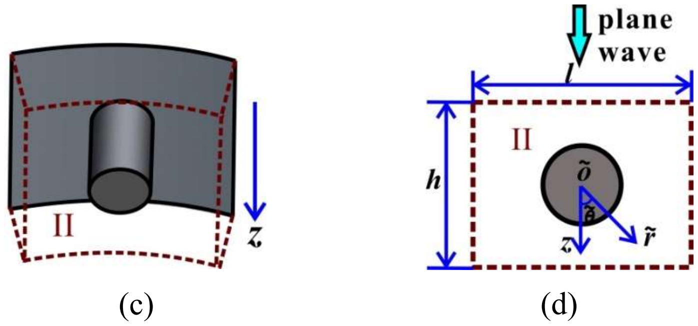

Fig. 5-1 Schematic of a cylindrical tube with micro-cylinder roughness elements periodically distributed on its inner surface: (a) overall view; (b) top view; (c) unit cell for cylindrical roughness element; (d) cross-section of cylindrical roughness element with rectangular outer boundary. (r,θ) are global polar coordinates and $(\tilde{r},\tilde{\theta})$ are local polar coordinates

5.2.1 Viscous effect characterization

To consider the viscous effect in the micro-tube with cylindrical roughness elements, the dynamic density $\rho_{eff}(\omega)$ of the micro-tube needs to be quantified, which is given as

$$\rho_{eff}(\omega)=\frac{-1}{i\omega}\frac{\partial p}{\partial z}\frac{1}{\overline{u}_z(\omega)} \tag{5-1}$$

where $i=\sqrt{-1}$, $\overline{u}_z(\omega)$ is the mean velocity in the micro-tube.

For a plane wave normally incident into the tube as shown in Fig. 5-1, a viscous boundary layer exists in the adjacent area of tube wall. Specifically, the viscous fluid has zero velocity at the fluid-solid interface, gradually becoming fully-developed flow when far from the tube wall. This viscous boundary layer is able to consume part of the sound energy. To account for this effect, the viscous Navier-Stokers equation is adopted to describe the viscous fluid velocity in region I, as:

$$\eta\Delta u_{\mathrm{I}z}(r,\omega)-i\omega\rho_0 u_{\mathrm{I}z}(r,\omega)=\frac{\partial p}{\partial z} \tag{5-2}$$

A general solution of the Navier-Stokes equation in region I is[39]

$$u_{\mathrm{I}z}(r,\omega)=\frac{-1}{i\omega\rho_0}\frac{\partial p}{\partial z}\left(1-AJ_0(\Lambda r)\right) \tag{5-3}$$

where $\Lambda=\sqrt{-i\omega\rho_0/\eta}$. $J_m(x)$ denotes the m th ($m=0,1,2,\ldots$) order of the first kind of Bessel function with complex variable x. $(r,\ \theta)$ are the global polar coordinates as shown in Fig. 5-1(b). A is an unknown coefficient to be determined by the boundary condition of region I.

At the interface between region I and region II, due to continuity of fluid velocity, the boundary condition of region I can be approximately written as:

$$u_{\mathrm{I}z}(r,\omega)\big|_{r=R-h_c}=\overline{v}_{\mathrm{II}z}(r,\omega)\big|_{r=R-h_c} \tag{5-4}$$

where R is the radius of cylindrical tube, h_c is the height of cylindrical roughness elements, and $\bar{v}_{\mathrm{II}z}(r,\omega)$ is the mean velocity of fluid flow around the cylindrical roughness elements in region II, as shown in Fig. 5-1(c).

When the radius of the roughness element is relatively small compared with that of the tube and a sufficiently large number of roughness elements are present in the cross-section of the tube, the outer boundary around the roughness elements may be approximately treated as plane rectangles, as shown in Fig. 5-1 (d). The width of the unit cell l can be approximately given as:

$$l(r) \approx \frac{2\pi r}{n} \tag{5-5}$$

where n is the number of roughness elements in the cross-section of the tube. The length of the unit cell, h, is equal to the distance between roughness elements in the z-direction.

To clearly calculate the fluid velocity around the cylinders in region II, a local polar coordinate system $(\tilde{r},\tilde{\theta})$ is established for the cylinder in region II, which is perpendicular to the axis of the cylinder, as shown in Fig. 5-1 (d). Consider next a sound wave that propagates normal to a cylinder of infinite length. When the cross-section of the cylinder is the same as the roughness element shown in Fig. 5-1(d), the velocity of the fluid at the cross-section of the cylinder can be written as[46,48]

$$\begin{aligned} v_{\tilde{r}0}(\tilde{r},\tilde{\theta},\omega) &= \left(\frac{E}{\tilde{r}^2}+1-\frac{B\eta}{i\omega\rho_0}\frac{g_1\left(\sqrt{i}\Lambda\tilde{r}\right)}{\tilde{r}}\right)U_0\cos\tilde{\theta} \\ v_{\tilde{\theta}0}(\tilde{r},\tilde{\theta},\omega) &= \left(\frac{E}{\tilde{r}^2}-1+\frac{B\eta}{i\omega\rho_0}\sqrt{\frac{\omega\rho_0}{\eta}}g_1'\left(\sqrt{i}\Lambda\tilde{r}\right)\right)U_0\sin\tilde{\theta} \end{aligned} \tag{5-6}$$

where $B=\dfrac{-2\Lambda}{ie^{3\pi i/4}g_0(i\Lambda a)}$, $E=\dfrac{2ag_1(i\Lambda a)}{i\Lambda e^{3\pi i/4}g_0(i\Lambda a)}-a^2$; $U_0=\dfrac{-1}{\rho_0 i\omega}\dfrac{\partial p}{\partial z}$ is the incidence velocity, and $g_1'(x)$ is the derivative of function $g_1(x)$. The function $g_m\left(\sqrt{i}\Lambda\tilde{r}\right)$ is given as[46]

$$g_m\left(\sqrt{i}\Lambda\tilde{r}\right)=Ke_m\left(\sqrt{i}\Lambda\tilde{r}\right)-\left(\frac{Ke_m\left(\sqrt{i}\Lambda\tilde{r}_{out}\right)}{Be_m\left(\sqrt{i}\Lambda\tilde{r}_{out}\right)}\right)Be_m\left(\sqrt{i}\Lambda\tilde{r}\right) \tag{5-7}$$

Where $Ke_m(x)=\mathrm{ker}_m(x)+i\mathrm{kei}_m(x)$, $Be_m(x)=\mathrm{ber}_m(x)+i\mathrm{bei}_m(x)$, (ker_m , kei_m , ber_m , bei_m) are the m th order of Kelvin functions, and $\tilde{r}_{out}$ is the distance from the center of the cylinder to the outer boundary. For the idealized rectangular outer boundary shown in Fig.5-1 (d), $\tilde{r}_{out}$ is:

$$\tilde{r}_{out}=\begin{cases} h/2\cos\tilde{\theta} & \tilde{\theta}\in\left(0,\ \mathrm{ac}\tan(l/h)\right) \\ l/2\sin\tilde{\theta} & \tilde{\theta}\in\left(\mathrm{ac}\tan(l/h),\ \pi\text{-}\mathrm{ac}\tan(l/h)\right) \\ -h/2\cos\tilde{\theta} & \tilde{\theta}\in\left(\pi\text{-}\mathrm{ac}\tan(l/h),\ \pi\right) \end{cases} \tag{5-8}$$

Eventually, the mean velocity at the cross-section of the cylinder in the z-direction can be calculated as:

$$\bar{v}_{0z}(\omega)=\frac{1}{lh-\pi a^2}\int_0^{2\pi}\int_a^{\tilde{r}_{out}}\left(v_{0\tilde{r}}\left(\tilde{r},\tilde{\theta}\right)\cos\tilde{\theta}-v_{0\tilde{\theta}}\left(\tilde{r},\tilde{\theta}\right)\sin\tilde{\theta}\right)\tilde{r}d\tilde{r}d\tilde{\theta} \tag{5-9}$$

Because the roughness elements have finite length (Fig. 5-2), the end wall effect upon fluid velocity should be considered. The velocity of laminar flow is parabolic inside the tube due to the zero velocity condition at the tube wall. Thus, to consider the influence of the tube wall, we assume that the incidence velocity is changed to be parabolic by the tube wall in region II, as:

$$U(r)=U_0\cdot K\left(1-\frac{r^2}{R^2}\right)\quad\left(R-h_c\le r\le R\right) \tag{5-10}$$

where K is an empirical parameter related to the ratio of the height of cylindrical roughness elements and the radius of the micro-tube, which can be quantified later by comparing the numerical results with the analytical results. With the modified incidence velocity, the velocity around the roughness elements in region II may be approximately written as:

$$\begin{aligned}
v_{\mathrm{II}\tilde{r}}\left(\tilde{r},\tilde{\theta},\omega,r\right)&=\left(\frac{E}{\tilde{r}^2}+1-\frac{B\eta}{i\omega\rho_0}\frac{g_1\left(\sqrt{i}\Lambda\tilde{r}\right)}{\tilde{r}}\right)U(r)\cos\tilde{\theta}=v_{\tilde{r}0}\left(\tilde{r},\tilde{\theta},\omega\right)K\left(1-\frac{r^2}{R^2}\right)\\
v_{\mathrm{II}\tilde{\theta}}\left(\tilde{r},\tilde{\theta},\omega,r\right)&=\left(\frac{E}{\tilde{r}^2}-1+\frac{B\eta}{i\omega\rho_0}\sqrt{\frac{\omega\rho_0}{\eta}}g_1'\left(\sqrt{i}\Lambda\tilde{r}\right)\right)U(r)\sin\tilde{\theta}=v_{\tilde{\theta}0}\left(\tilde{r},\tilde{\theta},\omega\right)K\left(1-\frac{r^2}{R^2}\right)
\end{aligned} \tag{5-11}$$

Thus the z-direction mean velocity at the cross-section of the cylindrical roughness elements in region II can be given as:

$$\bar{v}_{\mathrm{II}z}(r,\omega)=K\left(1-\frac{r^2}{R^2}\right)\bar{v}_{0z}(\omega) \tag{5-12}$$

Upon substituting Eq. (5-12) into Eq. (5-4), the boundary condition of region I in the micro-tube can be given as:

$$u_{\mathrm{I}z}(r,\omega)\Big|_{r=R-h_c}=\bar{v}_{\mathrm{II}z}(r,\omega)\Big|_{r=R-h_c}=K\left(1-\frac{\left(R-h_c\right)^2}{R^2}\right)\bar{v}_{0z}(\omega) \tag{5-13}$$

Substitution of Eq. (5-13) into Eq. (5-3) results in:

$$A=\left.\frac{\frac{-1}{i\omega\rho_0}\frac{\partial p}{\partial z}-\bar{v}_{\mathrm{II}z}(r,\omega)}{\frac{-1}{i\omega\rho_0}\frac{\partial p}{\partial z}J_0(\Lambda r)}\right|_{r=R-h_c} \tag{5-14}$$

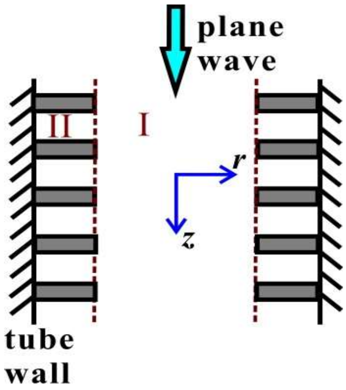

Fig. 5-2 Side view of unit cell for cylindrical roughness element

To validate Eqs. (5-12)-(5-14) and quantify the parameter K, a FE model is developed by using the Thermoacoustics Module of Comsol Multiphysics software, as shown in Fig. 5-3. In this FE model, the fluid in the micro-tube is taken as viscous creep flow, and the second-order Lagrange elements are applied for the velocity components. At the fluid-solid interfaces, no slip boundary condition is applied to ensure the zero velocity condition at the interfaces.

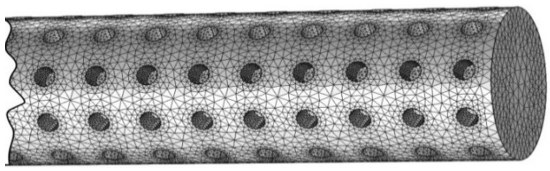

Fig. 5-3 Representative finite element model for micro-tube with surface roughness

When harmonic pressures p_{in} and p_{out} are imposed at the inlet and outlet of the tube, the pressure gradient is:

$$\frac{\partial p}{\partial z} \approx \frac{p_{in} - p_{out}}{t_h} \tag{5-15}$$

For a tube without surface roughness, the degraded FE model for velocity distribution in the tube can be validated by comparing the FE simulation results with the classical analytical formula[28]

$$u_{0z} = \frac{-1}{i\omega\rho_0} \frac{\partial p}{\partial z} \left(1 - \frac{\mathrm{J}_0(\Lambda r)}{\mathrm{J}_0(\Lambda R)} \right) \tag{5-16}$$

Figure 5-4(a) compares the absolute value of fluid velocity along the axial direction of the micro-tube without roughness elements obtained from the FE model and the classical formula of (5-16). Relevant material properties of air are the same as that listed in Table 2-1. The FE simulation results agree well with the classical formula, suggesting that it is feasible to use the FE model to calculate the velocity distribution in cylindrical tubes.

For a micro-tube containing cylindrical roughness elements, Fig. 5-4(b) compares the numerical and analytical velocities along its axial direction. It can be seen from Fig. 5-4(b) that the predictions of the present theoretical model match well with the FE calculation results for both region I and region II. Whereafter, by analyzing a large number of numerical and analytical results for velocity distributions in various micro-tubes with roughness elements, the empirical parameter K is obtained as a function of tube radius R and roughness height h_c, as:

$$K \approx -7.46\frac{h_c}{R}+4.69 \tag{5-17}$$

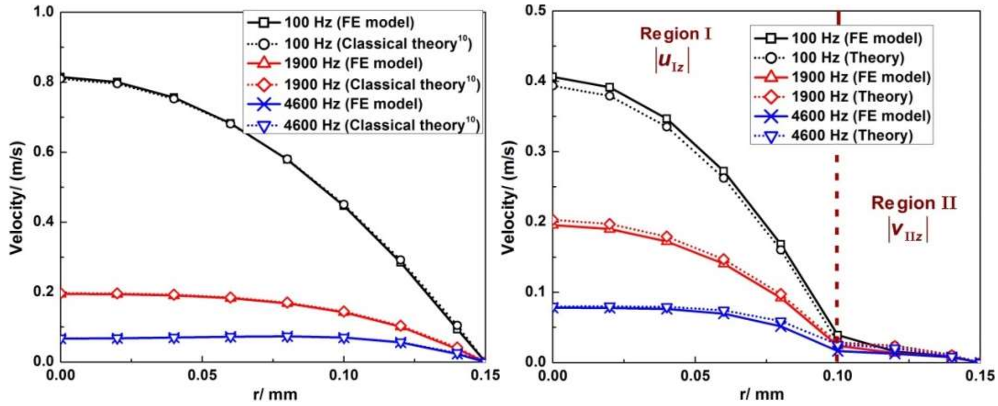

(a) (b)

Fig. 5-4 Absolute value of fluid velocity along radial direction of micro-tube: (a) without surface roughness and (b) with cylindrical roughness elements. Physical parameters of micro-tube are: $R=0.15$ mm, $t_h=10$ mm, $h_c=50$ μm, $h_c=50$ μm, $h_c=50$ μm, $a=10$ μm, $n=15$. The empirical number K is 2.2.

Finally, the mean velocity in a cylindrical tube with periodically placed surface roughness elements can be calculated as:

$$\bar{u}_z(\omega)=\frac{\int_0^{R-h_c} u_{\mathrm{I}z}(r,\omega)2\pi r dr h+\int_{R-h_c}^{R}\bar{v}_{\mathrm{II}z}(r,\omega)\left(2\pi rh-n\pi a^2\right)dr}{\pi R^2 h} \tag{5-18}$$

By substituting Eq. (5-18) into Eq. (5-1), the dynamic density of the composite tube can be obtained.

5.2.2 Thermal effect characterization

The thermal effect of a cylindrical tube with surface roughness elements is represented by the dynamic bulk modulus, given as

$$K_{eff}(\omega)=\frac{\gamma P_0}{\gamma-(\gamma-1)\bar{T}(\omega)\dfrac{\rho_0 c_p}{p}} \tag{5-19}$$

where $\bar{T}(\omega)$ is the mean temperature rise in the tube.

For sound propagating in the tube with surface roughness, the distribution of temperature rise in region I is governed by:

$$k_t\nabla^2 T_{\mathrm{I}}(r,\omega)-i\omega\rho_0 c_p T_{\mathrm{I}}(r,\omega)=-i\omega p \tag{5-20}$$

A general solution of the above thermal conduction equation in region I is expressed as[39]

$$T_{\mathrm{I}}(r,\omega)=\frac{p}{\rho_0 c_p}\left(1-H\mathrm{J}_0\left(\hat{\Lambda}r\right)\right) \tag{5-21}$$

Where $\hat{\Lambda}=\sqrt{\mathrm{Pr}\frac{-i\omega\rho_0}{\eta}}$ and H is an unknown coefficient to be determined by the boundary condition of region Ⅰ.

The temperature rise at the interface between region Ⅰ and Ⅱ can be estimated by:

$$T_{\mathrm{I}}(r,\omega)\Big|_{r=R-h_c}=\overline{\tau}_{\mathrm{II}}(r,\omega)\Big|_{r=R-h_c} \tag{5-22}$$

where $\overline{\tau}_{\mathrm{II}}(r,\omega)$ is the mean temperature rise for sound propagation around the roughness elements in region Ⅱ. Since temperature rise in the tube has the same mathematical form as that of velocity distribution[28], the temperature rise $\overline{\tau}_{\mathrm{II}}(r,\omega)$ can be written as:

$$\overline{\tau}_{\mathrm{II}}(r,\omega)\Big|_{r=R-h_c}=\frac{p}{\rho_0 c_p}\vartheta(r,\mathrm{Pr}\,\omega)\Big|_{r=R-h_c} \tag{5-23}$$

where $\vartheta(r,\omega)=\overline{v}_{\mathrm{II}z}(r,\omega)\Big/\left(\frac{-1}{i\omega\rho_0}\frac{\partial p}{\partial z}\right)$.

By substituting Eq. (5-23) into Eq. (5-21), the parameter H can be obtained as:

$$H=\left.\frac{1-\vartheta(r,\mathrm{Pr}\,\omega)}{\mathrm{J}_0\left(\hat{\Lambda}r\right)}\right|_{r=R-h_c} \tag{5-24}$$

To calculate the temperature rise in the micro-tubes, the FE model employed is the same as that for fluid velocity. Particularly, fluid-solid interfaces in the FE model are defined as acoustical rigid and isothermal wall, i.e., temperature rise of fluid is zero at the fluid-solid interfaces. The physical parameters used in the calculation are listed in Table 5-1. For comparison, the temperature rise in a micro-tube without surface roughness can be analytically predicted as[28]

$$T_0(r,\omega)=\frac{p}{\rho_0 c_p}\left(1-\frac{\mathrm{J}_0\left(\hat{\Lambda}r\right)}{\mathrm{J}_0\left(\hat{\Lambda}R\right)}\right) \tag{5-25}$$

As shown in Fig. 5-5(a), by comparing with the analytically predicted temperature rise, the FE model is validated in the context of thermal effect for smooth tubes. Figure 5-5(b) compares further the temperature rise in a micro-tube with roughness elements calculated by the FE method with that by the proposed theory. Good agreement is observed in both regions.

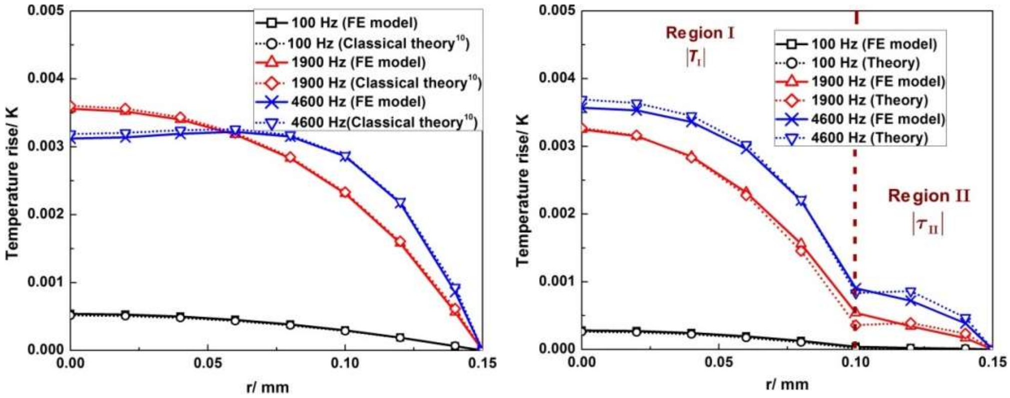

(a) (b)

Fig. 5-5 Absolute value of temperature rise along radial direction of micro-tube: (a) without surface roughness and (b) with cylindrical roughness elements. Physical parameters of micro-tube are: $R = 0.15$ mm, $t_h = 10$ mm, $h_c = 50$ μm, $h_c = 50$ μm, $h_c = 50$ μm, $a = 10$ μm, $n = 15$. The empirical number K is 2.2.

Based on Eqs. (5-21) to (5-23), the mean temperature rise in a cylindrical tube with roughness elements can be calculated by:

$$\bar{T}(\omega) = \frac{\int_0^{R-h_c} T_{\mathrm{I}}(r,\omega) 2\pi r dr + \int_{R-h_c}^{R} \bar{\tau}_{\mathrm{II}}(r,\omega)\left(2\pi r h - n\pi a^2\right) dr}{\pi R^2 h} \tag{5-26}$$

By substituting Eq. (5-26) into Eq. (5-19), the dynamic bulk modulus of the composite tube can be obtained.

5.2.3 Sound absorption

Finally, by combining the viscous and thermal effects, the characteristic impedance and propagation constant in a cylindrical tube with periodical roughness elements can be obtained as:

$$Z = \sqrt{\rho_{eff} K_{eff}}, \ \Gamma = i\omega \sqrt{\frac{\rho_{eff}}{K_{eff}}} \tag{5-27}$$

Correspondingly, the SAC of the tube is:

$$\alpha = 1 - \left| \frac{Z_f - \rho_0 c_0}{Z_f + \rho_0 c_0} \right|^2 \tag{5-28}$$

where Z_f is the surface impedance. For a rigid-backed tube of length t_h, the surface impedance is given by:

$$Z_f(\omega) = Z \coth\left(\Gamma(\omega) t_h\right) \tag{5-29}$$

5.3 Results and discussion

5.3.1 Influence of surface roughness on viscous and thermal effects

This section discusses the influence of surface roughness on the viscous and thermal effects of cylindrical tubes. Assume a plane wave is incident on a rigid-backed tube with roughness elements periodically distributed on its inner surface. The amplitude of the sound pressure is taken as 1 Pa, and the FE mesh developed for the tube is the same as that shown in Fig. 5-3. To explore the mechanisms of energy dissipation in the tube, the total energy dissipation and the energy dissipation densities by thermal and viscous effects in the axial cross-section of the tube are presented in Fig. 5-6. For comparison, the sound energy consumed by a cylindrical tube without inner surface roughness is also plotted in Fig. 5-6.

As shown in Fig. 5-6(b), the sound energy is most fiercely consumed at the solid-fluid interface in the smooth tube, decreasing as the distance from the interface is increased. In contrast, the sound energy is mostly consumed near the interface between region I and region II (Fig. 5-6(a)). To further compare the sound energy consumed in the tube with and without surface roughness, the energy dissipation density integrated over the whole cylindrical tube is presented in Fig. 5-7.

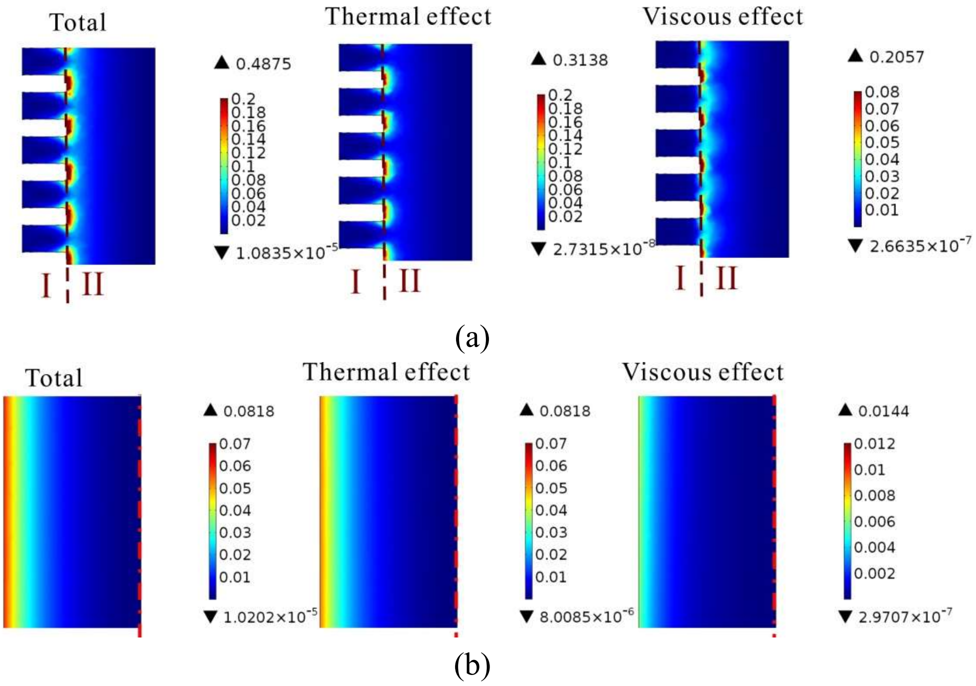

Fig. 5-6 Energy dissipation density ($\mathrm{W/m^3}$) in cylindrical micro-tube at 1900 Hz: (a) with roughness and (b) without roughness. Relevant physical parameters: $R = 0.15$ mm , $t_h = 4$ mm , $h_c = 50$ μm , $a = 10$ μm , $n = 15$.

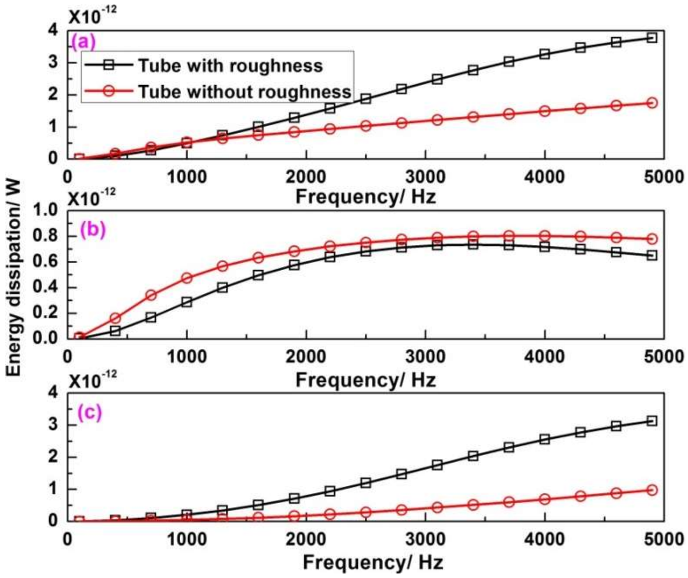

Fig. 5-7 Energy dissipation (W) in rigid-backed cylindrical micro-tubes with and without surface roughness: (a) total sound dissipation, (b) sound dissipation by thermal effect, and (c) sound dissipation by viscous effect. Relevant physical parameters: $R = 0.15$ mm , $t_h = 10$ mm , $h_c = 50$ μm , $a = 10$ μm , $n = 15$.

It can be seen from Fig. 5-7 that the sound energy consumed by thermal effect in the tube with roughness is smaller than that in the smooth tube, indicating that the thermal effect is weakened by roughness. However, the viscous effect is strengthened by roughness, as the sound energy consumed by viscous effect in the non-smooth tube is much bigger than that in the smooth tube. The influence of roughness on energy dissipation by viscous and thermal effects can be explained by comparing the fluid velocity and temperature rise in tubes with and without roughness as shown in Fig. 5-8.

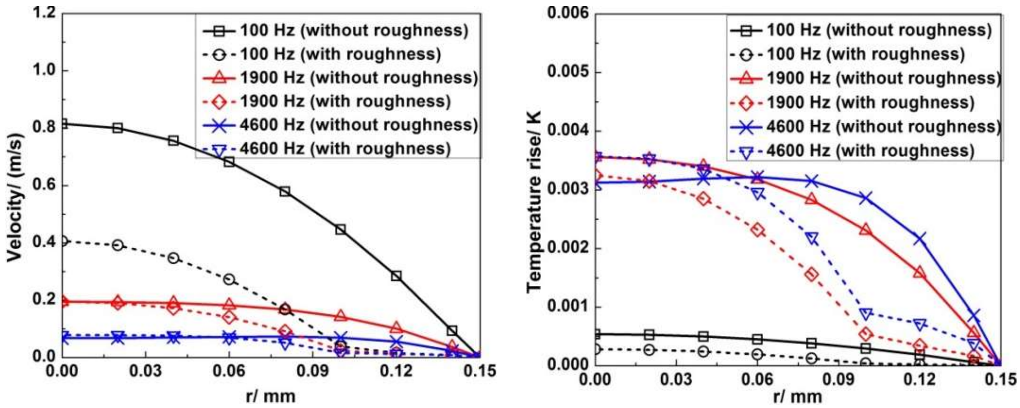

(a) (b)

Fig. 5-8 Comparison of velocity and temperature rise between cylindrical micro-tubes with and without roughness: (a) velocity and (b) temperature rise. Relevant physical parameters: $R = 0.15$ mm , $h_c = 50$ μm , $a = 10$ μm , $n = 15$.

Figure 5-8(a) shows that the fluid velocity is dramatically reduced by roughness, so that the energy dissipated by viscous effect is enlarged. The reduction of velocity is attributed to the increase of specific contact area by the roughness elements. For the present cylindrical tube with surface roughness as shown in Fig. 5-1, the specific contact area is:

$$S_{a1} = \frac{2Rh + 2ah_c n}{R^2 h} \tag{5-30}$$

In the absence of roughness, Eq. (5-30) becomes:

$$S_{a2} = \frac{2}{R} \tag{5-31}$$

Since S_{a1} is larger than S_{a2}, the velocity of a tube with roughness is smaller than that of a tube without roughness.

Figure 5-8(b) compares the temperature rises in micro-tubes with and without roughness elements. Similar to velocity, the presence of roughness decreases the temperature rise. As is known, the change of air temperature in the tube is accompanied with the compression and expansion of the air. With the same incident sound wave, air in a non-smooth tube is more difficult to be compressed due to reduced space, causing the temperature rise to decrease. Even though the temperature rise in the smooth tube is slightly smaller than that of tube with roughness within the range 0~0.05 mm at 4600 Hz, the mean temperature rise in the non-smooth tube is still much smaller than that of the smooth tube. The thermally dissipated sound energy of the air in the tube is dominated by temperature rise with the first kind heat transfer boundary condition. Since the temperature rise is reduced by surface roughness, the energy dissipated by the thermal effect inevitably decreases, as shown in Fig. 5-7(b).

5.3.2 Influence of roughness elements on SAC

This section aims to quantify the influence of roughness elements on the SAC of cylindrical tubes using the theoretical model developed in Section 5.2. To validate the theoretical model predictions, the SAC of the tubes is also calculated by the FE model. For convenience, a sound hard wall is placed at the end of the tube, to mimic a rigid-backed wall at the end of a porous material.

For sound absorption of tubes without roughness, to a large extent, the validity of the present FE model could be verified by comparing with the predictions obtained using the Allard-Atalla model[28]. In this model, the dynamic density of a tube without roughness is given by:

$$\rho_{eff} = \rho_0 \left(1 - \frac{2}{s\sqrt{-i}} \frac{J_1\left(s\sqrt{-i}\right)}{J_0\left(s\sqrt{-i}\right)} \right)^{-1} \tag{5-32}$$

where $s = \left(\omega\rho_0 R^2/\eta\right)^{0.5}$, and the dynamic bulk modulus of the tube without roughness is given by:

$$K_{eff} = \gamma P_0 \left(1 + (\gamma - 1) \frac{2}{\sqrt{\Pr} s\sqrt{-i}} \frac{J_1\left(\sqrt{\Pr} s\sqrt{-i}\right)}{J_0\left(\sqrt{\Pr} s\sqrt{-i}\right)} \right)^{-1} \tag{5-33}$$

Substitution of Eqs. (5-32) and (5-33) into Eqs. (5-27)-(5-29) leads to the SAC of a tube without roughness. For illustration, the numerically obtained SAC of such a tube (radius $R = 0.15$ mm, height $t_h = 10$ mm) is compared with that predicted by the Allard-Atalla model. It can be seen from Figs. 5-9 and 5-11 that the numerical results agree well with those of the Allard-Atalla model.

For tubes with roughness, the physical parameters used are listed in Table 5-1. The FE results are then compared with the predictions of the theoretical model detailed in Sec. 5.2, as shown in Figs. 5-9 and 5-11. Again, reasonably good agreement is achieved.

Table 5-1. Structural parameters of micro-tubes with cylindrical roughness elements

Sample number	h_c / R	n	h / R	a / R	$R(\text{mm})$
1#	0.333	15	0.333	0.0667	0.15
2#	0.267	15	0.333	0.0667	0.15
3#	0.267	15	0.333	0.05	0.15
4#	0.267	15	0.333	0.1	0.15

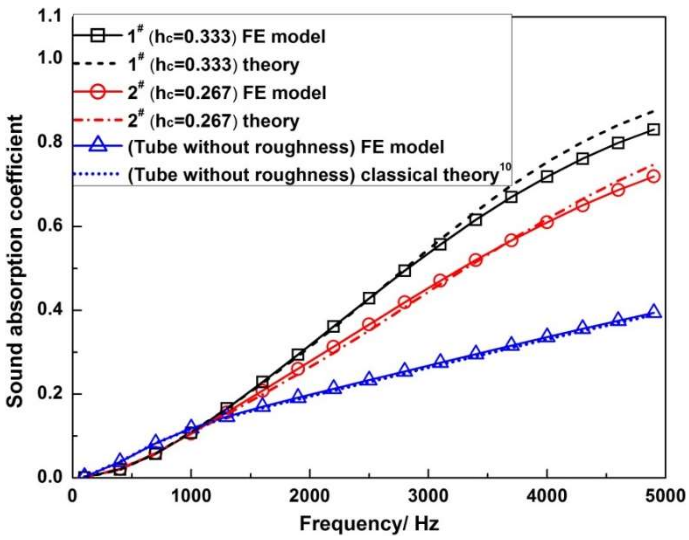

Fig. 5-9 Influence of roughness height on SAC

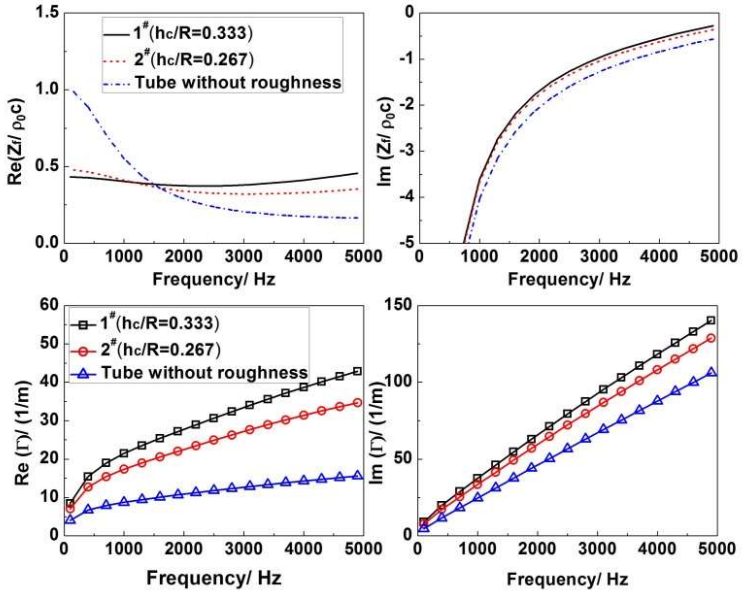

Fig.5-10 Influence of roughness height on surface impedance and propagation constant

The results of Figs. 5-9 and 5-11 also reveal how the height and radius of roughness elements affect SAC. Upon taking an overview of Figs. 5-9 and 5-11, the SAC of a tube with roughness is remarkably larger at frequencies beyond ~1200 Hz but slightly lower at frequencies below ~1200 Hz than that without roughness. As shown in Figs. 5-10 and 5-12, this phenomenon could be explained by comparing the surface impedances and propagation constants of sound wave in the tubes calculated using the present theoretical model. The real part of the surface impedance denotes acoustic resistance, which mainly causes sound energy dissipation. The absolute value of the imaginary part of the surface impedance represents acoustic reactance, which mainly induces reflection of a sound wave. Besides, the real part of the propagation constant represents actually the attenuation coefficient, and the sound energy can be more easily consumed with a larger attenuation coefficient. It is seen from Figs. 5-10 and 5-12 that the absolute value of the imaginary part of the surface impedance of a non-smooth tube is smaller than that of a smooth tube, while the real part of the surface impedance of a tube with roughness is bigger than that without roughness at frequencies beyond 1200 Hz. This means that, in the presence of roughness elements, sound dissipation is improved while sound reflection is weakened. Accordingly, the SAC of a non-smooth tube is bigger than that of a smooth tube at these frequencies. At frequencies below 1200 Hz, the real part of the surface impedance of a tube with roughness is much smaller than that without roughness. In other words, sound dissipation is weakened by the existence of roughness, thus the sound absorption coefficient of a tube with roughness is smaller than that without roughness. This can also be explained by the results of Fig. 5-7, that is, roughness increases the energy consumed by the viscous effect and decreases the energy dissipated by the thermal effect. By combining the two effects together, the total sound absorption is reduced at frequencies below ~1200 Hz and is enlarged at frequencies beyond ~1200 Hz.

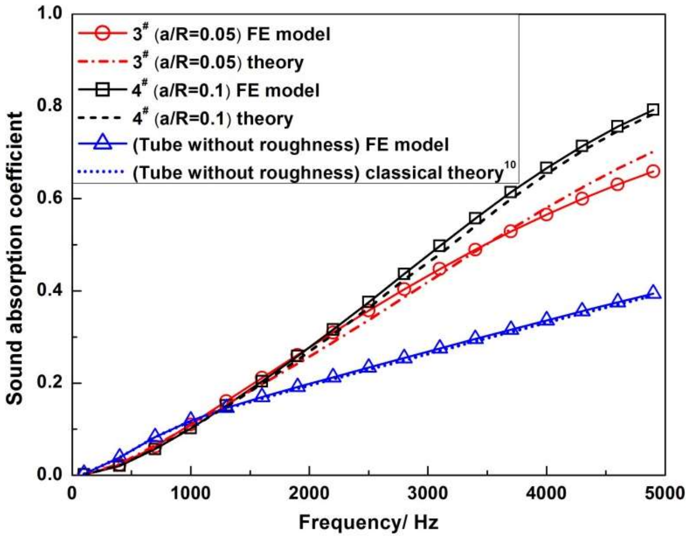

Fig.5-11 Influence of radius of roughness elements on SAC

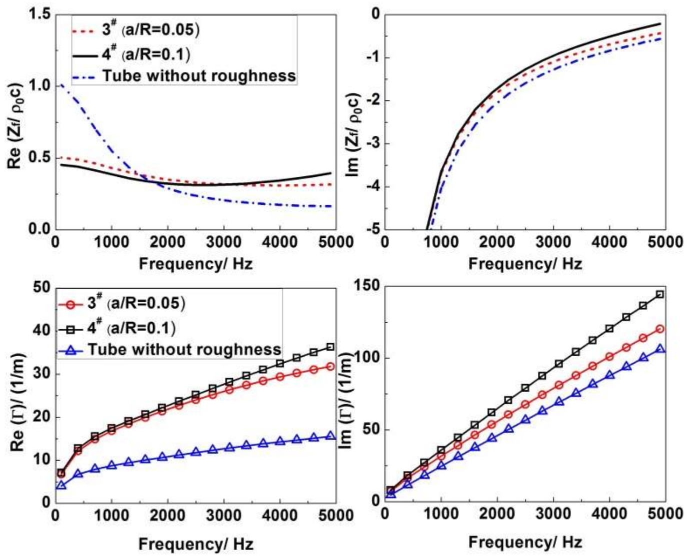

Fig.5-12 Influence of radius of roughness elements on surface impedance and propagation constant

Note that 1200 Hz is not a critical frequency. This particular frequency is just related to the geometrical and material parameters considered in the present case study. When these parameters are changed, this frequency will also change. As shown in Section 5.2, the velocity and temperature rise in the composite tube highly depend on the geometrical parameters of the roughness elements. Therefore, the dynamic density and bulk modulus of the tube also depend on these geometrical parameters, resulting in the dependence of SAC on geometrical parameters.

Figure 5-9 also shows that, as the height of roughness elements is increased, the SAC increases at frequencies beyond 1200 Hz, because the acoustic resistance and attenuation coefficient increase while the acoustic reactance decreases. The results presented in Fig.5-11 demonstrate that the SAC increases when the radius of roughness elements is increased at relatively high frequencies. Further, as shown in Fig. 5-12, upon increasing the radius of roughness elements, the acoustic resistance and attenuation increase, the reactance decreases, so that more sound energy will be dissipated.

5.4 Summary

A theoretical model is developed for sound propagation in cylindrical micro-tubes containing periodically placed cylindrical surface roughness elements, with both the viscous and thermal effects accounted for. To determine the fluid velocity around each roughness element, in addition to the zero velocity condition at tube wall, an approximate velocity continuity condition is applied, i.e., the velocity at the top of the roughness element equals the mean velocity of fluid flow inside the tube along its axial direction. Similarly, based on the approximate temperature at the top of the cylindrical roughness and the zero temperature rise condition at the tube walls, the distribution of temperature rise and the mean temperature rise in the tube are obtained. The theoretical model is validated by comparing with finite element simulation results, with good agreement achieved.

On the basis of the developed theoretical model, numerical calculations are carried out to explore the influence of roughness geometry. The presence of roughness improves the acoustic resistance and attenuation coefficient of micro-tubes over a wide frequency, leading to enlarged SAC. Also, increasing the height, radius and number of the roughness elements can improve the acoustic resistance, the attenuation coefficient and the sound absorption. The results of this study can inspire researchers to design superior sound absorption materials by artificially enlarging the surface roughness of existing porous materials, such as micro-perforated plates, fibrous materials and open-cell foams.

6 Low Frequency Sound Absorption Coefficient and Sound Transmission Loss of Perforated corrugated Sandwich Panels

6.1 Description of perforated corrugated sandwich panels (PCSP)

Figure 6-1 presents 4 kinds of corrugated sandwich panels with different perforation configurations. The sample in Fig. 6-1(a) represents classical corrugated sandwich panels without perforation. The wall thicknesses of the two face plates and the corrugated core are h_1, h_2 and t , respectively. The distance between the two face plates is H. The inclination angle of the corrugated core is φ, and the width of the unit cell of the corrugated core is L. Samples in Figs. 6-1(b)-(d) have perforated pores of submillimeter~millimeter scale in the upper face plate, in the corrugated core, and in both the upper face and the core, respectively. The diameters of perforated pores in the face plate and the corrugated core are d_1 and d_2 respectively. It is noted that for all these corrugated sandwich panels, no perforated pores exist on the lower face plate to achieve more effective sound transmission loss (STL).

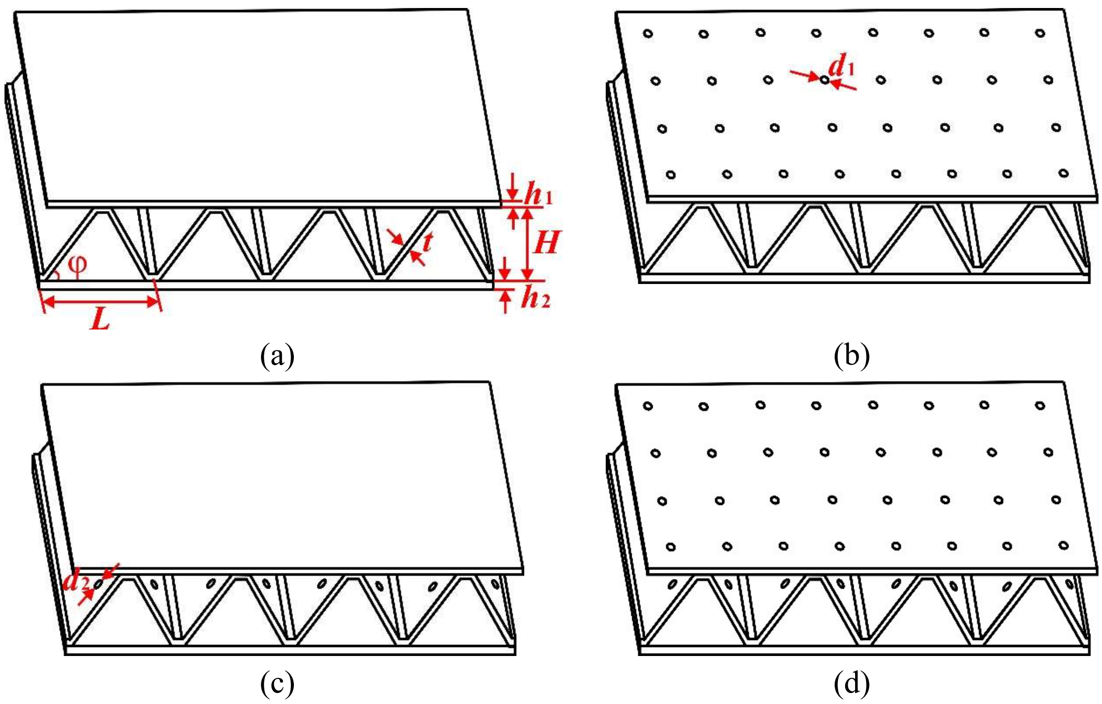

Fig. 6-1 Schematic of classical corrugated sandwich panel and corrugated sandwich panels with various perforation configurations

6.2 Finite element (FE) model for the sound propagation in PCSPs

When a plane wave impinges on the upper face plate, the acoustical properties of the corrugated sandwich panel can be calculated by the FE model shown in Fig. 6-2. The FE model is set up by using COMSOL Multiphysics. The plane wave is applied to the incidence field. The Perfectly Match layer (PML) is a domain that can absorb all the energy entering into it, and waves impinge on the PML from other non-PML domains won't be reflected. Therefore, two Perfectly Match layers (PML) are added to the ends of incident and the transmitted fields to simulate infinite and non-reflecting acoustic domain.

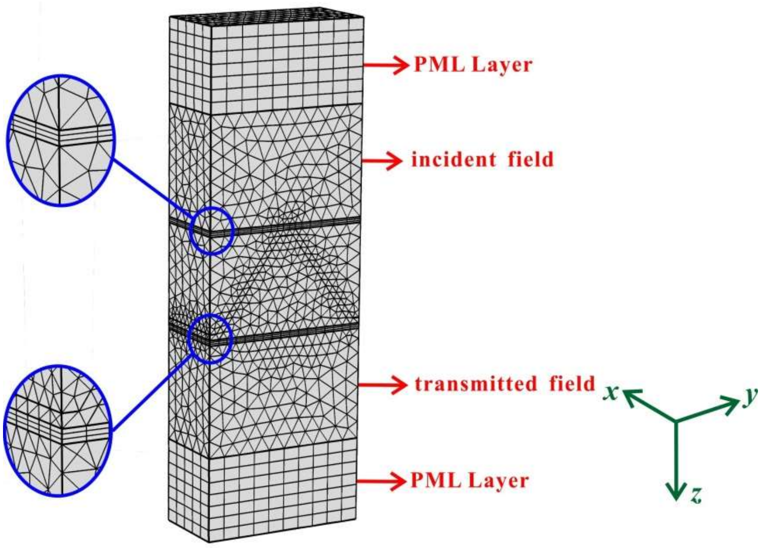

Fig. 6-2 Finite element model of a unit cell of corrugated sandwich panel

The air in the incident, transmitted and middle fields is compressible but lossless flow, with no thermal conductivity and viscosity considered. Thus the 'Pressure Acoustics' module of COMSOL, which is suited for all frequency-domain simulations with harmonic variations of the pressure field, is applied. The sound pressure is governed by the Helmholtz equation in this module:

$$\nabla^2 p = \frac{1}{c_0^2}\frac{\partial^2 p}{\partial t^2} \tag{6-1}$$

where t is the time.

The solid components of the structures are taken as isotropic linear elastic materials, with the 'Solid Mechanics' module of COMOL applied during the simulation. The displacement of the panel is governed by:

$$-\rho\omega^2\mathbf{u} - \frac{1}{2}\nabla\cdot\mathbf{C}:\left(\left(\nabla\mathbf{u}\right)^{\mathrm{T}} + \nabla\mathbf{u}\right) = 0 \tag{6-2}$$

where $\mathbf{u}$ represents the displacement of the solid panel, ρ is the density of the solid panel, $:$ represents double contraction, $\mathbf{C}$ is the elastic tensor of the panel material, which actually can be expressed by two elastic constants (i.e., the Young's modulus and the Poisson ratio) for isotropic elastic material.

As to the air inside the small pores, the radius of the pores is of comparable size with the thermal boundary thickness and viscous boundary thickness at low frequencies, which means the thermal conduction and viscosity should be considered during the simulation. Therefore, the 'Thermal-Acoustics' module is applied. The sound pressure, temperature, and particle velocity are governed by three equations, namely, the linear Navier-Stokes equation, the mass continuity equation, and the heat conduction equation in this module:

$$
\begin{aligned}
& i\omega\rho_0\mathbf{v}=\nabla\cdot\left(-P_t\mathbf{I}+\eta\left(\nabla\mathbf{v}+(\nabla\mathbf{v})^{\mathrm{T}}\right)-\frac{2}{3}\eta(\nabla\cdot\mathbf{v})\mathbf{I}\right) \\
& i\omega\rho_0\left(\frac{P_t}{P_0}-\frac{T}{T_0}\right)+\rho_0\nabla\cdot\mathbf{v}=0 \\
& i\omega\rho_0 C_p T=-\nabla\cdot(-k_T\nabla T)+i\omega P_t
\end{aligned}
\tag{6-3}
$$

where $\mathbf{v}$ is the fluid velocity, P_t is the sound pressure of the thermal-acoustic field, $\mathbf{I}$ is the identity matrix.

At the interface of the pressure acoustic field and solid panel, the normal accelerations of the air and panel are the same in the FE model, given as

$$
\begin{aligned}
& -\mathbf{n}\cdot\left(\frac{-1}{\rho_0}\nabla P\right)=-\mathbf{n}\cdot\mathbf{a}_t \\
& \mathbf{F}_A=P\mathbf{n}
\end{aligned}
\tag{6-4}
$$

where $\mathbf{n}$ is the surface normal direction, $\mathbf{a}_t$ is the acceleration of the solid panel. $\mathbf{F}_A$ is the total load of solid panel, which is decided by the normal sound pressure exerted on the panel.

While at the interface of the thermal acoustic field and pressure acoustic field, the continuous normal stress and acceleration and adiabatic conditions are applied in the FE model, as

$$
\begin{aligned}
& \left(-P_t\mathbf{I}+\eta\left(\nabla\mathbf{v}+(\nabla\mathbf{v})^{\mathrm{T}}\right)-\frac{2}{3}\eta(\nabla\cdot\mathbf{v})\mathbf{I}\right)\mathbf{n}=-P\mathbf{n} \\
& -\mathbf{n}\cdot\left(\frac{-1}{\rho_0}\nabla P\right)=-\mathbf{n}\cdot i\omega\mathbf{v} \\
& -\mathbf{n}\cdot(-K_T\nabla T)=0
\end{aligned}
\tag{6-5}
$$

As to the thermal acoustic field and solid panel coupling boundary, the velocity of the air is identical to that of the solid panel and the temperature variation is isothermal at the interface of the two fields in the FE model,

$$
\begin{aligned}
& \mathbf{v}=i\omega\mathbf{u} \\
& T=0
\end{aligned}
\tag{6-6}
$$

For corrugated sandwich panels of infinite size, FE simulations can be conducted using a unit cell with periodic boundary conditions as shown in Fig. 6-2. In contrast, for panels of finite size, the whole panel with actual boundaries should be embodied in the FE model. Model settings for the air and solid frame previously mentioned are applicable for both infinite and finite sized samples. Most part of the FE model is meshed by tetrahedral elements except from the plates and PML as shown in Fig. 6-2. The PMLs use the swept mesh method to create triangular prism elements as suggested in the User's Guide Manual of Comsol. The plates are also meshed by the swept mesh method due to the high transverse length to thickness ratio. Elements sizes changes with the dimension of each part.

The energy of sound is divided into three parts during its propagation through the composite panel, as:

$$E = E_{ref} + E_{trans} + E_{absorp} \tag{6-7}$$

where E_{ref} denotes the reflected energy in the incident field, E_{trans} denotes the transmitted energy in the transmitted sound field, while E_{absorp} denotes the absorbed energy inside the sandwich panel. In the FE model, a normal incidence sound wave with pressure $P_i = e^{-ik_0 z}$ is incident on the surface of the panel, thus the total sound energy is:

$$E = \frac{1}{2}\mathrm{Re}\int_S P_i \cdot v_i^* dS \tag{6-8}$$

where $k_0 = \frac{\omega}{c_0}$, S is the area of incidence plane of the FE model. v_i is the velocity of incident wave, given as

$$v_i = \frac{-1}{i\omega\rho_0}\frac{\partial P_i}{\partial z} = \frac{e^{-ik_0 z}}{\rho_0 c_0} \tag{6-9}$$

The reflected sound energy E_{ref} is calculated by:

$$E_{ref} = \frac{1}{2}\mathrm{Re}\int_S \left\{ (P_1 - P_i)\cdot(-v_1 + v_i)^* \right\} dS \tag{6-10}$$

where P_1 and v_1 are the total sound pressure and velocity at the surface of the top face plate in the incident field. $(P_1 - P_i)$, $(-v_1 + v_i)$ represent the reflected sound pressure and velocity at the surface of the top face plate in the incident field respectively.

The transmitted energy E_{trans} is given as:

$$E_{trans} = \frac{1}{2}\mathrm{Re}\int_S P_3 \cdot v_3^* dS \tag{6-11}$$

where P_3 and v_3 are the sound pressure and velocity at the surface of the bottom face plate in the transmitted field. Hence, the STL can be obtained as:

$$\mathrm{STL} = 10\log_{10}\frac{E}{E_{trans}} \tag{6-12}$$

while the SAC is written as:

$$\mathrm{SAC} = 1 - \frac{E_{trans}}{E} - \frac{E_{ref}}{E} \tag{6-13}$$

6.3 Validation of the FE model

6.3.1 SAC and STL measurement by impedance tube

Experimental measurements were performed to validate the FE models by using the four microphones B&K standing wave tube with the two load method shown in Fig. 6-3. A loudspeaker mounted at the end of the tube was set to generate a random noise signal over the frequency span of 100~1600 Hz. Four microphones were installed at four measuring positions to measure the frequency response functions. Notice that B&K 4206 large tubes with a diameter of 100 mm were chosen, suitable for low frequency measurement (100~1600 Hz). As shown in Fig. 6-3 (a), distances between microphones s_1 and s_2 are 50 mm, and distances between the tested sample and microphones m_1 and m_2 are 100 mm and 250 mm respectively. The two-cavity method developed by Bolton *et al*.[144] was applied to obtain the acoustic properties of the tested samples. The transfer matrix elements were solved by two independent measurements, conducted separately with open tube termination and anechoic termination. The fully absorbing termination was created with 3 standard sound absorbing samples having an approximately 75 mm depth in total.

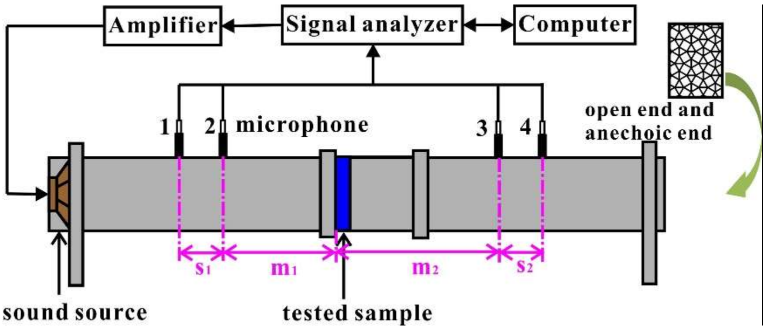

(a)

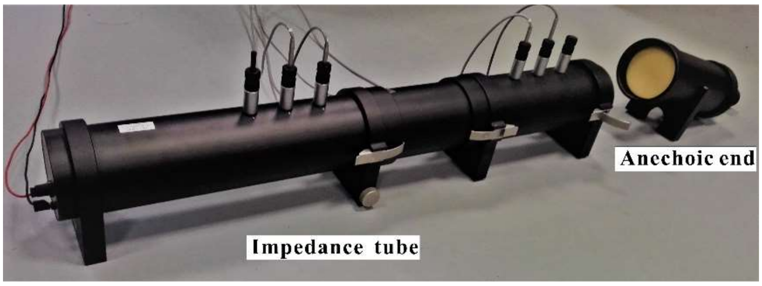

(b)

Fig. 6-3 (a) Schematic of the experimental system, (b) Photograph of the impedance tube

6.3.2 Manufacturing of experimental samples by 3D printing method

Perforations in the PCSPs are micro-sized that makes the manufacture of experimental samples extremely difficult by conventional manufacturing methods. Hence, the additive manufacturing (also known as 3D printing) is employed to fabricate the PCSPs. In an additive manufacturing progress, the expected structure is created by laying down thin layers of materials according to the digital CAD models. Nowadays, there exist many different kinds of 3D printers, including direct metal laser sintering (DMLS), selective laser melting (SLM), fused deposition modeling (FDM), etc.[145]. These 3D printers can create objects from many materials, plastics, sandstones, porcelains, pure metals, alloys and almost everything in-between. The additive manufacturing can not only print structures with elaborate shapes, it is also a more time-saving method than conventional manufacturing methods for single or small batch production[146-149].

Figure 6-4 shows the four test samples A$^{\#}$, B$^{\#}$, C$^{\#}$ and D$^{\#}$ fabricated by a FDM 3D printer, corresponding to the four types of panel in Fig. 6-1. The samples have a density of 958 kg/m3, Young's modulus of 1 GPa and Poisson' ratio of 0.35. Geometrical parameters of the samples are listed in Table 6-1. The perforation ratio in Table 6-1 is defined as the ratio of the area of the perforated pores to the area of the sandwich panels.

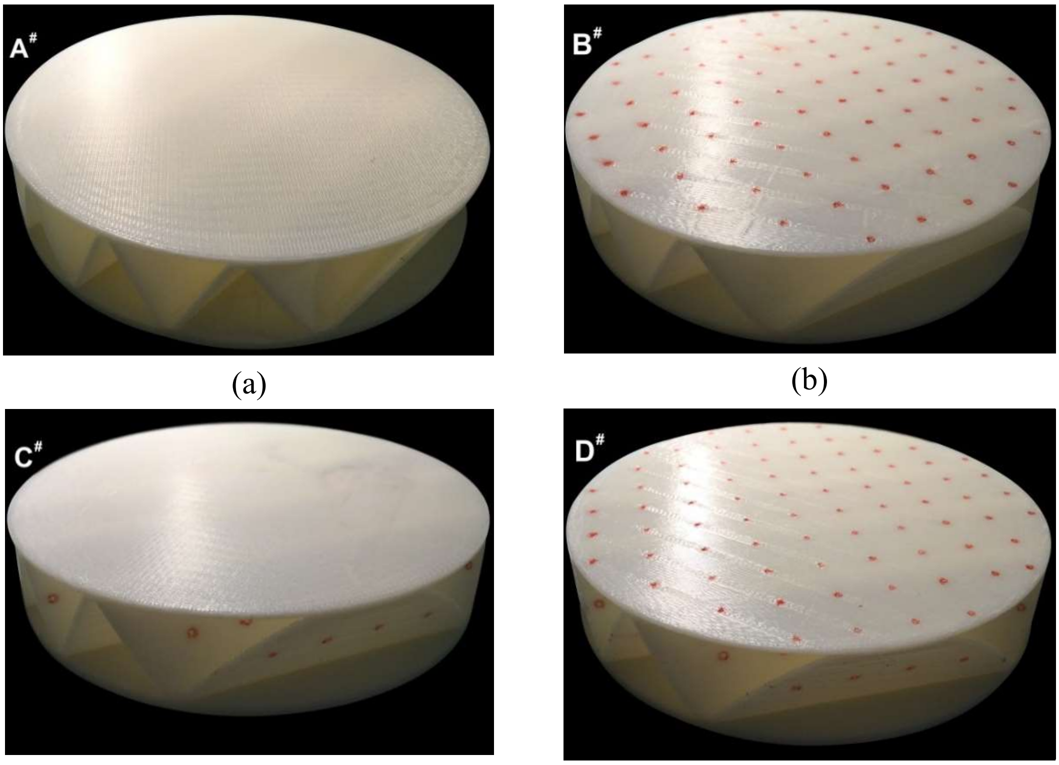

(a) (b) (c) (d)

Fig. 6-4 Pictures of corrugated sandwich panel samples for impedance tube test, (a) Samples A#, (b) Sample B#, (c) Sample C#, (d) Sample D#

Table 6-1 Geometrical parameters of corrugated sandwich samples for experiment

Parameters	**Value**
face plate thicknesses	$h_1 = 1$ mm
	$h_2 = 2$ mm
distance between face plates	$H = 17$ mm
perforation ratios	σ_1=σ_2=0.78%
pores diameters	$d_1 = d_2 = 1$ mm
thickness of core plate	$t = 1$ mm
inclination angle of core plate	φ=63.4°
unit cell width of core	$L = 20$ mm

6.3.3 Comparison between the experimental and FE results

During the measurement, the samples were fixed in the tube. FE models of finite size identical to the tested samples are set up (see Fig. 6-5) by applying the FE method presented in the previous section. Fixed constrains and sound hard wall boundary conditions are applied to the boundaries of the solid panel and pressure acoustic field of the FE models respectively. The meshes of the calculated FE models are shown in Fig. 6-5 with the convergences checked by mesh refinement. Physical parameters of the air are shown in Table 2-1.

Figure 6-6 compares the measured STLs with those obtained from FE simulations. The experimental data agree well with the simulation results for all four samples, demonstrating that the FE method presented is effective to estimate the acoustical properties of corrugated sandwich panels with or without perforations. It is noted that different from the infinite sized samples, the stiffness of finite sized tested samples is enhanced by the fixed boundary conditions, thus the sound transmission loss decreases with frequency within the stiffness controlled frequency region until the first structural resonance frequency. The first structural resonance frequencies for these samples exist around 2000 Hz which exceeds the tested frequency range, so the sound transmission loss drops with frequency as shown in Fig. 6-6. The deviations between simulation and experimental STLs at low frequencies are mainly introduced by the non-ideal experimental conditions, including air leaks at the interface between sample edges and impedance tube, measuring errors by microphones, etc.

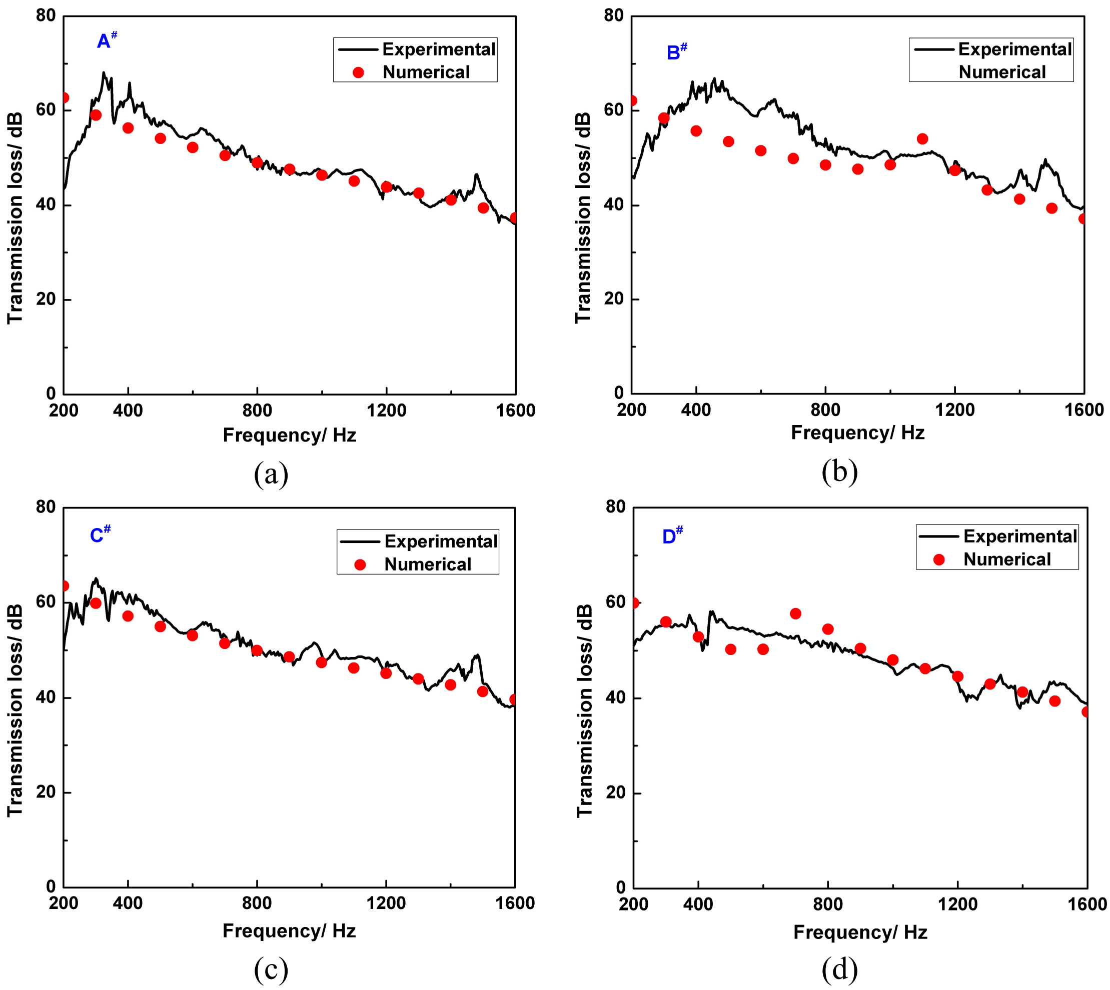

Fig. 6-6 Comparison between the STLs obtained by FE simulation and experimental measurement, (a) Samples A#, (b) Sample B#, (c) Sample C#, (d) Sample D#

The comparisons between the SACs by FE simulations and experiments are shown in Fig. 6-7(a)-(d). It can be seen from Fig. 6-7 that the FE simulations can give reasonable estimations for the SACs. For Samples A$^{\#}$ and C$^{\#}$, both the SACs by FE simulation and experiments are close to zero. For Samples B and D, the SACs by FE simulations capture the resonances frequencies precisely, however, the bandwidths of measured SACs are bigger than simulation results. The discrepancies of the bandwidth are mainly caused by the inevitable manufacturing errors, such as the irregular edge shapes of the perforated pores and extra mini pores adjacent to perforated pores. Besides, the peak values in the experimental SAC curves are smaller than that in the numerical SAC curves, which should be attributed to the non-ideal experimental conditions. In addition, discrepancies are also introduced by assumptions of the FE models. For instance, density fluctuation of the air by the temperature variation is ignored in FE models, fixed boundary conditions are ideally assumed without any air leaks during simulation process.

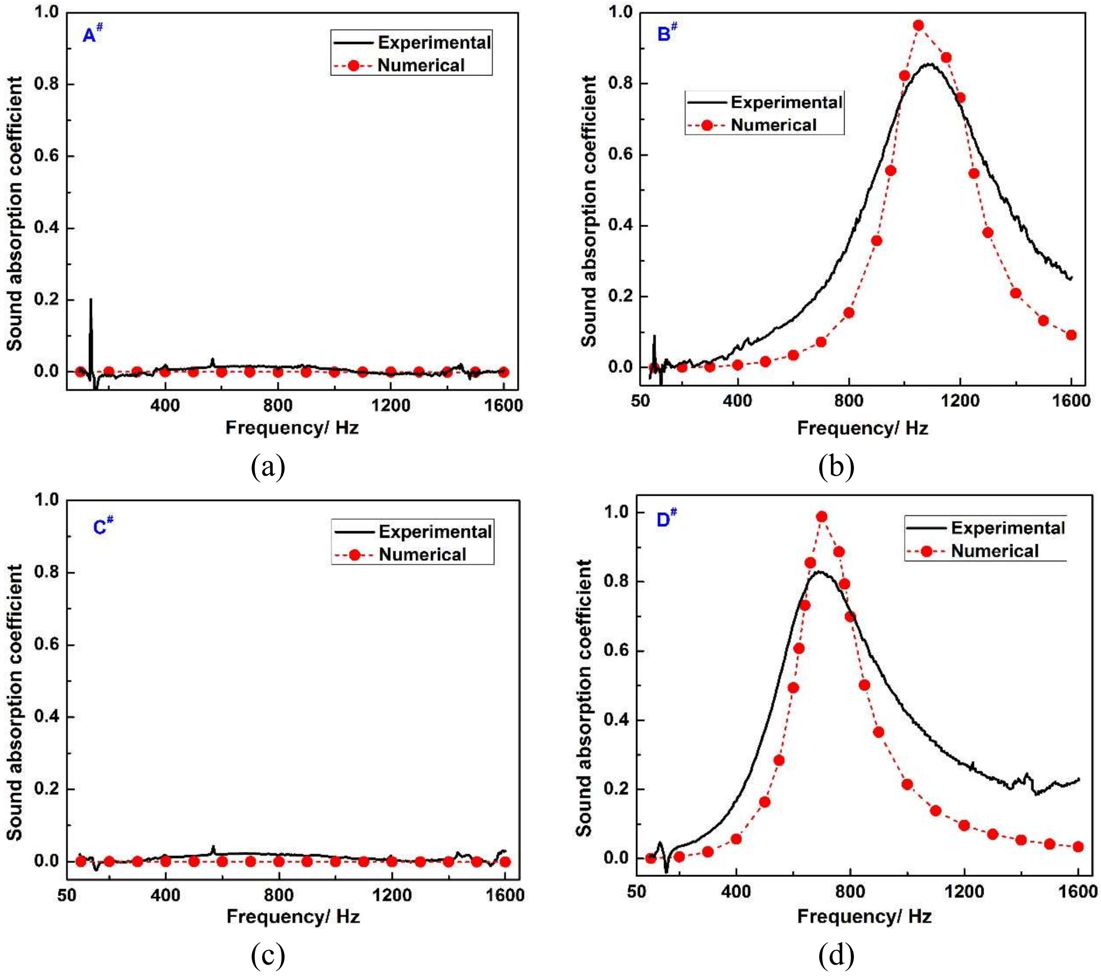

Fig. 6-7 Comparison between the SACs obtained by FE simulation and experimental measurement, (a) Samples A$^{\#}$, (b) Sample B$^{\#}$, (c) Sample C$^{\#}$, (d) Sample D$^{\#}$

6.4 Results and discussions

6.4.1 Influence of perforation configurations

Based on the FE models proposed and validated in previous sections, the STL and SAC of the four kinds of corrugated sandwich panels are compared next. For simplification, sandwich panels of infinite size are considered. These panels are assumed to be made of aluminum with a density of 2700 kg/m^3, Young's modulus of 70 GPa, and Poisson's ratio of 0.33.

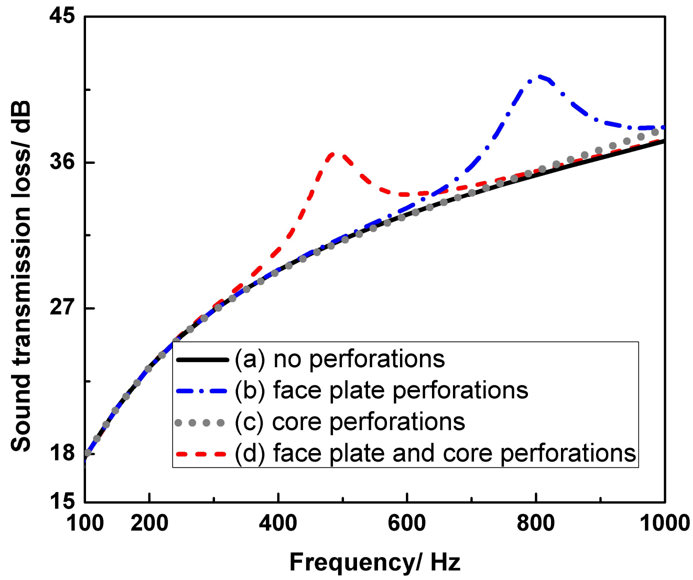

Fig. 6-8 STL comparison among corrugated sandwich panels with different perforation configurations

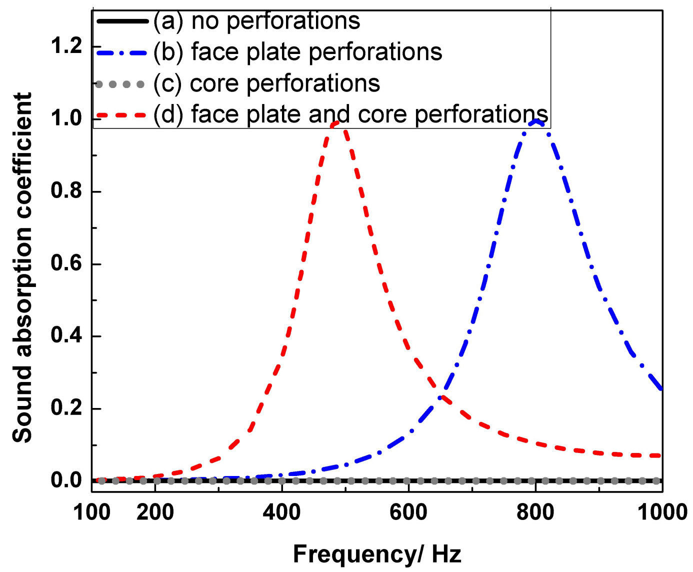

Fig. 6-9 SAC comparison among corrugated sandwich panels with different perforation configurations

Table 6-2 Geometrical parameters of the calculated corrugated sandwich panels

Parameters	Value
face plates thicknesses	$h_1 = h_2 = 1$ mm
distance between face plates	$H = 18$ mm

perforation ratios	σ_1=σ_2=0.349%
pores diameters	$d_1 = d_2 = 1$ mm
thickness of core plate	$t = 1$ mm
inclination angle of the core	φ=54.8°
unit cell width of the core	$L = 30$ mm

The STL and SAC of the classical corrugated sandwich panel are compared with those of corrugated sandwich panels with various perforation configurations in Fig. 6-8 and Fig. 6-9, with the geometrical parameters of these panels listed in Table 6-2. It can be seen that, compared with classical panels, panels with perforations in the face plate have better SAC and STL at low frequencies, while those with perforations only in the corrugated core have almost identical STL and SAC curves. For panels with face plate perforations, the sound waves can enter the small pores during propagation. As a result, the SAC can be dramatically enlarged since the sound energy is consumed by viscous and thermal dissipations inside the pores. Due to the improvement of absorbed energy, the transmitted energy is reduced and hence the STL is enlarged. On the contrary, for a panel with perforations only in the core, most of the sound is reflected by the upper face plate. Correspondingly, the SAC is negligibly small and no improvement occurs in the STL. Besides, it also can be seen that acoustical resonance frequencies exist in the SAC and STL curves of panels with face plate perforations. Panel with perforations in both the face plate and the core have lower acoustical resonance frequency than that of panel with only face plate perforations.

It can be concluded that perforations have great influence on the STL and SAC of corrugated sandwich panels, with those having perforations both in the face plate and the core exhibiting the best acoustic performance at low frequencies. Hence, further study of the perforations is conducted based on panels with both face plate and core perforations. The effects of pore diameter and pore size are discussed in the following section.

6.4.2 Influence of pore diameter

Figure 6-10 compares the STL and SAC of three corrugated sandwich panels having identical geometrical parameters (as listed in Table 6-2) apart from the perforated pore diameters. For all the three sandwich panels, the pore diameters are uniformly distributed, namely, the diameter of pores in the face plate is equal to that in the corrugated core. It can be seen from Fig. 6-10 that, with decreasing pore diameter, the bandwidth of SAC increases. When the perforation ratio is fixed, the air-frame interfacial area inside the perforated pores increases as the pore diameter is reduced. The improved air-frame interface area increases the acoustic resistance, enlarging the bandwidth in SAC and STL as a consequence. It also can be seen from Fig. 6-10 that decrease in pore diameter can enlarge the acoustical resonance frequencies and reduce the peak values in STL and SAC curves. As is known, the acoustical resonance frequency of micro perforated structures is dominated by their acoustic reactance. Since decreasing pore diameter can reduce the acoustic reactance, hence enlarges the acoustical resonance frequency[150,151].

Corrugated sandwich panels are ideally expected to have high peak values, big bandwidths and low acoustical resonance frequencies in SAC and STL curves at the same time. However, for sandwich panels with uniform pore diameters, the results of Fig. 6-10 reveal that there exists a contradiction among increment of bandwidth, decrease of acoustical resonance frequencies and increment of peak values. Therefore, panels with non-uniform pore diameters are resorted to balance this problem as shown in Fig. 6-11.

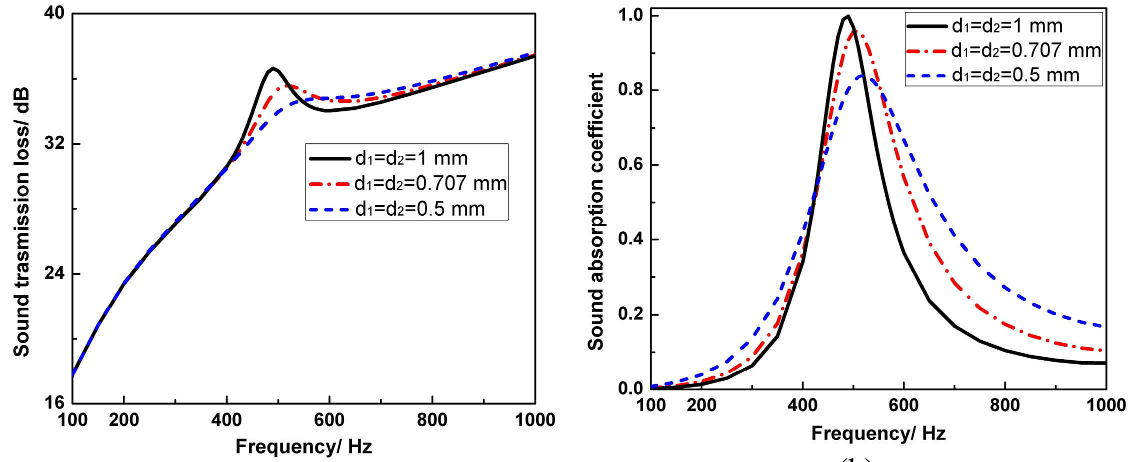

(a) (b)

Fig. 6-10 STL and SAC comparison among corrugated sandwich panels with uniform perforations but different pore diameters, (a) STL comparison, (b) SAC comparison

Figure 6-11 compares the STL and SAC of sandwich panels having both uniform and non-uniform perforations. For the two non-uniformly perforated sandwich panels, if the pores in the face plate have larger diameter than that in the corrugated cores, the pore diameters are defined as in descending order, otherwise they are defined as in ascending order. It can be seen from Fig. 6-11 that non-uniform pores can remedy the aforementioned deficiency induced by uniform pores. Compared with the uniformly perforated sandwich panels with pore diameter of 1 mm, the non-uniformly perforated panels have larger acoustic resistance induced by smaller pores in the face plates or corrugated cores, therefore, they exhibit wider bandwidth. On the other hand, the non-uniformly perforated panels have bigger pores in the face plates or corrugated cores than the uniformly perforated sandwich panels with pore diameter of 0.5 mm, which will enlarge the acoustic reactance of the panel, hence reduce the acoustical resonance frequency. In addition, the results of Fig. 6-11 also show that panels with non-uniform pores diameters in descending order have better STL and SAC at low frequencies than those in ascending order. For double layer coupled micro perforated structures, the coupling reaction between the two perforated layers is decided by the acoustic reactance of the layer farther from the sound source. Increase of the coupling reaction can result in bigger acoustical resonance frequency[151]. The coupling effect of the panel with pore diameters in ascending order is larger than that that with pore diameters in descending order due to the bigger pore diameter and acoustic reactance of the corrugated core. Therefore, the non-uniformly perforated panel with pores diameters in ascending order generates higher acoustical resonance frequency.

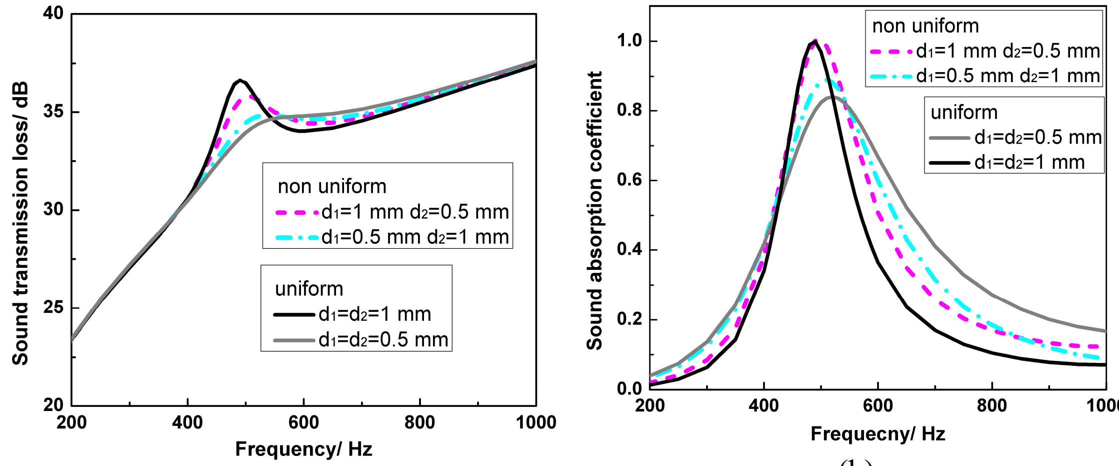

(a) (b)

Fig.6-11 STL and SAC comparison among corrugated sandwich panels with perforations of uniform pore diameters and those with non-uniform pore diameters, (a) STL comparison, (b) SAC comparison

6.4.3 Influence of perforation ratio

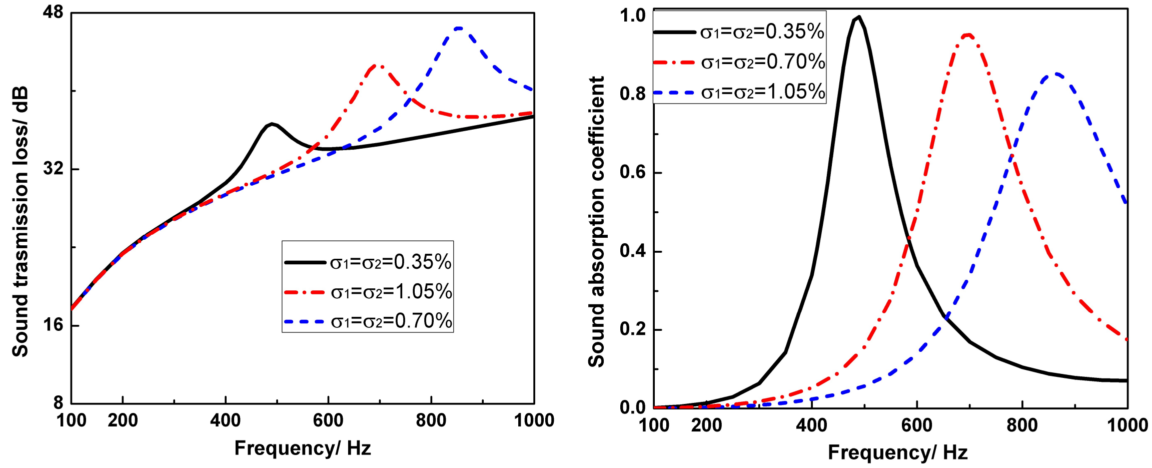

(a) (b)

Fig. 6-12 STL and SAC comparison among corrugated sandwich panels with perforations of different porosities, (a) STL comparison, (b) SAC comparison

This subsection discusses the influence of perforation ratio on the STL and SAC of corrugated sandwich panels. These perforated panels have the same geometrical parameters (as listed in Table 6-2) except perforation ratios. Notice that for the three sandwich panels discussed in Fig. 6-12, the perforation ratio in the face plate is identical to that in the corrugated core of the same sandwich panel. It can be seen from Fig. 6-12 that, for both STL and SAC, the bandwidth is enlarged as the perforation ratio is increased, which can also be attributed to the increasing acoustic resistance by increasing porosity. Besides, the acoustical resonance frequency decreases with decreasing perforation ratio owing to the enlarged acoustic reactance. Contradiction between the decrease of acoustical resonance frequency and the increase of bandwidth also exists for panels with uniform perforation ratios. Therefore, panels with non-uniform perforation ratio are explored in Fig. 6-13.

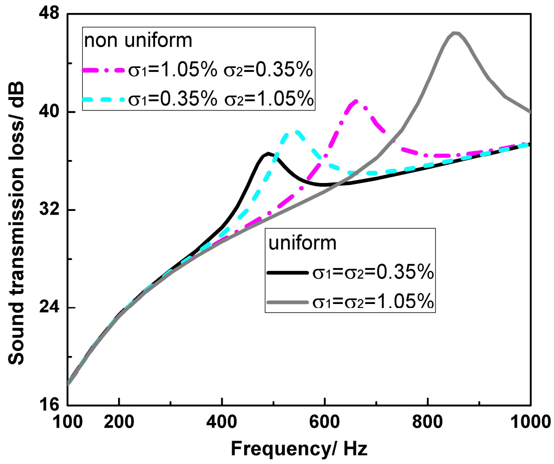

(a)

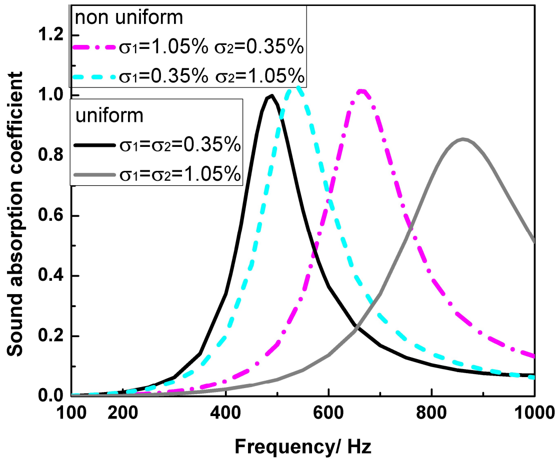

(b)

Fig. 6-13 STL and SAC comparison among corrugated sandwich panels with perforations of uniform and non-uniform porosities, (a) STL comparison, (b) SAC comparison

The STL and SAC of corrugated sandwich panels with non-uniform perforation ratios are compared with those with uniform perforation ratios in Fig. 6-13. The perforation ratios of the face plate and that of the core are in descending order and ascending order, respectively. Attributed to the enlargement of acoustic reactance induced by the smaller perforation ratio in the face plate or corrugated core, the panel with non-uniform perforation ratio is seen to have a lower acoustical resonance frequency than the uniformly perforated panel with a perforation ratio of 1.05%. On the other hand, the panel with non-uniform perforation ratio possess bigger acoustic resistance because of the bigger perforation ratio in the face plate or corrugated core than the uniformly perforated panel with a perforation ratio of 0.35%, which results in broader bandwidth. Besides, it also can be seen from Fig. 6-13 that sandwich panels with non-uniform perforation ratios in ascending order have better STL and SAC at low frequencies than that in descending order. As mentioned in section 6.4.2, the acoustical resonance frequencies of the two non-uniformly perforated panel are related to the acoustic reactance of the corrugated cores. The non-uniformly perforated panel with descending perforation ratios has corrugated core with larger acoustic reactance, therefore, exhibits higher acoustical resonance frequencies than the other panel.

6.5 Conclusions

In this study, corrugated sandwich panels with perforations are numerically investigated from the SAC and STL viewpoint. Finite element models are constructed by applying Comsol Multiphysics. The numerically calculated STLs are validated by comparing with experimental results, and excellent agreement is achieved. Subsequent comparisons between the classical corrugated sandwich panels (without perforations) and corrugated sandwich panels with face plate perforations prove the face plate perforations are effective in improving the SAC and STL at low frequencies. Meanwhile, the resonance frequencies and bandwidths in SAC and STL curves are shown to decrease with increasing pore diameter and decreasing perforation ratio. Panels with either non-uniform perforated pore diameters or non-uniform perforation ratios can have better low-frequency SAC and STL than those with uniform pore dimeters and perforation ratios. Results obtained in the present paper can help researchers to design superior multifunctional structures that aim at reducing both reflection and transmission with internal noise while maintaining high load-carrying capability. Further optimization work can be conducted based on corrugated sandwich panels with non-uniform perforations.

7 Low Frequency Sound Absorption Coefficient and Sound Transmission Loss of Perforated Honeycomb Sandwich Panels

7.1 Description of perforated honeycomb sandwich panels (PHSP)

Consider an ultra-lightweight sandwich panel with hexagonal honeycomb core shown schematically in Fig. 7-1. Its faceplates and core are both made of homogeneous and isotropic material. The top faceplate is a micro-perforated plate with submillimeter pores to enable sound penetration into the air cavities for absorption. It should be noted that in the structure, to achieve high structural efficiency, the thickness of either faceplate is much smaller than that of the middle layer (i.e., the core), while the wall thickness of the core is much smaller than its edge length. Except from the hexagonal honeycomb, other honeycombs, such as rectangular or triangular honeycombs shown in Fig. 7-2 can also act as the core of the sandwich. The sandwich panels with micro-perforated faceplates shown in Figs. 7-1 and 7-2 are attractive for multifunctional applications requiring lightweight and simultaneous load carrying, sound insulation as well as sound absorption capabilities.

To calculate the STL and SAC of perforated honeycomb sandwich panels, an analytical model is set up in the following section. Different from the existing models for normal honeycomb sandwich panels without perforation, this analytical model can not only calculate the pressure and velocity distributions inside honeycomb sandwich panels with perforated faceplates, but can also figure out the acoustic properties of perforated sandwich panels with rectangular and triangular cores as well as hexagonal ones.

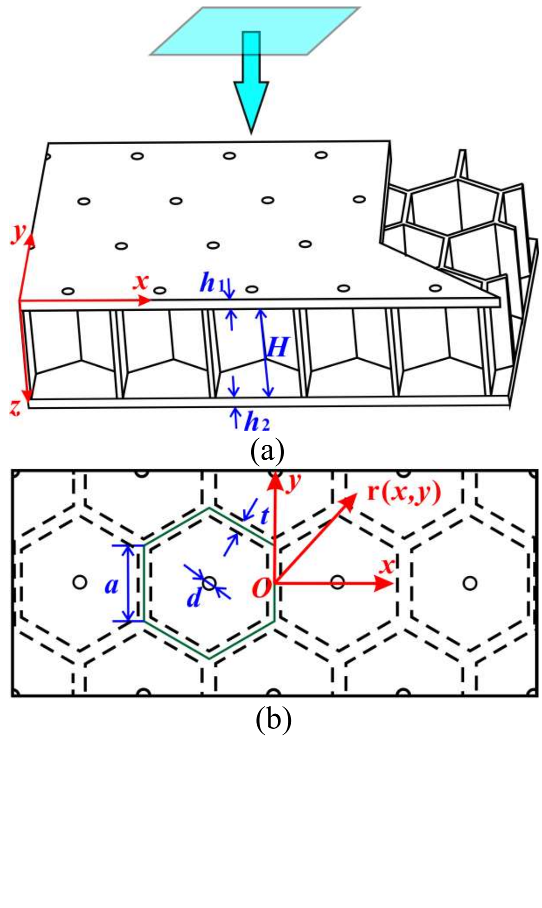

Fig. 7-1 Schematic of surface-perforated sandwich panel with hexagonal core: (a) global view and (b) top view

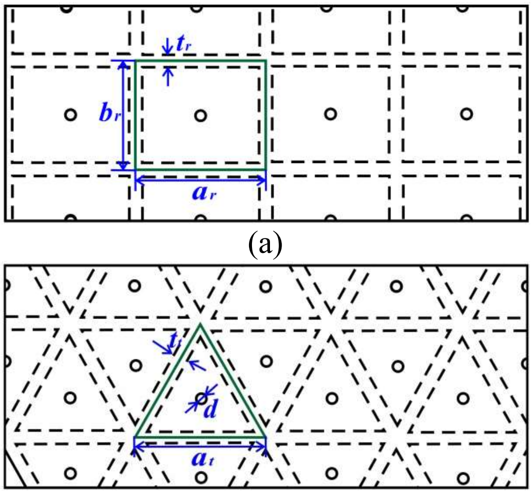

(a)

(b)

Fig. 7-2 Top view of sandwich panel with (a) rectangular core and (b) triangular core

7.2 Theoretical model for the sound propagation in PHSPs

For a normally incident sound wave, the incident sound pressure $p_i(\mathbf{r},z)$ and velocity $v_i(\mathbf{r},z)$ are given as:

$$p_i(\mathbf{r},z) = P_{i0}e^{-jk_0 z} \quad v_i(\mathbf{r},z) = P_{i0}e^{-jk_0 z}/\rho_0 c_0 \tag{7-1}$$

where P_{i0} is the amplitude of the incident wave. For simplification, the time factor $e^{j\omega t}$ is suppressed and $P_{i0}=1$ is set in the present paper.

In the field inside the honeycomb core between the faceplates, the sound pressure $p_2(\mathbf{r},z)$ can be given as [7]

$$p_2(\mathbf{r},z) = Ce^{-jk_0(z-h_1)} + De^{jk_0(z-h_1)} \tag{7-2}$$

where C and D are unknown parameters to be determined, and h_1 is the thickness of the micro-perforated faceplate. Accordingly, the velocity inside the honeycomb can be obtained as:

$$v_2(\mathbf{r},z) = \frac{-1}{j\omega\rho_0}\frac{\partial p_2(\mathbf{r},z)}{\partial z} = \frac{1}{\rho_0 c_0}\left(\mathrm{C}e^{-jk_0(z-h_1)} - De^{jk_0(z-h_1)}\right) \tag{7-3}$$

According to the Green's function, sound pressures on the surfaces of the faceplates in the incident and transmitted sound fields are separately given by[152]

$$p_1(\mathbf{r}) = 2p_i(\mathbf{r},0) - \frac{\rho_0\omega}{2}\int_{-\infty}^{\infty}\mathrm{H}_0^{(1)}\left(k_0\left|\mathbf{r}-\mathbf{r}_0\right|\right)v_1(\mathbf{r}_0)\,d\mathbf{r}_0 \tag{7-4}$$

$$p_3(\mathbf{r}) = \frac{\rho_0\omega}{2}\int_{-\infty}^{\infty}\mathrm{H}_0^{(1)}\left(k_0\left|\mathbf{r}-\mathbf{r}_0\right|\right)\mathrm{v}_3(\mathbf{r}_0)\,d\mathbf{r}_0 \tag{7-5}$$

where $\mathbf{H}_0^{(1)}$ is the first kind Hankel function of zero order. The velocity adjacent to the microperforated faceplate is given as [153,154]

$$v_1(\mathbf{r}) = v_2(\mathbf{r}, h_1) = (1-\sigma)v_p(\mathbf{r}) + \sigma v_f(\mathbf{r}) \tag{7-6}$$

where $v_p(\mathbf{r})$ is the velocity of the perforated faceplate, $v_f(\mathbf{r})$ is the velocity of the fluid inside the perforated pores, and σ is the perforation ratio of the plate. For a sandwich panel with hexagonal section core, the perforation ratio is calculated by:

$$\sigma = \pi d^2 / 6\sqrt{3}a^2 \tag{7-7}$$

where a is the edge length of the honeycomb, and d is the diameter of the perforated pores as shown in Fig. 7-1 (b). Likewise, for sandwich panels with rectangular and triangular honeycomb cores, the perforation ratios can be obtained by:

$$\sigma_r = \pi d^2 / 4a_r b_r \tag{7-8}$$

$$\sigma_t = \pi d^2 / \sqrt{3}a_t^2 \tag{7-9}$$

where a_r and b_r are the side length of the rectangular honeycomb, and a_t is the edge length of the triangular honeycomb as shown in Fig. 7-2. The pressure difference between the two surfaces of the perforated faceplate is related to the velocity and impedance, given as:

$$\Delta p(r) = Z_{resist}\left(v_f(\mathbf{r}) - v_p(\mathbf{r})\right) + Z_{react} v_f(\mathbf{r}) \tag{7-10}$$

where Z_{resist} and Z_{react} are the resistance and reactance of the perforated faceplate. According to Maa's theory, the resistance and reactance of a MPP are given as:

$$\begin{aligned} Z_{resist} &= \frac{32\eta h_1}{d^2}\left(\sqrt{1+\frac{X^2}{32}} + \frac{\sqrt{2}dX}{32h_1}\right) \\ Z_{react} &= -i\rho_0\omega h_1\left(1+\frac{1}{\sqrt{9+X^2/2}} + \frac{0.85d}{h_1}\right) \end{aligned} \tag{7-11}$$

where $X = d/2\sqrt{\rho_0\omega/\eta}$.

Upon combing Eq. (7-6) with Eq. (7-10), the velocity $v_1(\mathbf{r})$ can be given as:

$$v_1(\mathbf{r}) = -j\omega\lambda w_p(\mathbf{r}) + \zeta\left(p_1(\mathbf{r}) - p_2(\mathbf{r}, h_1)\right) \tag{7-12}$$

where $\lambda = 1-\sigma\left(Z_{react}/Z_0\right)$, $\zeta = \sigma/Z_0$ and $Z_0 = Z_{resist} + Z_{react}$.

Next, the fluid velocity adjacent to the lower face plate can be given as:

$$v_3(\mathbf{r}) = v_2(\mathbf{r}, h_1 + H) = -\mathrm{j}\omega w_b(\mathbf{r}) \tag{7-13}$$

Substitution of Eqs. (7-3) and (7-2) into Eqs. (7-12) and (7-13) leads to:

$$v_2(\mathbf{r}, h_1) = (\mathrm{C} - D)/\rho_0 c_0 = -j\omega\lambda w_p(\mathbf{r}) + \zeta\left(p_1(\mathbf{r}) - (\mathrm{C}+D)\right) \tag{7-14}$$

$$v_2(\mathbf{r}, h_1 + H) = \left(\mathrm{C}e^{jk_0\mathrm{H}} - De^{-jk_0 H}\right)/\rho_0 c_0 = -j\omega w_b(\mathbf{r}) \tag{7-15}$$

Combing Eqs. (7-14) and (7-15), one can express the unknown parameters C and D as:

$$
\begin{aligned}
D &= \rho_0 c_0 \left[\left(1+\zeta\rho_0 c_0\right) \mathrm{e}^{-jk_0 H} j\omega w_b(\mathbf{r}) - j\omega\lambda \mathrm{w}_p(\mathbf{r}) + \zeta p_1(\mathbf{r}) \right] \big/ Q \\
\mathrm{C} &= \rho_0 c_0 \left[-j\omega w_\mathrm{b}(\mathbf{r}) \mathrm{e}^{-jk_0 H} \left(-1+\zeta\rho_0 c_0\right) - j\omega\lambda \mathrm{w}_p(\mathbf{r}) \mathrm{e}^{-2jk_0 H} + \zeta p_1(\mathbf{r}) \mathrm{e}^{-2jk_0 H} \right] \big/ Q
\end{aligned}
\tag{7-16}
$$

Where $Q = \left(1+\zeta\rho_0 c_0\right)\mathrm{e}^{-2jk_0\mathrm{H}} - 1+\zeta\rho_0 c_0$.

For the case that the two faceplates are connected (bonded) by the honeycomb core, the core is considered as rigid, and the displacements of the faceplates are regarded as consistent[7], namely:

$$
w_p(\mathbf{r}) = w_b(\mathbf{r}) \tag{7-17}
$$

where the subscripts "*p*" and "*b*" denote the perforated faceplate and the bottom faceplate without perforation, respectively. The displacements of the two faceplates are governed by:

$$
\left(D_{p,b}\nabla^4 - m_{p,b}\omega^2\right) w(\mathbf{r}) = \Delta p_{p,b}(\mathbf{r}) \tag{7-18}
$$

where $m_{p,b}$ are the surface densities of the faceplates, $D_{p,b}$ denote flexible rigidities, and $\Delta p_{p,b}(\mathbf{r})$ are the pressure differences.

The total pressure acting on the two faceplates can be given as:

$$
\begin{aligned}
\Delta p_p(\mathbf{r}) &= p_1(\mathbf{r}) - p_2(\mathbf{r}, h_1) - I(\mathbf{r}) \\
\Delta p_\mathrm{b}(\mathbf{r}) &= p_2(\mathbf{r}, h_1 + H) - p_3(\mathbf{r}) + I(\mathbf{r})
\end{aligned}
\tag{7-19}
$$

where $I(\mathbf{r})$ is the force exerted by the honeycomb core.

Substituting Eq. (7-16) into Eq. (7-19) yields:

$$
\begin{aligned}
\Delta p_p(\mathbf{r}) &= \left(1-Q_3\right) p_1(\mathbf{r}) - Q_1 w_b(\mathbf{r}) - Q_2 w_p(\mathbf{r}) - I(\mathbf{r}) \\
\Delta p_b(\mathbf{r}) &= G_1 w_b(\mathbf{r}) + G_2 \mathrm{w}_p(\mathbf{r}) + G_3 p_1(\mathbf{r}) - p_3(\mathbf{r}) + I(\mathbf{r})
\end{aligned}
\tag{7-20}
$$

where

$$
\begin{aligned}
& Q_1 = 2\mathrm{e}^{-jk_0\mathrm{H}} j\omega\rho_0 c_0 / Q, Q_2 = \left[-j\omega\lambda(\mathrm{e}^{-2jk_0\mathrm{H}}+1)\rho_0 c_0\right] / Q, Q_3 = \zeta(\mathrm{e}^{-2jk_0 H}+1)\rho_0 c_0 / Q \\
& \mathrm{G}_1 = \left(1-\zeta\rho_0 c_0 + \left(1+\zeta\rho_0 c_0\right)\mathrm{e}^{-2jk_0 H}\right) j\omega\rho_0 c_0 / Q, G_2 = -2j\omega\lambda\rho_0 c_0 e^{-jk_0 H} / Q, G_3 = 2\zeta e^{-jk_0 H} \rho_0 c_0 / Q
\end{aligned}
\tag{7-21}
$$

Assuming $u_{p,b}(\mathbf{r})$ are the displacements of the two faceplates when they are excited by an unit force $\delta(\mathbf{r})$, one has:

$$
\left(D_{p,b}\nabla^4 - m_{p,b}\omega^2\right) u_{p,b}(\mathbf{r}) = \delta(\mathbf{r}) \tag{7-22}
$$

According to the definition of the convolution integral, the displacements of the faceplates can be expressed as:

$$
w_{p,b}(\mathbf{r}) = \int_{-\infty}^{\infty} \Delta p_{p,b}(\mathbf{f}) \times u_{p,b}(\mathbf{r}-\mathbf{f})\, d\mathbf{f} \tag{7-23}
$$

Substituting Eqs. (7-20) and (7-21) into Eq. (7-23), one can write these displacements as:

$$
\begin{aligned}
w_p(\mathbf{r}) &= \int_{-\infty}^{\infty} \left(\left(1-Q_3\right) p_1(\boldsymbol{\xi}) - Q_1 w_b(\boldsymbol{\xi}) - Q_2 w_p(\boldsymbol{\xi}) - I(\boldsymbol{\xi})\right) \times u_p(\mathbf{r}-\boldsymbol{\xi})\, d\boldsymbol{\xi} \\
w_b(\mathbf{r}) &= \int_{-\infty}^{\infty} \left(\mathrm{G}_1 w_b(\boldsymbol{\xi}) + G_2 w_p(\boldsymbol{\xi}) + G_3 p_1(\boldsymbol{\xi}) - p_3(\boldsymbol{\xi}) + I(\boldsymbol{\xi})\right) \times u_b(\mathbf{r}-\boldsymbol{\xi})\, d\boldsymbol{\xi}
\end{aligned}
\tag{7-24}
$$

The force of the honeycomb can be obtained by introducing the Fourier transform to Eq. (7-24) as well as by combing with the convolution theorem,

$$\begin{aligned} W_p(\mathbf{k}) &= 2\pi\left((1-Q_3)P_1(\mathbf{k})-Q_1W_b(\mathbf{k})-Q_2\mathrm{W}_p(\mathbf{k})-I_p(\mathbf{k})\right)U_p(\mathbf{k}) \\ W_{\mathrm{b}}(\mathbf{k}) &= 2\pi\left(G_1\mathrm{W}_b(\mathbf{k})+G_2\mathrm{W}_p(\mathbf{k})+G_3P_1(\mathbf{k})-P_3(\mathbf{k})+I_p(\mathbf{k})\right)U_b(\mathbf{k}) \end{aligned} \tag{7-25}$$

where $\mathbf{k}=(k_x,k_y)$ and $U_{p,b}(\mathbf{k})=1\big/2\pi\left(\mathrm{D}_{p,b}|\mathbf{k}|^4-m_{p,b}\omega^2\right)$. $W_{p,b}(\mathbf{k})$, $P_1(\mathbf{k})$, $I_p(\mathbf{k})$ and $U_p(\mathbf{k})$ are the Fourier transforms of $w_{p,b}(\mathbf{r})$, $p_1(\mathbf{r})$, $I(\mathbf{r})$ and $u_{p,b}(\mathbf{r})$, which can be obtained by:

$$\begin{aligned} F(\mathbf{k}) &= \frac{1}{2\pi}\int_{-\infty}^{\infty} f(\mathbf{r})e^{-\mathrm{j}\mathbf{kr}}d\mathbf{r} \\ f(\mathbf{r}) &= \int_{-\infty}^{\infty} F(\mathbf{k})e^{j\mathbf{kr}}d\mathbf{k} \end{aligned} \tag{7-26}$$

Substitution of Eq. (7-12) into Eq. (7-4) yields:

$$p_1(\mathbf{r})=2p_i(\mathbf{r},0)-\frac{\rho_0\omega}{2}\int_{-\infty}^{\infty}\mathrm{H}_0^{(1)}\left(k_0|\mathbf{r}-\mathbf{r}_0|\right)\left(-j\omega\lambda w_p(\mathbf{r})+\zeta\left(p_1(\mathbf{r})-p_2(\mathbf{r},h_1)\right)\right)d\mathbf{r}_0 \tag{7-27}$$

Since the function $\mathrm{H}_0^{(1)}\left(k_0|\mathbf{r}-\mathbf{r}_0|\right)$ is given as:

$$\mathrm{H}_0^{(1)}\left(k_0|\mathbf{r}-\mathbf{r}_0|\right)=\frac{1}{\pi}\int_{-\infty}^{\infty}\frac{e^{\mathrm{j}\mathbf{k}(\mathbf{r}-\mathbf{r}_0)}}{\sqrt{k_0^2-|\mathbf{k}|^2}}d\mathbf{k} \tag{7-28}$$

Eq. (7-27) can be rewritten after the Fourier transform, as:

$$P_1(\mathbf{k})=\frac{2}{Q_p}\delta(\mathbf{k})-\frac{Q_w}{Q_p}W_b(\mathbf{k}) \tag{7-29}$$

where $Q_p=\left(1+\rho_0\omega\zeta(\mathrm{e}^{-2jk_0\mathrm{H}}-1)\big/Q\sqrt{k_0^2-|\mathbf{k}|^2}\right)$, $Q_w=\rho_0\omega\left(-2\zeta\rho_0c_0\mathrm{e}^{-jk_0\mathrm{H}}j\omega-j\omega\lambda(\mathrm{e}^{-2jk_0H}-1)\right)\big/Q\sqrt{k_0^2-|\mathbf{k}|^2}$.

Similarly, by applying Fourier transform to Eq.(7-5), one arrives at:

$$P_3(\mathbf{k})=Q_{p3}W_b(\mathbf{k}) \tag{7-30}$$

where $Q_{p3}=-j\rho_0\omega^2\big/\sqrt{k_0^2-|\mathbf{k}|^2}$.

Substituting Eqs. (7-29) and (7-30) into Eq. (7-25), one obtains the displacement as:

$$W_{\mathrm{b}}(\mathbf{k})=F_b(\mathbf{k})\delta(\mathbf{k}) \tag{7-31}$$

where $F_b(\mathbf{k})=2(G_3-Q_3+1)/Q_pQ_{\mathrm{L}}$, $Q_{\mathrm{L}}=Q_{wm}+(G_3-Q_3+1)Q_w/Q_p+Q_{p3}$ and $Q_{wm}=(D_p+D_b)|\mathbf{k}|^4-\Gamma\omega^2+j\omega\rho_0c_0/Q\left[-\left(1-e^{-jk_0H}\right)^2(1+\lambda)+\zeta\rho_0c_0\left(1-e^{-2jk_0H}\right)\right]$, Γ is the sum of surface densities of the two face plates, given as $\Gamma=m_p+m_b$.

Given that the two faceplates are connected by the honeycomb core, the mass of the honeycomb should be reflected in the model. The total surface density Γ is thus modified by adding the surface density of the honeycomb core m_c,

$$\Gamma^c=\Gamma+m_{\mathrm{c}} \tag{7-32}$$

where the surface densities of the honeycomb cores are calculated by

$$m_c=\frac{M}{S}=\begin{cases}\left(1.5\sqrt{3}a^2-1.5\sqrt{3}\left(a-t/\sqrt{3}\right)^2\right)H\rho_c\Big/1.5\sqrt{3}a^2 & \text{Hexgonal core}\\ \left(a_rb_r-\left(a_r-t_r\right)\left(b_r-t_r\right)\right)H\rho_c\Big/a_rb_r & \text{Rectangular core}\\ \left(a_t^2-\left(a_t-\sqrt{3}t_t\right)^2\right)H\rho_c\Big/a_t^2 & \text{Triangualr core}\end{cases} \tag{7-33}$$

where M and S are the unit cell mass and cross section area of the honeycomb cores respectively, ρ_c is the density of the honeycomb cores.

Substitution of Eq. (7-31) into Eq. (7-26) yields the displacement of the bottom facelate:

$$w_b\left(\mathbf{r}\right)=\frac{2\left(G_3-Q_3+1\right)}{Q_{b1}+Q_{b2}+Q_{b2}} \tag{7-34}$$

where Q_{b1}, Q_{b2} and Q_{b3} are:

$$\begin{aligned}&Q_{b1}=\left(1+\rho_0\omega\zeta(\mathrm{e}^{-2jk_0\mathrm{H}}-1)/Qk_0\right)\left(-\Gamma^c\omega^2+j\omega\rho_0c_0/Q\left[-\left(1-e^{-jk_0H}\right)^2\left(1+\lambda\right)+\zeta\rho_0c_0\left(1-e^{-2jk_0H}\right)\right]\right)\\&Q_{b2}=\left(G_3-Q_3+1\right)\left(-G_3\rho_0c_0j\omega+Q_2+2\rho_0c_0j\omega\lambda/Q\right)\\&Q_{b3}=-j\rho_0c_0\omega\left(G_1/j\omega\rho_0c_0+Q_3-2/Q\right)\end{aligned} \tag{7-35}$$

Similarly, Substitution of Eq. (7-29) into Eq. (7-26) leads to the pressure on the surface of the top faceplate:

$$p_1\left(\mathbf{r}\right)=\frac{2j\omega\rho_0c_0Q}{QG_1+j\omega\rho_0c_0QQ_3-2j\omega\rho_0c_0}\left(1-\frac{\left(G_3-Q_3+1\right)Q_m}{Q\left(Q_{b1}+Q_{b2}+Q_{b2}\right)}\right) \tag{7-36}$$

where $Q_m=-G_3\rho_0c_0j\omega Q+Q_2Q+2\rho_0c_0j\omega\lambda$.

Combing Eqs. (7-6)(7-14)(7-16)(7-17)(7-34) and (7-36) yields

$$v_1\left(\mathbf{r}\right)=\left(Q_{v1}/Q\right)w_b\left(\mathbf{r}\right)+\left(Q_{v2}/Q\right)p_1\left(\mathbf{r}\right) \tag{7-37}$$

where $Q_{v2}=\zeta(\mathrm{e}^{-2jk_0h}-1)$ and $Q_{v1}=-2\zeta\rho_0c_0\mathrm{e}^{-jk_0h}j\omega-j\omega\lambda(\mathrm{e}^{-2jk_0h}-1)$.

According to Eq.(7-34), the sound pressure and velocity in the transmitted sound field are:

$$\begin{aligned}p_3\left(\mathbf{r}\right)&=-i\rho_0c_0\omega w_b\left(\mathbf{r}\right)\\v_3\left(\mathbf{r}\right)&=-i\omega w_b\left(\mathbf{r}\right)\end{aligned} \tag{7-38}$$

Finally, the STL and SAC of the honeycomb sandwich with perforated faceplate can be obtained by comparing the transmitted and reflected sound energy with the incident energy, as:

$$\mathrm{STL}=20\log_{10}\frac{E}{E_{trans}}\qquad \mathrm{SAC}=1-\frac{E_{ref}}{E}-\frac{E_{trans}}{E} \tag{7-39}$$

here, E, E_{trans} and I_{ref} are the total incident energy, the transmitted energy and the reflected energy, respectively, which can be calculated as:

$$
\begin{aligned}
&E = 0.5\,\mathrm{Re}\int_S p_i(\mathbf{r})\cdot v_i^*(\mathbf{r})dS \\
&E_{trans} = 0.5\,\mathrm{Re}\int_S \left\{p_3(\mathbf{r})\cdot v_3^*(\mathbf{r})\right\}dS \\
&E_{ref} = 0.5\,\mathrm{Re}\int_S \left\{\left(p_1(\mathbf{r}) - p_i(\mathbf{r})\right)\cdot\left(-v_1(\mathbf{r}) + v_i(\mathbf{r})\right)^*\right\}dS
\end{aligned}
\tag{7-40}
$$

7.3 Validation of the theoretical model

The proposed theory in the last section should be validated because of the simplifications and assumptions made to develop the model. To this end, a FE model is established based on the commercial software COMSOL Multiphysics. The calculation unit cells of sandwich panels with perforated facing are shown in Fig. 7-3 for hexagonal core, rectangular core and triangular core. The shapes of these unit cells are all rectangular, so that periodic boundary conditions can be added to the boundary of each unit cell. The calculation model of hexagonal sandwich panel is shown in Fig. 7-4, where two perfectly matched layers are added to the ends of incident and transmitted sound fields to mimic open and non-reflecting infinite sound fields. The solid mechanics modulus of COMSOL is applied to calculate the displacement and velocity of the solid part of each sandwich panel, with the sandwich regarded as an isotropic elastic material. For air inside the perforated pore, the thicknesses of viscous and thermal boundary layers have the same order of magnitude as the pore radius in the considered frequency range. Therefore, the thermoacoustic modulus is applied to calculate the sound pressure and temperature variation of the air, with both viscous and thermal losses included. With air in the incident, transmitted and inside the core considered as non-viscous, the pressure acoustic modulus is applied to calculate the pressure and air velocity. At solid-fluid interface, the velocity of air is equal to that of solid, and temperature variation is adiabatic at the interface.

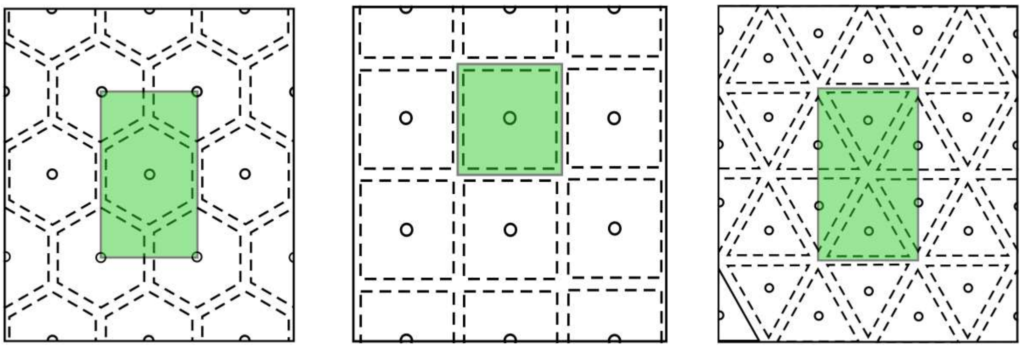

(a) hexagonal core (b) rectangular core (c) triangular core

Fig. 7-3 Unit cells of honeycomb sandwich panels with perforated faceplates for FE

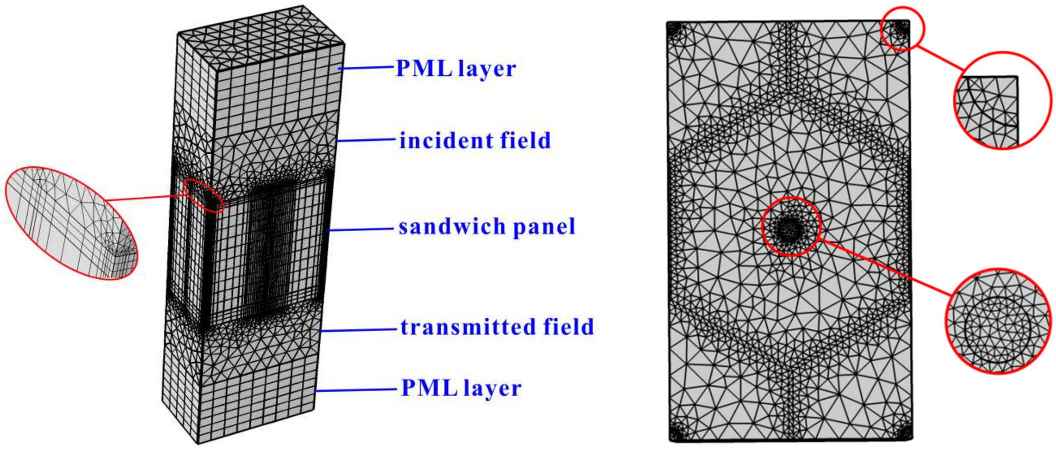

(a) Mesh of global view Top view

Fig. 7-4 FE mesh of perforated hexagonal honeycomb sandwich panel

The FE simulation results of PHSPs are compared with theoretical model predictions in Fig. 7-5 from the viewpoint of STL and SAC, respectively. All the samples are assumed to be made of aluminum with density of 2700 kg/m^3, Poisson's ratio of 0.35, and elastic modulus of 70 GPa. The geometrical parameters of the samples are listed in Table 7-1. The simulated results for sandwich panels with hexagonal, rectangular and triangular cores all agree well with theoretical predictions.

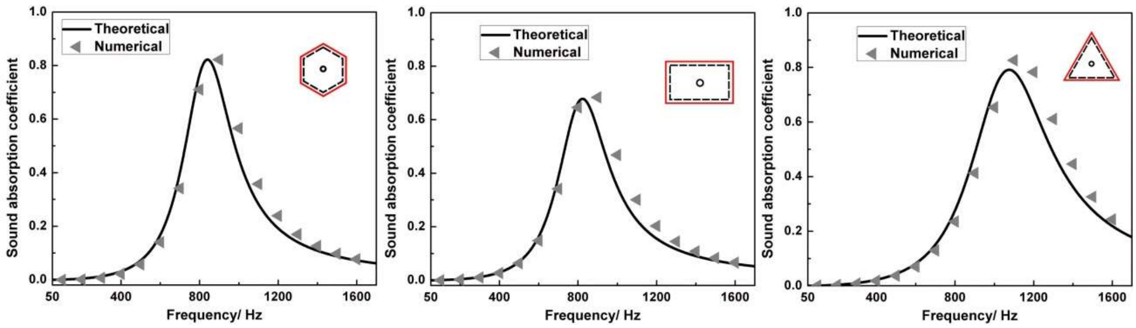

(b)

Fig. 7-5 Comparison of STL (a) and SAC (b) between theory and FE simulation for sandwich panel with various honeycomb cores

Table 7-1. Geometrical parameters of perforated honeycomb sandwich panels for FE simulation

Hexagonal core
$h_1 = 1$ mm, $h_1 = 2$ mm, $H = 17$ mm, $a = 6.2$ mm,
$t = 0.2$ mm, $d = 1$ mm, $\sigma = 0.79\%$
Rectangular core
$h_1 = 1$ mm, $h_1 = 1$ mm, $H = 20$ mm, $a_r = 12$ mm,
$b_r = 10$ mm, $t = 0.3$ mm, $d = 1.2$ mm, $\sigma = 0.94\%$
Triangular core
$h_1 = 1$ mm, $h_1 = 2$ mm, $H = 17$ mm, $a_t = 10$ mm,

$t = 0.2$ mm, $d = 0.8$ mm, $\sigma = 1.16\%$

Except from the simulation results by FE models, the present theory is also validated by comparison with the available experimental results in literature by Toyoda and Takahashi[7]. The tested sample was composed of a 0.5-mm-thick acryl MPP, a 60-mm-thick paper honeycomb and a 1-mm-thick non perforated acryl plate. The acryl plate has a density of 1190 $\mathrm{kg/m^3}$, elastic modulus of 2.8 GPa, Poisson's ratio of 0.3. The paper honeycomb has a density of $24\,\mathrm{kg/m^3}$. The STL predicted by the present theory is compared with the experimental and theoretical results by Toyoda and Takahashi[7] in Fig. 7-6. It can be seen that the STL by the present theory matches with the experimental and theoretical results by Toyoda and Takahashi. Discrepancies may be attributed to the non-ideal experimental conditions, dimension errors and defects inside the sample.

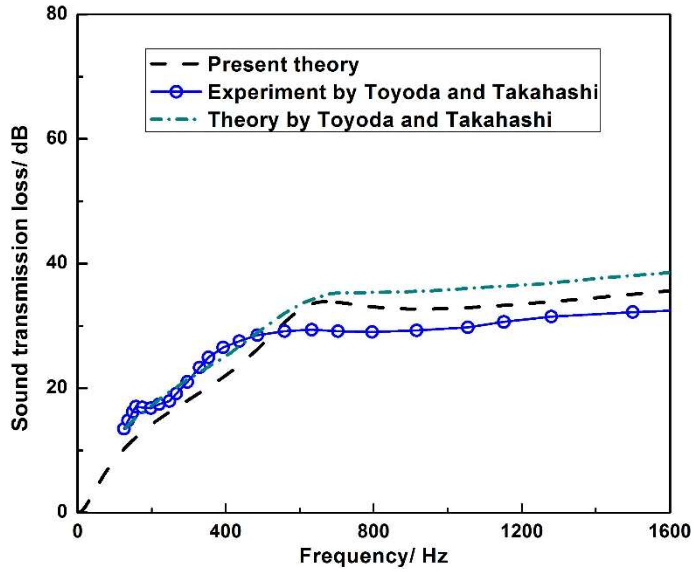

Fig. 7-6 Comparison of STL between the present model and experimental and theoretical results by Toyoda and Takahashi[7]

In addition, since the PHSP can be favorably degraded to non-perforated classic honeycomb sandwich panel by setting the perforation ratio and perforated pore diameter to negligibly small, the present theory is also verified by Kumar *et al.*'s[155] model for classical honeycomb sandwich panels as shown in Fig. 7-7. Kumar *et al.* calculated the STL of classical honeycomb sandwich panels by orthotropic panel theory. The geometrical parameters of the non-perforated hexagonal honeycomb sandwich panel in Fig. 7-7 are the same as that listed in Table 7-1 except from the perforation ratio and pore diameter. It can be seen from Fig. 7-7 that STL by the present theory agrees well with that by Kumar *et al.*'s model.

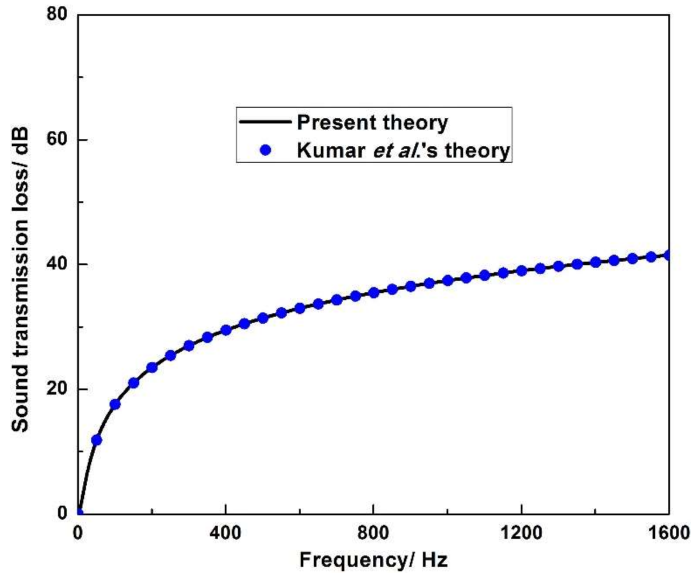

Fig. 7-7 Comparison of STL between the present model and theoretical results by Kumar *et al.*[155]

7.4 Parameter study

To figure out the effects of perforated faceplate and explore the influential parameters related to the perforation, systematic parameter studies based on the validated analytical model are performed from the viewpoint of STL and SAC. For further validation of the model, corresponding results obtained using FE models are also presented below.

7.4.1 Effect of perforated faceplate

The STL and SAC of hexagonal sandwich panels with perforated faceplates are compared with those of hexagonal sandwich panel without perforation in Fig. 7-8. Geometrical parameters of the sandwich are the same as those listed in Table 7-1.

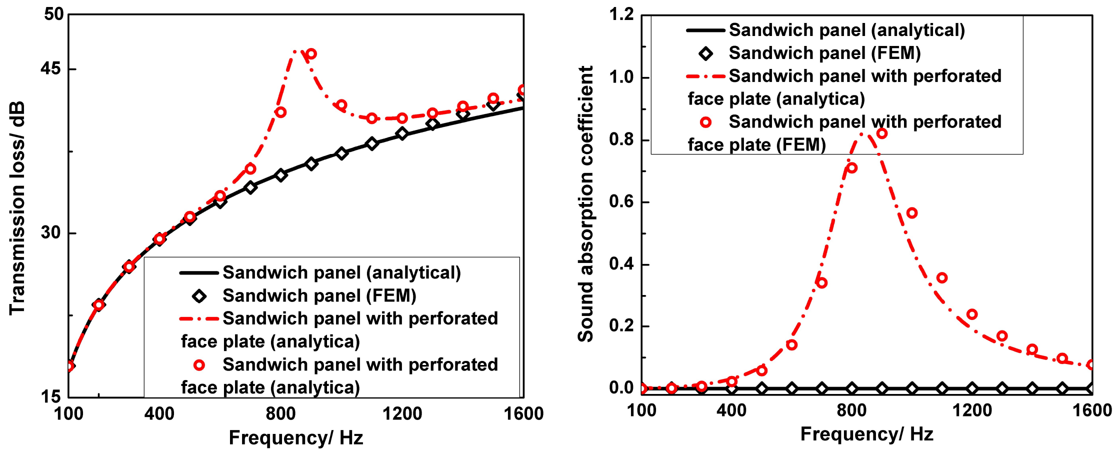

(a) (b)

Fig. 7-8 Comparison of sound transmission loss and absorption coefficient between sandwich panels with non-perforated and perforated faceplates

It can be seen from Fig. 7-8(b) that, in the absence of perforation, the SAC is zero for all frequencies as expected. That is, traditional honeycomb sandwiches without perforated facings cannot absorb sound at all. In sharp contrast, for sandwiches with perforated faceplates, an absorption crest appears in the SAC versus frequency curve, because the perforated faceplate, the honeycomb core and the backing faceplate constitute distributed Helmholtz resonators. The resonance frequency of the distributed 'Helmholtz resonators' can be estimated as[156]

$$f_0 = \frac{c_0}{2\pi}\sqrt{\sigma / H\left(h_1 + \delta_{tot}\right)} \approx 860\text{Hz} \tag{7-41}$$

where $\delta_{tot} \approx 8d/3\pi$ is the end correction. The results of Fig. 7-8 (b) demonstrate that the peak frequency in the SAC curve as predicted by the present analytical model is approximately equal to the resonance frequency estimated by Eq. (7-41).

Figure 7-8 (a) shows perforation-induced increment of STL within the frequency range of 700~1200 Hz. The peak frequency in the STL curve is identical to that in the SAC curve, which means that the enlargement of STL should be attributed to the appearance of SAC. For the sandwich without perforation, since no acoustic energy can be consumed during sound propagation, the STL is decided by the reflection of sound wave. In the presence of perforation, sound wave enters the sandwich via the perforated pores and the acoustic energy is consumed due to viscous and thermal losses inside the pores.

7.4.2 Influence of perforation ratio

Figure 7-9 shows three hexagonal sandwich panels having identical geometrical parameters but different perforation ratios. These sandwich panels have one, two and three pores in each unit cell of the faceplate as shown in Figs. 7-9. All the pores have the same diameter of 0.5 mm, and the other geometrical parameters of the sandwich panels are the identical to those of Table 7-1. Accordingly, the perforation ratios are 0.39%, 0.79% and 1.2%, respectively.

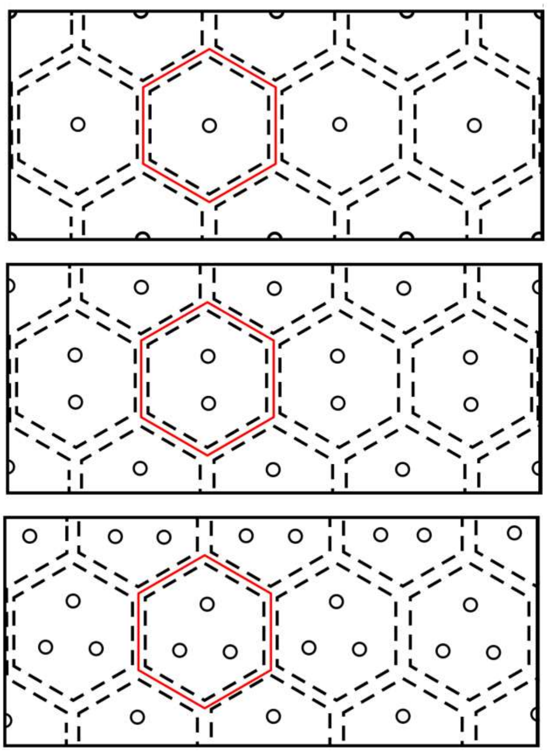

Fig. 7-9 Schematic of hexagonal sandwich panels with different perforation ratios

The influence of perforation ratio on the STL and SAC of hexagonal sandwich panels is displayed in Fig. 7-10. It can be seen from Fig. 7-10 that with the increase of perforation ratio, the peak frequency of the STL and SAC increases, which can also be seen evidently from Eq. (41). Besides, the bandwidth for SAC is enlarged by the increase of perforation ratio. As the perforation ratio is increased, the viscous and thermal losses inside the perforated pores are enhanced as a result of the increased contact area between air and solid frame, thus enlarging the resistance of the perforated faceplate. The enlarged resistance will increase the bandwidth[150].

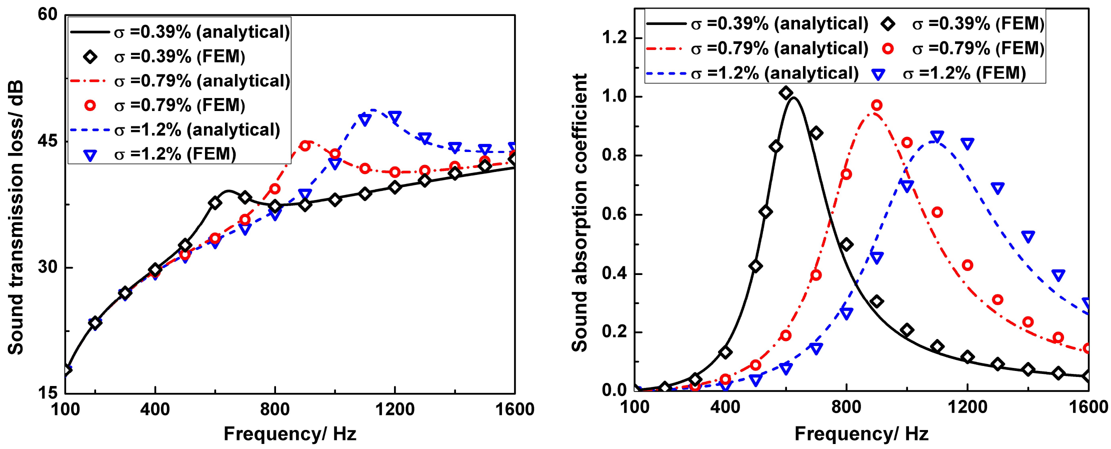

(a) (b)

Fig. 7-10 Influence of perforation ratio on sound transmission loss and absorption coefficient of hexagonal sandwich panel

7.4.3 Influence of pore diameter

Figure 7-11 shows three hexagonal sandwich panels having the same geometrical parameters except the pore diameter and number. These sandwich panels have one, two and four pores in each unit cell of the top faceplate. With identical perforation ratio assumed, the corresponding pore diameters are 1 mm, 0.707 mm and 0.5 mm. The remaining parameters are the same as those listed in Table 7-1.

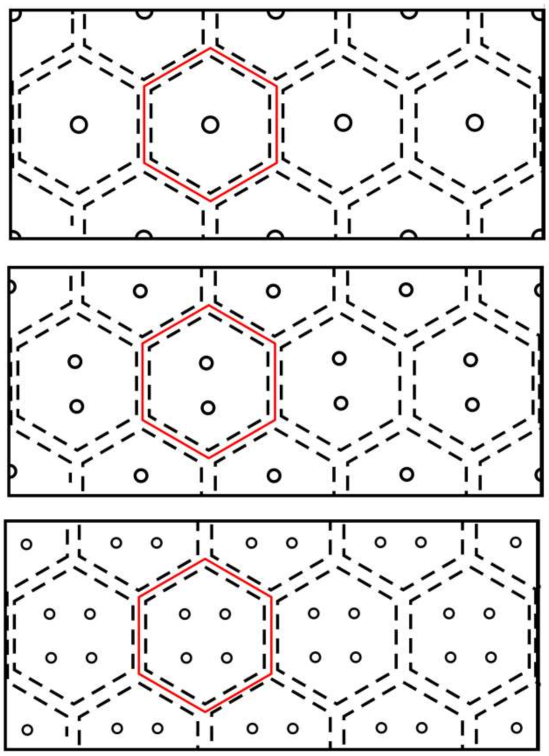

Fig. 7-11 Schematic of hexagonal sandwich panels with different pore diameters but fixed perforation ratio

Figure 7-12 compares the STL and SAC of the three sandwich panels. It is seen from Fig. 7-12 that the peak frequency is improved by reducing the pore diameter. According to Eq.(7-41), the peak frequency of SAC increases with decreasing pore diameter and, accordingly, the peak frequency of STL increases. Besides, with the decrease of pore diameter, the bandwidth of SAC is enlarged. Decreasing the pore diameter increases the contact area between air and solid frame inside the pores, which in turn leads to enlarged resistance of the perforated faceplate.

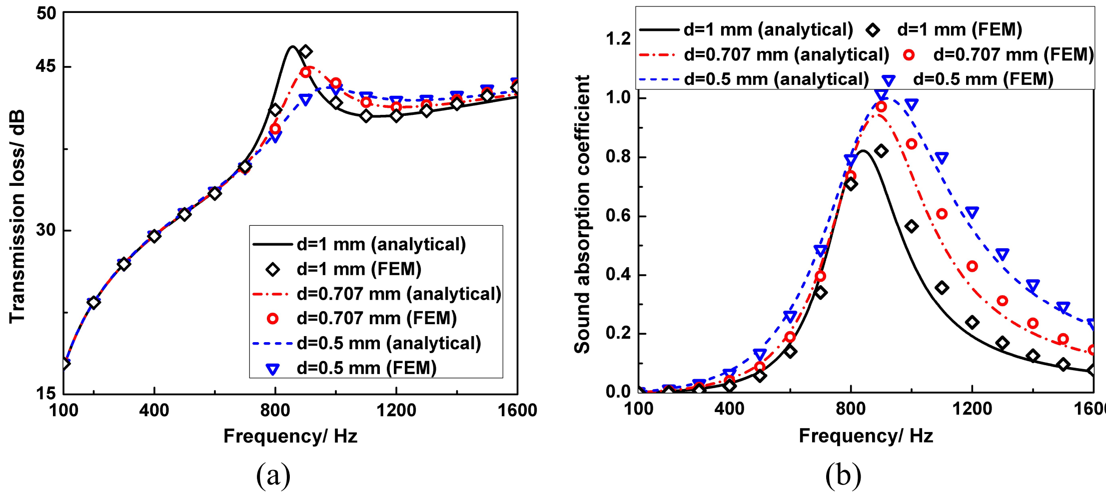

Fig. 7-12 Influence of pore diameter on sound transmission loss and absorption coefficient of hexagonal sandwich panels with fixed perforation ratio

7.4.4 Influence of core configuration

According to the theory presented in Section 7.2, the surface density and perforation ratio of a honeycomb sandwich panel are affected by core configuration. Consequently, the STL and SAC of the sandwich are also affected, as discussed below.

Let sandwich panels with different honeycomb cores have the same geometrical parameters and the same effective mass. When the geometrical parameters of hexagonal sandwich panel are the same as shown in Table 7-1, the side lengths of rectangular and triangular cores can be calculated using Eq. (7-33). Table 7-2 presents the side length and perforation ratio for each type of sandwich panel. For simplification, the length of the rectangular core is set as $a_s = b_s$.

Table 7-2. Side lengths of honeycomb cores and perforation ratios of sandwich panels with these cores

Core shape	Side length (mm)	Perforation ratio
Hexagon	6.2	0.79 %
Square	10.75	0.68 %
Triangular	18.61157	0.52 %

The STL and SAC of the three sandwich panels are compared in Fig. 7-13. It is seen that the peak frequency increases as the edge number of the core is increased, and sandwich panel with triangular core has the best acoustic properties at relatively low frequencies.

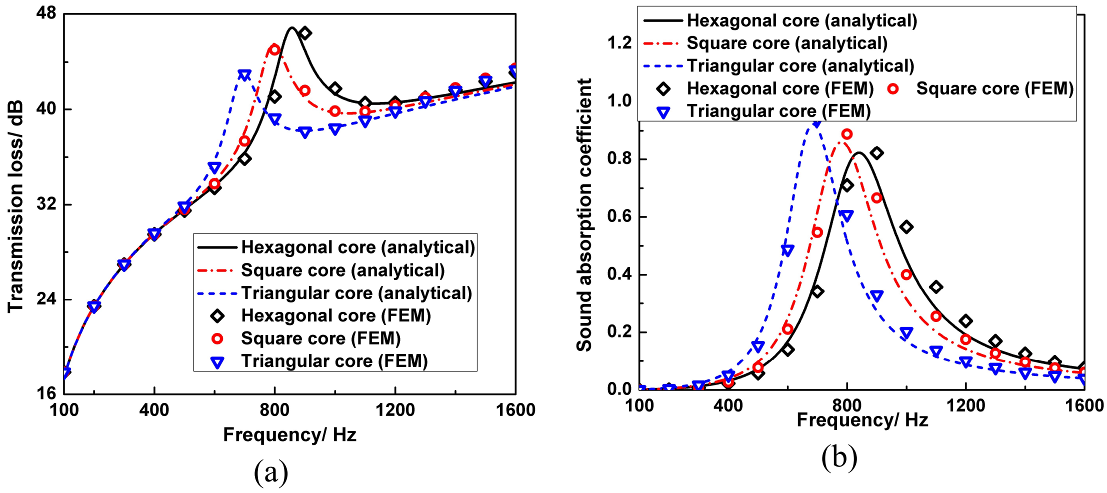

Fig. 7-13 Influence of core configuration on sound transmission loss and absorption coefficient of honeycomb sandwich panels having identical effective mass

7.5 Conclusion

An analytical model for estimating the STL and SAC of honeycomb sandwich panels with perforated faceplates is developed by taking into account the effect of faceplate perforation as well as the effect of core configuration. The reflected and transmitted sound pressures are expressed by applying the Green's function and solved by employing Fourier transforms. The STL and SAC are obtained by comparing the reflected and transmitted sound energy with the incident sound energy. FE models are developed to validate the analytical model, with good agreement achieved. In the analytical model, the two face plates are assumed to have the same displacement because of the honeycomb connection, which makes the presented model valid for frequencies lower than faceplate resonance frequency. Acoustic properties of frequencies higher than the faceplate resonance frequency go beyond our investigation in the present model. Influences of faceplate perforation, perforation ratio, pore size, and core configuration are discussed using the analytical model. Results show that perforation in faceplate can improve the STL and SAC at low frequencies, and the peak frequency in the STL and SAC curves increases with increasing perforation ratio and decreasing pore size. Compared with other sandwich panels of the same effective mass and perforated pores, the sandwich panel with triangular core exhibits the lowest peak frequency for both STL and SAC. Results of the present chapter can inspire researchers to design multifunctional lightweight sandwich structures with superior mechanical and acoustic properties by artificially adding perforations to existing sandwich panels or optimizing the sandwich core.

8 Low Frequency Sound Absorption Coefficient and Sound Transmission Loss of Perforated Sandwich Panels with Porous Materials

8.1 Introduction of perforated sandwich panel with porous materials

The perforated sandwich panels are proved to improve the SAC and STL of the sandwich panel by the sound wave resonances, but the bandwidth of the increment is subjected to the resonance frequencies and is relatively small at low frequencies as discussed in Chapters 6 and 7. Improvement of bandwidth is in demand for better application.

Simultaneously, porous materials are good sound absorbers that provide broadband sound absorption. Different from the perforated panels, the sound energy is dissipated by the thermal and viscous effects during the propagation inside the porous materials.

Therefore, porous materials are filled into the cores of perforated sandwich panels in this chapter. The combination of two different energy consumption methods might improve the bandwidth of the perforated sandwich panels. Besides, the effects of different porous materials filling ways on the acoustic properties of perforated sandwich panels are also explored with explanation provided.

8.2 Acoustic properties of PCSPs with porous materials

8.2.1 PCSPs with different filling ways of porous materials

When porous material is added to the PCSPs, porous materials can be filled with three different ways: fully filled inside the sandwich panel, filled in the upper part or lower part inside the sandwich panel divided by the corrugated pores. The schematics of the PCSPs with different porous material configurations are shown in Fig. 8-1.

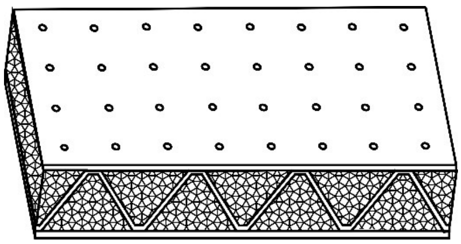

(a)

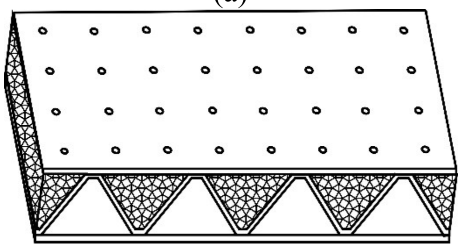

(b)

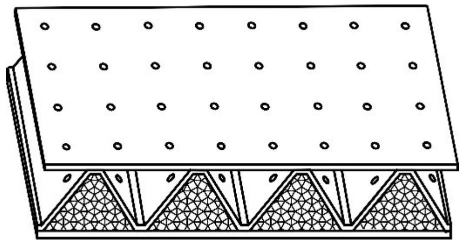

(c)

Fig. 8-1 Schematics of the PCSPs with porous materials (a) PCSP with fully filled porous material (PCSP-FP), (b) PCSP with up-half part filled porous material (PCSP-UP), (c) PCSP with low-half part filled porous material (PCSP-LP)

8.2.2 FE models for PCSPs with rigid frame porous materials

The PCSPs with different rigid frame porous materials configurations are also modelled by the same FE method used in Chapters 6 and 7. The fluid part inside the perforated pores are calculated by the Thermoacoustic Module of Comsol with the governing equation shown as Eq. (6-3), while the solid part is modeled by the linear elastic solid module controlled by Eq.(6-2). The Poroacoustics module is applied with regard to the modelling of rigid porous material inside the corrugations. The governing equation is similar to Eq. (6-1) except the sound speed replaced by the complex sound speed inside the rigid frame porous materials, given as

$$c = \sqrt{\frac{K_{eff}}{\rho_{eff}}} \tag{8-1}$$

where ρ_{eff} represents the dynamic density, K_{eff} is the dynamic bulk modulus. The dynamic density and bulk modulus are determined by above mentioned general JCA (Johnson-Champoux-Allard) model, given as

$$\begin{aligned} \rho_{eff} &= \frac{\tau_\infty \rho_0}{\Omega}\left[1 + \frac{R_f \Omega}{i\omega\rho_0\tau_\infty}\sqrt{1 + \frac{4i\omega\tau_\infty^2\eta\rho_0}{R_f^2 L_V^2 \Omega^2}}\right] \\ K_{eff} &= \frac{\gamma P_0/\Omega}{\gamma - (\gamma - 1)\left(1 + \frac{8\eta}{i\omega L_{th}^2 P_r \rho_0}\sqrt{1 + \frac{i\omega L_{th}^2 P_r \rho_0}{16\eta}}\right)^{-1}} \end{aligned} \tag{8-2}$$

where τ_∞ is the tortuosity, R_f is the static flow resistivity, Ω is the porosity of the porous materials, L_V and L_{th} denote the viscous and thermal characteristic lengths respectively.

8.2.3 Influence of porous material configurations on PCSPs

Figure 8-2 compares the STL and SAC of the four PCSPs with different porous material configurations. The acoustic properties of the filled porous materials with the same thickness of the PCSPs are also presented for comparison. The geometrical and physical parameters of the PCSP and filled porous materials are listed in Table 8-1 and Table 8-2 respectively.

Table 8-1 Geometrical parameters of the PCSPs

Parameters	Value
face plates thicknesses	$h_1 = h_2 = 1$ mm
thickness of the corrugated core	$H = 18$ mm
perforation ratios	σ_1=σ_2=0.785%
pores diameters	$d_1 = d_2 = 1.5$ mm
Wall thickness of corrugated core	$t = 1$ mm
inclination angle of the core	φ=54.8°
unit cell width of the core	$L = 30$ mm

Table 8-2 Physical parameters of the porous materials

Parameters	Value
porosity	$\Omega = 97\%$
flow resistivity	$R_f = 30000\ \mathrm{Pa \cdot s / m^2}$
viscous characteristic length	$L_v = 41\ \mu\mathrm{m}$
thermal characteristic length	$L_{th} = 59\ \mu\mathrm{m}$
tortuosity	τ_∞=1.06

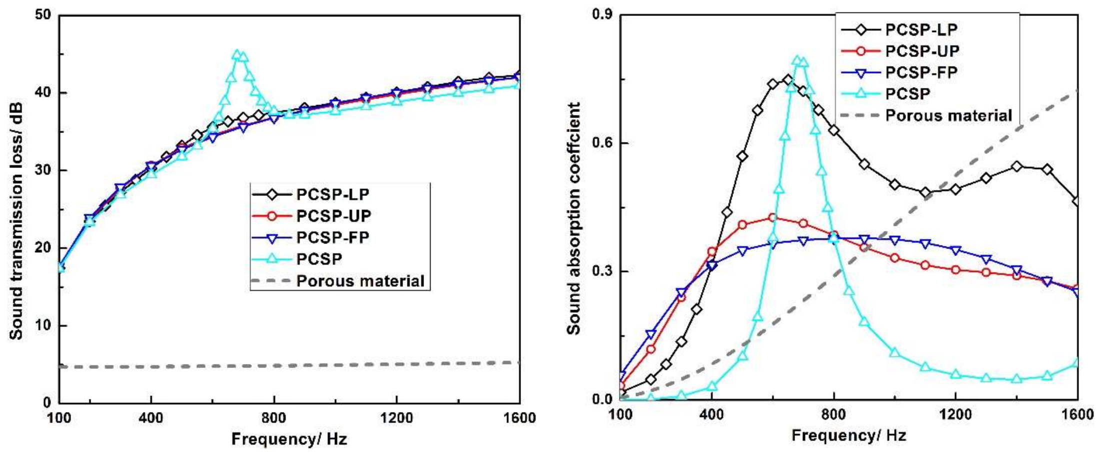

(a) (b)

Fig. 8-2 Comparison between the PCSPs with and without porous materials

It can be seen from Fig. 8-2 (b) that, compared with the PCSP without porous materials, the PCSPs with porous materials have a SAC with larger bandwidth and lower acoustical resonance frequencies. The two acoustical resonance frequencies become closer due to the filled porous materials, the bandwidths in SAC curves is hence enlarged because of the two adjacent acoustic resonance frequencies.

Besides, since the sound energy can be dissipated inside the porous materials, the resonances caused by the standing waves are weakened accordingly. The peak values of STL and SAC of PCSP with porous materials are smaller than that of PCSP without porous materials as shown in Figs.8-2 (a) and (b).

In addition, Figs. 8-2 (a) and (b) shows that the PCSP-LP has both highest values and broadest bandwidth in the SAC and STL curves of the three PCSPs with porous materials. To further compare the three PSCPs with porous materials and explain the differences in the SAC and STL curves, the surface impedances of the three structures are also plotted as Fig. 8-3.

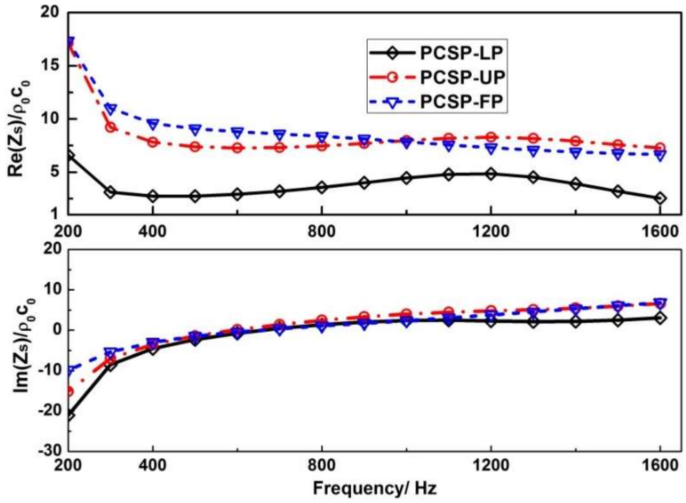

Fig. 8-3 Comparison of the surface impedances of the three PCSPs with different porous material configurations

As shown in Fig.8-3, imaginary parts of surface impedances of the three structures have approximate values, while the real part of the surface impedance of PCSP-LP is much closer to the air impedance $\rho_0 c_0$ than that of PCSP-LP and PCSP-UP at frequencies higher than 400 Hz. Therefore, the PSCP-LP has better impedance match with air than the other two structures. However, for frequencies lower than 400 Hz, the imaginary part of impedance of PSCP-LP has bigger absolute value, which brings larger acoustic reactance, sound absorption coefficient is reduced accordingly.

Except from the surface impedances, the power dissipation densities inside the three PCSPs with porous materials are also plotted in Fig. 8-4, which will further reveal the mechanism underlying the PCSPs with different porous materials configurations.

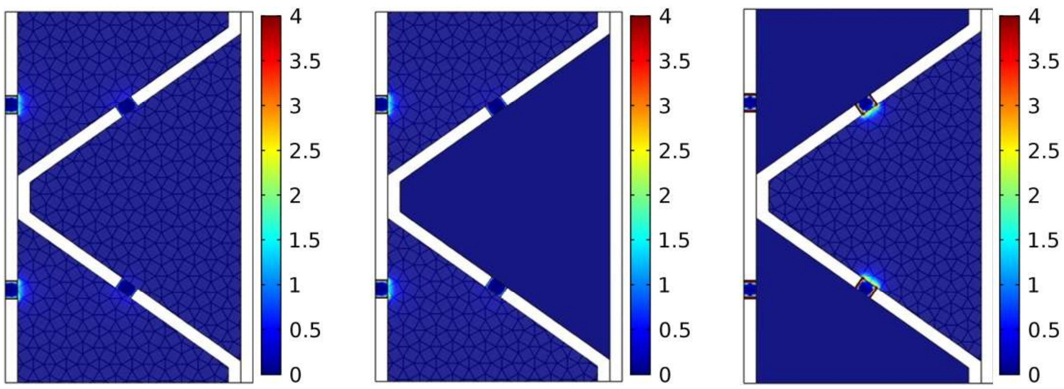

(a) (b) (c)

Fig.8-4 Power dissipation density (W/m^3) at 450 Hz in the (a) PCSP-FP, (b) PCSP-UP, (c) PCSP-LP

It can be seen from Fig. 8-4 that sound energy is dissipated fiercely by the low-part filled porous materials and both the perforations in the face plate and corrugated cores for the PCSP-LP. On the contrary, sound energy is mostly consumed by the perforated pores in the face plate and up-half filled porous material with regard to PCSP-FP and PCSP-UP, much less energy dissipation happens around the perforated pores in the corrugation and low-half filled porous materials. The porous materials filled in the up half part of the corrugated cores produces high resistance which keep back the sound propagation through the perforated corrugation and low-half filled porous materials. The SACs of PCSP-UP and PCSP-FP are smaller than that of PCSP-LP as a result.

8.2.4 Parameter study

In the section, the FE models are employed to investigate the influences of geometrical parameters of PCSPs (perforation ratio and perforated pore diameters particularly) on the acoustic properties of the PCSPs with porous materials. Besides, since the sound absorbing ability of the porous material is greatly affected by the physical parameters (flow resistivity and porosity particularly), influences of these parameters are also discussed. It is demonstrated that the PCSP-LP has the best STL and SAC of all the PCSPs with porous materials in the previous section, therefore, only the PCSP-LP is considered in this section. Moreover, it is noted that the STL is much less affected by the porous materials and perforations than SAC based on the above results, the emphasis is hence on the change of SAC with the considered parameters. Further fundamental understandings for the sound propagations through the PCSP-LP are also provided by the parameter study.

1) Influences of perforation ratio

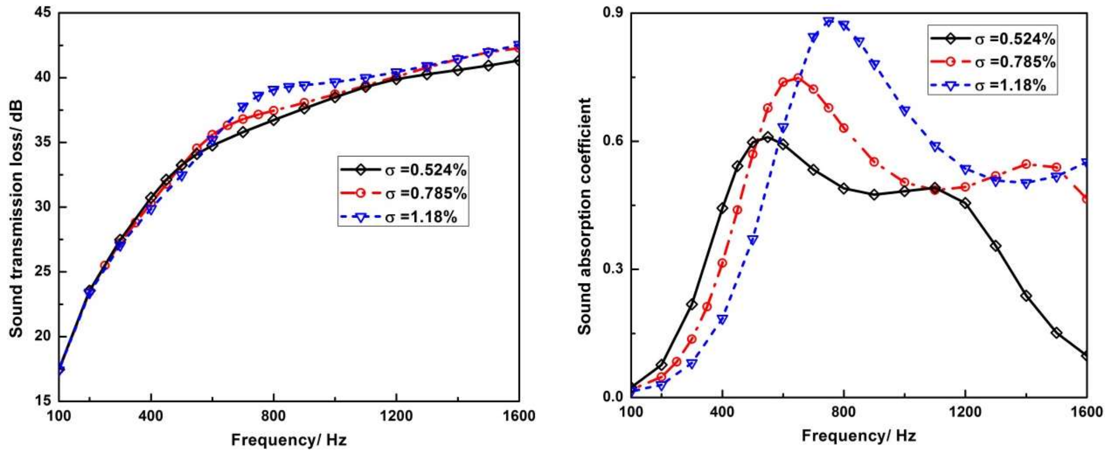

(a) (b)

Fig. 8-5 Comparison among PCSP-LPs with different perforation ratios: (a) STL, (b) SAC

Influences of the perforation ratio on the acoustic properties of the PCSP-LP are discussed in this subsection as shown in Fig. 8-5 (a) and (b). The PCSP-LPs have the same geometrical parameters and porous materials as listed in Table 8-1 and Table 8-2 except from the perforation ratio. It can be seen from Fig. 8-5 (b) that the resonance frequencies shifts to lower frequencies with the decrease of perforation ratio, corresponding to that of PCSP. With the decrease of perforation ratio, the reactance of the PCSP-LP increases, which will reduce the resonance frequencies. Besides, the decrease of perforation ratio narrows the gap between the two resonance frequencies owing to the reduced resistivity, hence enlarge the bandwidth of SAC. The change of STL with perforation ratio is correspondence to that of SAC.

2) Influences of perforated pore diameters

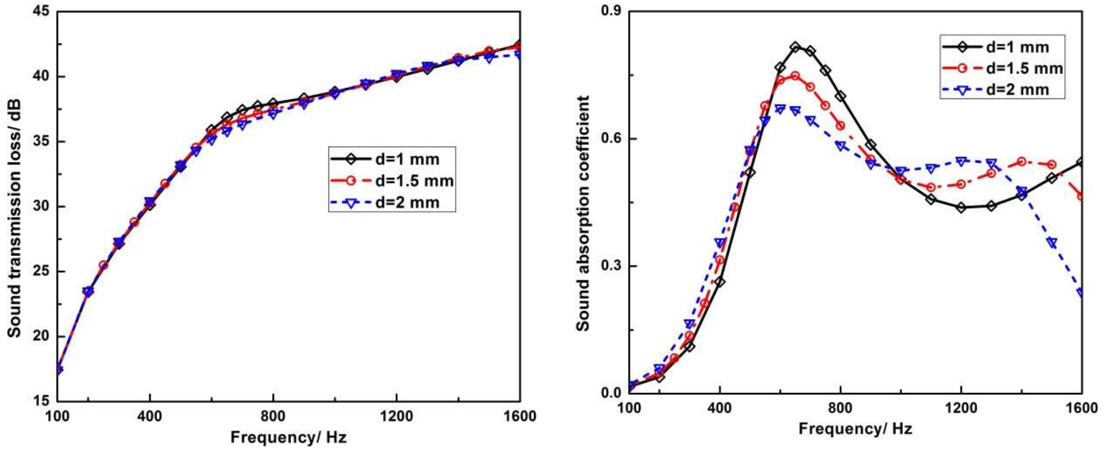

Fig. 8-6 Comparison among PCSP-LPs with different perforation pore diameters: (a) STL, (b) SAC

Figure 8-6 (a) and (b) plot the STL and SAC of three PCSP-LPs with the same parameters except from the perforated pore diameters. Identifying with that discussed in Chapters 6 and 7, the resonance frequencies decrease with the increase of the pore diameter due to the enlarged reactance. In addition, the increase of pore diameter can decrease the acoustic resistance of the structure as mentioned in Chapter 6, which makes two acoustical resonance frequencies closer. SAC with broad bandwidth can be generated with the two adjacent resonance frequencies.

3) Influences of filled porous materials

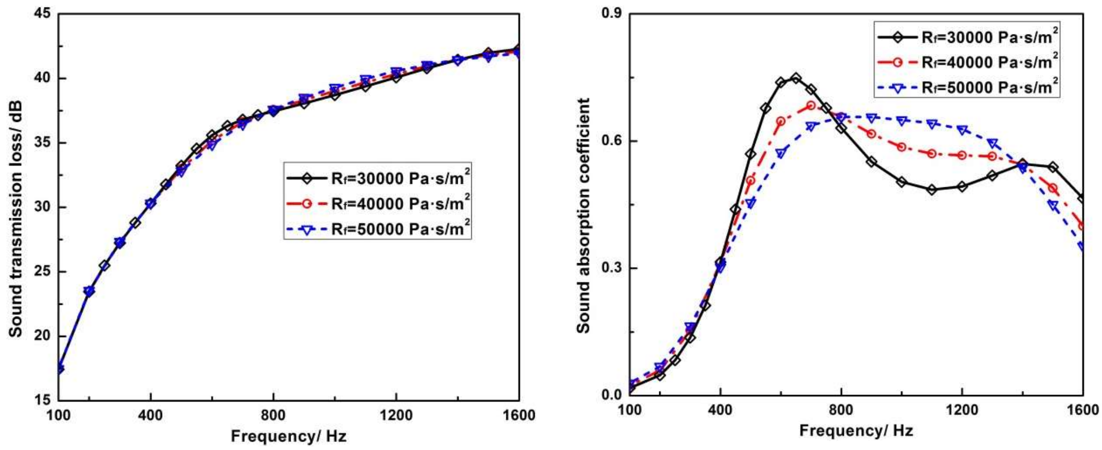

Fig. 8-7 Comparison among PCSP-LPs with different flow resistivities (a) STL, (b) SAC

Figure 8-7 (a) and (b) plot the STL and SAC of three PCSP-LPs with the same PCSPs but flow resistivity varied porous materials. The filled porous materials have the same physical parameters (as listed in Table 8-2) except the flow resistivity. It can be seen from Fig. 8-7 (b) that, the resonance frequencies decreases with the decrease of flow resistivity, while peak value of SAC increases with the decrease of flow resistivity. As is known, the enlarged flow resistivity leads to better sound absorbing ability for porous materials, the sound absorbing bandwidth can be improved accordingly. However, the increase of flow resistivity will also prevent the sound propagation inside the porous materials, the acoustical resonance frequencies are thus enlarged and peak value of SAC reduced. The STL of PCSP-LP hardly changes with flow resistivity of the porous materials as shown in Fig. 8-7 (a).

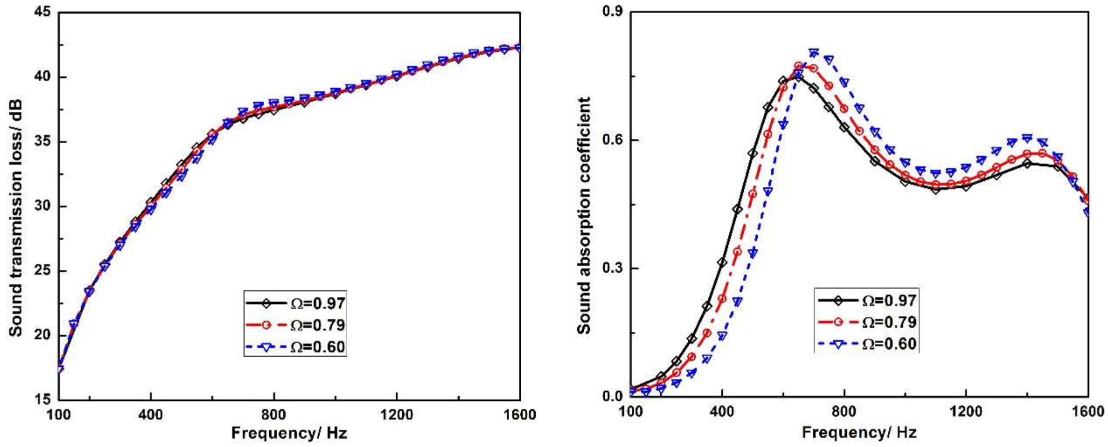

(a) (b)

Fig. 8-8 Comparison among PCSP-LPs with different porosities (a) STL, (b) SAC

Figures 8-8 (a) and (b) compare the STL and SAC of the PCSP-LPs with porosity varied porous materials. The physical parameters of the porous materials are listed in Table 8-2 except from the porosity. It can be seen from Fig. 8-8 (b) that with the decrease of porous material porosity, the bandwidth of SAC is reduced. The sound absorbing ability of the porous materials becomes smaller with the decrease of porosity, the PCSP-LP exhibits lower resistance accordingly. The bandwidth of SAC hence becomes smaller. Beside, since the reduced porosity makes the sound wave propagate harder in the porous materials, the resonance frequency is enlarged as shown in Fig. 8-8 (b). It is also found from Fig. 8-8 (a) that the porosity variation brings tiny change to the STL of PCSP-LPs.

8.3 Acoustic properties of PHSPs with porous materials

Except from the PCSPs, the PHSPs with porous materials (PHSP-Ps) is also considered in the present section as shown in Fig. 8-9. Only the PHSPs with square honeycomb cores are calculated for simplicity. The STL and SAC of the PHSP-Ps are also estimated numerically by the FE method discussed in the last section.

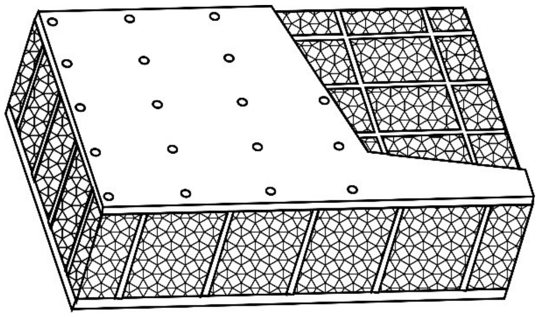

Fig. 8-9 Schematic of PHSP with porous materials

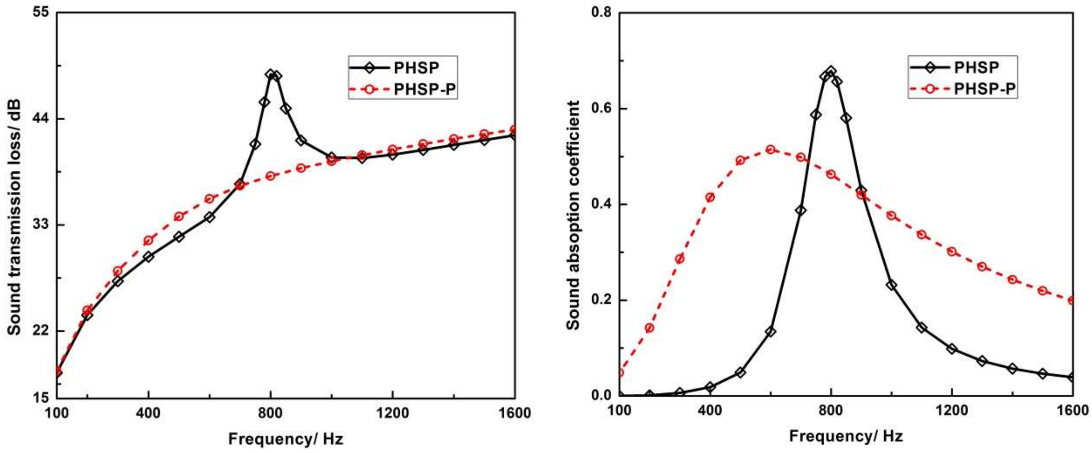

Fig. 8-10 Comparison between PHSPs with and without porous materials

Figure 8-10 plots the comparison of STL and SAC between PHSP and PHSP-P. The geometrical parameters of the calculated PHSPs and filled porous materials are listed in Table 8-3. It can be seen from Fig. 8-10 that bandwidth of SAC can be greatly improved by the porous materials in the PHSPs. Identical with that discussed in the last section, the energy dissipation inside the porous materials can weaken the sound wave resonance, the peak values of resonance in SAC and STL curves hence decrease. Besides, the bandwidth of SAC is also improved by the energy dissipation of porous materials.

Table 8-3. Geometrical parameters of PHSP

Parameters	Value
face plates thicknesses	$h_1 = h_2 = 1$ mm
thickkess of honeycomb core	$H = 18$ mm
perforation ratios	σ=0.785%
pores diameters	$d_1 = d_2 = 1.5$ mm
Wall thickness of honeycomb core	$t = 0.688$ mm
unit cell of the core	$a_r = b_r = 15$ mm

8.4 Comparison between PCSPs and PHSPs with and without porous materials

Both the PCSP and PHSP are proved to provide more effective STL and SAC at low frequencies than conventional sandwich panels. It might be meaningful to compare the acoustic properties of the two structures, which will give instructions for practical applications.

On the basis of the previous FE model method, the STL and SAC of the two structures are calculated and compared in the present section. Since the PHSPs with different honeycomb cores have the same STL and SAC mechanisms, only the PHSP with rectangular honeycomb cores are considered for simplicity. The PCSP and PHSP without porous materials are first compared in Fig. 8-11, following with the comparison between PCSP-P and PHSP-P in Fig. 8-12.

Assume the PCSP and PHSP have the same thickness, faceplates and effective density. The perforated pore diameter and perforated ration in the faceplates of both the structures are also identical. The geometrical parameters of the PCSP are listed in Table 8-1, so the parameters of the PHSP can be obtained as the same as that listed in Table 8-3.

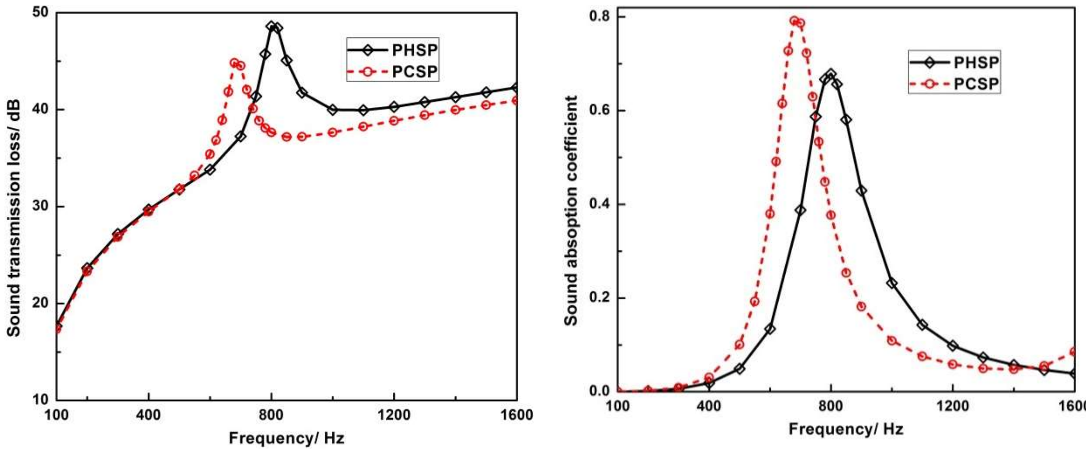

Fig. 8-11 Comparison between PCSP and PHSP (a) STL, (b) SAC

As shown in Fig. 8-11, the resonance frequency in the STL and SAC curves of PCSP is lower than that in the curves of PHSP. Compared with the PHSP, the PCSP has perforations in both the corrugated cores and perforated faceplate. The perforated pores in the faceplate and corrugated are regarded as parallelly connected. The parallel connection of perforated pores can improve the acoustic resistance and reduce the resonance frequency[84].

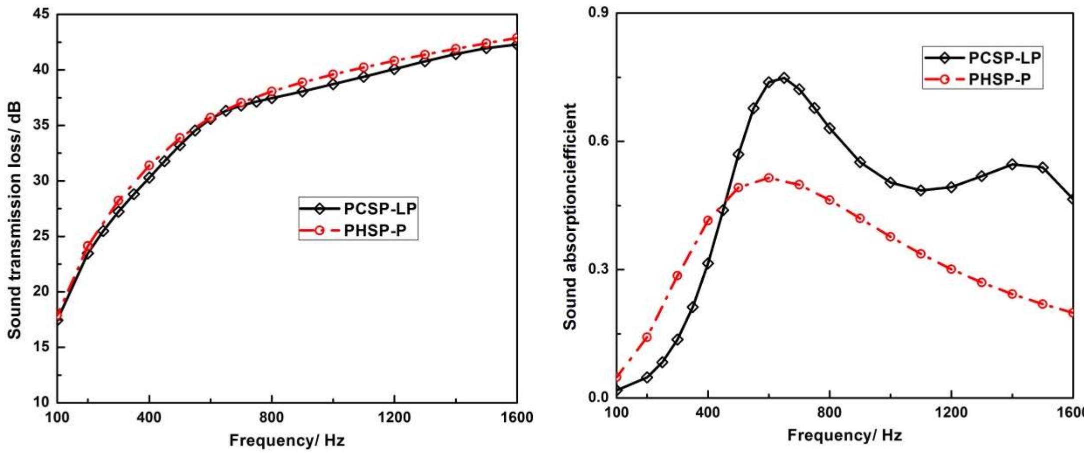

(a) (b)

Fig. 8-12 Comparison between PCSP and PHSP (a) STL, (b) SAC

Figure 8-12 compare the STL and SAC of the PCSP-LP with that of PHSP-P. The physical parameters of the filled porous material are the same as that listed in Table 8-2. It can be seen from Fig. 8-12 (b) that the PCSP-LP has better SAC that PHSP-P with higher value and wider bandwidth in the considered frequency range. Simultaneously, Fig. 8-12 (b) also shows the resonance frequency of the PHSP-P is lower than that of PCSP-LP, which is contrary to the comparison between PCSP and PHSP without porous materials. The PHSP-P hence posses higher SAC at low frequencies (<500 Hz) that PCSP-LP. As discussed in previous sections, the porous materials can lower the resonance frequencies of PCSP and PHSP, and the resonance frequency reduction of PHSP is clearly bigger than that of PCSP.

8.5 Conclusions

Perforated sandwich panels with rigid frame porous materials are developed on the basis of PCSPs and PHSPs to provide STL and SAC with wider bandwidth. The FE method for the modeling of PCSPs and PHSPs are applied to estimate the acoustic properties of perforated sandwich panels with porous materials. The filled porous materials inside the perforated sandwich panels are modeled based on JCA model. The perforated sandwich panels with porous materials can not only provide SAC with wider bandwidth than perforated sandwich panels without porous materials, the resonance frequency is also reduced due to the attenuation of porous materials. However, since the sound wave resonance is weakened by the energy consumption of the porous materials, the peak values in the STL and SAC curves of PCSP and PHSP by the resonance decreases. Besides, for the PCSPs with porous materials, highest SAC can be obtained when the porous materials are filled only to the low half part of the corrugated cores. The up half filled porous materials enlarges the acoustic resistance of the whole structure, which keeps back the sound propagation inside the composite structures. Whereafter, comparisons are made between PCSPs and PHSPs with and without porous materials. The PCSP has higher resonance frequency and larger SAC at low frequencies in contrast to PHSP, while this trend is reversed for the PCSP-LP and PHSP-P by the resonance reduction effect of the porous materials. The presented perforated sandwich panels with porous materials are more applicable as sound absorbing materials at low frequencies than perforated sandwich panels with the broad bandwidth.

9 Conclusions and Future Work

The findings of the present dissertation are summarized and the future work is suggested in this chapter.

This dissertation focuses on acoustic materials for sound absorption and transmission loss. Porous materials with better sound absorption are developed and optimized by methods of physical parameter gradient and surface roughness. Combinations of microperforated structures and sandwich panels are proposed to achieve both good sound absorption and transmission loss. Porous materials are further added to the cores of combinations to enlarge the sound absorption bandwidth. These findings provide a foundation for future work.

9.1 Conclusions and Findings

The conclusions and findings of the present dissertation are listed as below

A combined theoretical and experimental study is carried out to investigate the anisotropic acoustic properties of sintered fibrous metals. The anisotropic sound absorption coefficient of the sintered fibrous material are modeled based on randomly placed parallel fibers. For validation, experimental measurements are performed, with good agreement achieved. Subsequent numerical investigations show that sintered fibrous material shows better sound absorption/attenuation performance in direction parallel to its surface than in direction normal to its surface. The anisotropy in acoustical properties increases with decreasing fiber diameter and porosity due mainly to increasing interactions between adjacent fibers.

Optimization of the graded sintered fibrous materials is conducted based on the above mentioned theory. Distributions of the porosity and fiber diameter are optimized for either a sole frequency or a pre-specified frequency range using genetic algorithm method. The optimized graded sintered fibrous materials have the best sound absorption compared with other non-optimized sintered fibrous materials.

Built upon the acoustic impedance of circular apertures and cylindrical cavities as well as the principle of electroacoustic analogy, an impedance model is developed to calculate theoretically the sound absorption of graded semi-open cellular metals. Theoretical predictions are then verified by existing experimental results. Optimal design is subsequently performed to seek for optimal distributions of the geometrical parameters in graded semi-open cellular metals by using the same optimizing method as that for graded sintered fibrous materials.

The influence of surface roughness such as short fibers on sound propagation in cylindrical micro pores is investigated. Based on the calculated velocity and temperature fields, a theoretical model is built to calculate the sound absorption of composite micro pores with periodical fibrous surface roughness. Finite element models are developed to validate the theoretical model, with good agreements achieved. It is found that surface roughness can dramatically increase the sound energy consumed by viscous effect and decrease the sound energy consumed by thermal effect, resulting enlarged sound absorption in a wide frequency range.

Numerical and experimental investigations are performed to evaluate the low frequency acoustic properties of corrugated sandwich panels with different perforation configurations, including perforations in one of the face plates, in the corrugated core, and in both the face plate and the corrugated core. Finite element (FE) models are set up by considering acoustic-structure interactions and viscous and thermal energy dissipations inside the perforations. The FE calculations are validated by comparing with measured results. The corrugated sandwich with micro perforated pores in its face plate have better SAC and STL than classical corrugated sandwich panels, which is attributed to the acoustical resonance. In additions, for a corrugated sandwich with uniform perforations, the acoustical resonance frequencies and bandwidth in its SAC and STL curves decrease with increasing pore diameter and decreasing perforation ratio. Non-uniform perforation diameters and perforation ratios result in larger bandwidth and lower acoustical resonance frequencies relative to the case of uniform perforations.

An analytical model is presented to calculate both the STL and SAC of honeycomb sandwich panels with perforated faceplates. The displacements of the two faceplates are assumed identical at frequencies below the faceplate resonance frequency. Influences of core configuration are investigated by comparing different honeycomb core designs. Finite element (FE) models and existing experimental results are subsequently applied to validate the proposed analytical model. Whereafter, parametric surveys, including the influences of perforation ratio, pore size and core configuration on STL and SAC, are conducted based on the analytical model. It is found that honeycomb sandwiches with perforated faceplates result in high SAC at low frequencies, which in turn enlarges the STL. Moreover, sandwich panels with triangular cores are shown to have the lowest peak frequency in the STL and SAC curves compared with the other kinds of sandwich panels having the same effective mass and perforations.

Generally, the above investigated perforated sandwich structures have narrow bandwidth at low frequencies, while porous materials are wide bandwidth sound absorbing materials. Therefore,

Porous materials are filled into the cores of the perforated honeycomb sandwich panels and corrugated sandwich panels to enlargement the bandwidth of sound absorption. The porous materials and perforated sandwich panel composited structures are found numerically to improve the bandwidth of the perforated sandwich panels greatly. Besides, the sound absorption of the composite structures is also determined by the filling way of porous materials. The best sound absorption is obtained when the porous materials are only filled in the low half part of the corrugated cores.

9.2 Future work

Based on the findings of the dissertation, future work would be worth while in these areas:

（1）The surface roughness is found to improve the acoustic properties of the micro pores over a wide frequency range by enlarging the viscous dissipation. The shapes and distributions of the roughness elements can be further studied and optimized to achieve better sound absorption.

（2）The proposed theory for micro pores with surface roughness is based on the assumption that the thickness of the pores is much larger than their diameter. The assumption fails when the surface roughness is added to pores with smaller thickness, such as MPPs. It is interesting and meaningful to study the influences of surface roughness on the acoustic properties of pores of finite thickness.

（3）Investigations of the microperforated sandwich panels are proposed at frequencies lower than the structural resonance frequencies. To get a more comprehensive understanding of the microperforated sandwich panels, the acoustic properties at higher frequencies can be considered in the future work.

（4）It can be seen from the findings that the micro perforations can improve the STL and SAC of sandwich panels at low frequencies for normal incident sound in the dissertation. Normally, sandwich panels subjected to oblique incident waves might have quite different acoustic properties from that with normal incident sound wave. The acoustic properties of perforated sandwich panels under oblique and field incidences should be further explored.

（5）Composite structures of micro perforations and honeycomb and corrugated sandwich panels are studied in the dissertation. Actually, the micro perforation and sandwich panel combination technology can be applied to other sandwich panels according to the demanding of applications. It is useful to consider the acoustic properties of various sandwich panels, perforated structures and porous materials combinations.

Acknowledgement

I would like to express my gratitude to all those who helped me during the writing of this thesis.

My deepest gratitude goes first and foremost to my supervisors, Prof. Tianjian Lu, Prof. Fengxian Xin, Prof. Marie-Annick Galland, and Prof. Mohamed Ichchou, for their meticulous guidance. Prof. Lu guided my research throughout my PhD study, I benefit a lot from his rigorous attitude towards the research and plenty of innovative ideas. Whenever I encountered difficulties and lacked inspiration for my research, Prof. Lu's guidance helped me out. Prof. Xin is a conscientious supervisor. He taught me useful knowledge for the research and many skills for publishing research results. Prof. Galland and Prof. Ichchou also gave me valuable suggestions for my research and answered my questions patiently. Their advices made me focused on the quality of the research which is closely related to the details.

I would also like to thank Ms Qingye Li and Prof. Marie-Annick Galland for their help of administration affairs during my PhD study.

I'm also indebted to all the professors, technicians and students that helped me during my research in the labs of MOE Key Laboratory for Multifunctional Materials and Structures of Xi'an Jiaotong University, Laboratoire de Tribologie et Dynamique des Systèmes and Centre d'Acoustique of Ecole centrale de Lyon, including Prof. Xiaohu Yang, Prof. Olivier Bareille, Shuwei Ren, Yufan Tang, Alexandre Azouzi, Pierre Roland, et al.

Last, I want to express my thanks to my family, especially my husband, Wenming Wei. He is always there for me and really supportive for my research.

References

[1] Groby J-P, Dazel O, De Ryck L, et al. Acoustic characterization of graded porous materials under the rigid frame approximation[C]. Montreal: Proceedings of Meetings on Acoustics, 2013: 065009.

[2] Tang H, Zhu J, Wang J, et al. Sound absorption characters of metal fibrous porous material[C]. Montreal: Proceedings of the Fifth International Conference on Porous Metals and Metallic Foams, DEStech Publications, Inc, 2008: 181.

[3] Huang K, Yang D, He S, et al. Acoustic absorption properties of open-cell Al alloy foams with graded pore size[J]. Journal of Physics D: Applied Physics, 2011, 44 (36): 365405.

[4] Dupont T, Pavic G, Laulagnet B. Acoustic properties of lightweight micro-perforated plate systems[J]. Acta Acustica united with Acustica, 2003, 89 (2): 201-212.

[5] Bravo T, Maury C, Pinhède C. Sound absorption and transmission through flexible micro-perforated panels backed by an air layer and a thin plate[J]. Journal of the Acoustical Society of America, 2012, 131 (5): 3853-3863.

[6] Bravo T, Maury C, Pinhede C. Enhancing sound absorption and transmission through flexible multi-layer micro-perforated structures[J]. Journal of the Acoustical Society of America, 2013, 134 (5): 3663-3673.

[7] Toyoda M, Takahashi D. Sound transmission through a microperforated-panel structure with subdivided air cavities[J]. Journal of the Acoustical Society of America, 2008, 124 (6): 3594-3603.

[8] Arenas JP, Crocker MJ. Recent trends in porous sound-absorbing materials[J]. Sound & vibration, 2010, 44 (7): 12-18.

[9] Biot MA. Theory of propagation of elastic waves in a fluid-saturated porous solid. I. Low-frequency range[J]. Journal of the Acoustical Society of America, 1956, 28 (2): 168-178.

[10] Biot MA. Theory of propagation of elastic waves in a fluid-saturated porous solid. II. Higher frequency range[J]. Journal of the Acoustical Society of America, 1956, 28 (2): 179-191.

[11] Biot MA. Generalized theory of acoustic propagation in porous dissipative media[J]. Journal of the Acoustical Society of America, 1962, 34 (9A): 1254-1264.

[12] Biot MA. Mechanics of deformation and acoustic propagation in porous media[J]. Journal of applied physics, 1962, 33 (4): 1482-1498.

[13] Allard JF, Aknine A, Depollier C. Acoustical properties of partially reticulated foams with high and medium flow resistance[J]. Journal of the Acoustical Society of America, 1986, 79 (6): 1734-1740.

[14] Khurana P, Boeckx L, Lauriks W, et al. A description of transversely isotropic sound absorbing porous materials by transfer matrices[J]. Journal of the Acoustical Society of America, 2009, 125 (2): 915-921.

[15] Atalla N, Panneton R, Debergue P. A mixed displacement-pressure formulation for poroelastic materials[J]. Journal of the Acoustical Society of America, 1998, 104 (3): 1444-1452.

[16] Panneton R, Atalla N. Numerical prediction of sound transmission through finite multilayer systems with poroelastic materials[J]. Journal of the Acoustical Society of America, 1996, 100 (1): 346-354.

[17] Panneton R, Atalla N. An efficient finite element scheme for solving the three-

dimensional poroelasticity problem in acoustics[J]. Journal of the Acoustical Society of America, 1997, 101 (6): 3287-3298.

[18] Sgard FC, Atalla N, Panneton R. A modal reduction technique for the finite element formulation of biot's poroelasticity equations in acoustics applied to multilayered structures[J]. Journal of the Acoustical Society of America, 1998, 103 (5): 2882-2882.

[19] Kang YJ, Bolton JS. Finite element modeling of isotropic elastic porous materials coupled with acoustical finite elements[J]. Journal of the Acoustical Society of America, 1995, 98 (1): 635-643.

[20] Deckers E, Horlin N-E, Vandepitte D, et al. A Wave Based Method for the efficient solution of the 2D poroelastic Biot equations[J]. Computer Methods in Applied Mechanics and Engineering, 2012, 201: 245-262.

[21] Dazel O, Brouard B, Depollier C, et al. An alternative Biot's displacement formulation for porous materials[J]. Journal of the Acoustical Society of America, 2007, 121 (6): 3509-3516.

[22] Bécot F-X, Jaouen L. An alternative Biot's formulation for dissipative porous media with skeleton deformation[J]. Journal of the Acoustical Society of America, 2013, 134 (6): 4801-4807.

[23] Gao K, van Dommelen J, Göransson P, et al. A homogenization approach for characterization of the fluid–solid coupling parameters in Biot's equations for acoustic poroelastic materials[J]. Journal of Sound and Vibration, 2015, 351: 251-267.

[24] Gao K, van Dommelen J, Göransson P, et al. Computational homogenization of sound propagation in a deformable porous material including microscopic viscous-thermal effects[J]. Journal of Sound and Vibration, 2016, 365: 119-133.

[25] Yamamoto T, Maruyama S, Terada K, et al. A generalized macroscopic model for sound-absorbing poroelastic media using the homogenization method[J]. Computer Methods in Applied Mechanics and Engineering, 2011, 200 (1): 251-264.

[26] Voronina N. An empirical model for elastic porous materials[J]. Applied Acoustics, 1998, 55 (1): 67-83.

[27] Voronina N. Comparison between theoretical and empirical models for elastic porous materials[J]. Applied Acoustics, 1999, 58 (3): 255-260.

[28] Allard JF, Atalla N. Propagation of sound in porous media: modelling sound absorbing materials 2e[M]. John Wiley & Sons, 2009.

[29] Delany ME, Bazley EN. Acoustical properties of fibrous absorbent materials[J]. Applied Acoustics, 1970, 3 (2): 105-116.

[30] Miki Y. Acoustical properties of porous materials-Modifications of Delany-Bazley models[J]. Journal of the Acoustical Society of Japan (E), 1990, 11 (1): 19-24.

[31] Komatsu T. Improvement of the Delany-Bazley and Miki models for fibrous sound-absorbing materials[J]. Acoustical science and technology, 2008, 29 (2): 121-129.

[32] Voronina N. An empirical model for rigid-frame porous materials with low porosity[J]. Applied Acoustics, 1999, 58 (3): 295-304.

[33] Voronina N. An empirical model for rigid frame porous materials with high porosity[J]. Applied Acoustics, 1997, 51 (2): 181-198.

[34] Voronina N. Improved empirical model of sound propagation through a fibrous material[J]. Applied Acoustics, 1996, 48 (2): 121-132.

[35] Voronina N. Acoustic properties of fibrous materials[J]. Applied Acoustics, 1994, 42 (2): 165-174.

[36] Narang P. Material parameter selection in polyester fibre insulation for sound transmission and absorption[J]. Applied Acoustics, 1995, 45 (4): 335-358.

[37] Bies DA, Hansen CH. Flow resistance information for acoustical design[J]. Applied

Acoustics, 1980, 13 (5): 357-391.
[38] Stinson MR. The propagation of plane sound waves in narrow and wide circular tubes, and generalization to uniform tubes of arbitrary cross - sectional shape[J]. Journal of the Acoustical Society of America, 1991, 89 (2): 550-558.
[39] Zwikker C, Kosten CW. Sound absorbing materials[M]. Elsevier, 1949: 26-34.
[40] Attenborough K. Acoustical characteristics of rigid fibrous absorbents and granular materials[J]. Journal of the Acoustical Society of America, 1983, 73 (3): 785-799.
[41] Wilson DK. Relaxation-matched modeling of propagation through porous media, including fractal pore structure[J]. Journal of the Acoustical Society of America, 1993, 94 (2): 1136-1145.
[42] Johnson DL, Koplik J, Dashen R. Theory of dynamic permeability and tortuosity in fluid-saturated porous media[J]. Journal of fluid mechanics, 1987, 176: 379-402.
[43] Champoux Y, Allard JF. Dynamic tortuosity and bulk modulus in air - saturated porous media[J]. Journal of applied physics, 1991, 70 (4): 1975-1979.
[44] Tarnow V. Compressibility of air in fibrous materials[J]. Journal of the Acoustical Society of America, 1996, 99 (5): 3010-3017.
[45] Tarnow V. Calculation of the dynamic air flow resistivity of fiber materials[J]. Journal of the Acoustical Society of America, 1997, 102 (3): 1680-1688.
[46] Dupere ID, Dowling AP, Lu TJ. The absorption of sound in cellular foams[C]. ASME 2004 International Mechanical Engineering Congress and Exposition, American Society of Mechanical Engineers, 2004: 123-132.
[47] Dupere ID, Dowling AP, Lu TJ. Optimization of cell structures of cellular materials for acoustic applications[C]. Lisbon: 12th International Congress on Sound and Vibration, 2005: 276-284.
[48] Sun F, Chen H, Wu J, et al. Sound absorbing characteristics of fibrous metal materials at high temperatures[J]. Applied Acoustics, 2010, 71 (3): 221-235.
[49] Kirby R, Cummings A. Prediction of the bulk acoustic properties of fibrous materials at low frequencies[J]. Applied Acoustics, 1999, 56 (2): 101-125.
[50] Dupère ID, Lu TJ, Dowling AP. Microstructural optimization of cellular acoustic materials[J]. Journal of Xi'an Jiaotong University, 2007, 41: 1251-1256. (In Chinese)
[51] Cortis A, Smeulders DM, Guermond JL, et al. Influence of pore roughness on high-frequency permeability[J]. Physics of Fluids, 2003, 15 (6): 1766-1775.
[52] Achdou Y, Avellaneda M. Influence of pore roughness and pore - size dispersion in estimating the permeability of a porous medium from electrical measurements[J]. Physics of Fluids A: Fluid Dynamics, 1992, 4 (12): 2651-2673.
[53] Ren Y, Wang K, Zhu B, et al. Synthesis of ZnO micro-rods on the cell walls of open celled Al foam and their effect on the sound absorption behavior[J]. Materials Letters, 2013, 91: 242-244.
[54] Sakagami K, Takahashi D, Gen H, et al. Acoustic properties of an infinite elastic plate with a back cavity[J]. Acta Acustica united with Acustica, 1993, 78 (5): 288-295.
[55] Sakagami K, Gen H, Morimoto M, et al. Acoustic properties of an infinite elastic plate backed by multiple layers[J]. Acta Acustica united with Acustica, 1996, 82 (1): 45-53.
[56] Sakagami K, Kiyama M, Morimoto M, et al. Sound absorption of a cavity-backed membrane: a step towards design method for membrane-type absorbers[J]. Applied Acoustics, 1996, 49 (3): 237-247.
[57] Ford R, McCormick M. Panel sound absorbers[J]. Journal of Sound and Vibration, 1969, 10 (3): 411-423.
[58] Arenas JP, Ugarte F. A note on a circular panel sound absorber with an elastic boundary condition[J]. Applied Acoustics, 2016, 114: 10-17.

[59] Thomas Jr W, Hurst CJ. Acoustic performance of a stretched membrane and porous blanket combination[J]. Journal of the Acoustical Society of America, 1976, 59 (5): 1071-1076.
[60] Wang C, Han J, Huang L. Optimization of a clamped plate silencer[J]. Journal of the Acoustical Society of America, 2007, 121 (2): 949-960.
[61] Mechel FP. Panel absorber[J]. Journal of Sound and Vibration, 2001, 248 (1): 43-70.
[62] Oldfield R. Improved membrane absorbers[D]. The University of Salford, 2006.
[63] Morse PM, Ingard KU. Theoretical acoustics[M]. Princeton university press, 1968.
[64] Ingard U. On the theory and design of acoustic resonators[J]. Journal of the Acoustical Society of America, 1953, 25 (6): 1037-1061.
[65] Ih J-G. On the inertial end correction of resonators[J]. Acta Acustica united with Acustica, 1993, 78 (1): 1-15.
[66] Ingard U. The near field of a Helmholtz resonator exposed to a plane wave[J]. Journal of the Acoustical Society of America, 1953, 25 (6): 1062-1067.
[67] Panton RL, Miller JM. Resonant frequencies of cylindrical Helmholtz resonators[J]. Journal of the Acoustical Society of America, 1975, 57 (6): 1533-1535.
[68] Alster M. Improved calculation of resonant frequencies of Helmholtz resonators[J]. Journal of Sound and Vibration, 1972, 24 (1): 63-85.
[69] Chanaud R. Effects of geometry on the resonance frequency of Helmholtz resonators[J]. Journal of Sound and Vibration, 1994, 178 (3): 337-348.
[70] Chanaud R. Effects of geometry on the resonance frequency of Helmholtz resonators, part II[J]. Journal of Sound and Vibration, 1997, 204 (5): 829-834.
[71] Tang S. On Helmholtz resonators with tapered necks[J]. Journal of Sound and Vibration, 2005, 279 (3): 1085-1096.
[72] Li D, Vipperman JS. On the design of long T-shaped acoustic resonators[J]. Journal of the Acoustical Society of America, 2004, 116 (5): 2785-2792.
[73] Li D, Vipperman JS. Noise control of mock-scale ChamberCore payload fairing using integrated acoustic resonators[J]. Journal of spacecraft and rockets, 2006, 43 (4): 877-882.
[74] Li D, Cheng L, Yu G, et al. Noise control in enclosures: Modeling and experiments with T-shaped acoustic resonators[J]. Journal of the Acoustical Society of America, 2007, 122 (5): 2615-2625.
[75] Cai X, Guo Q, Hu G, et al. Ultrathin low-frequency sound absorbing panels based on coplanar spiral tubes or coplanar Helmholtz resonators[J]. Applied Physics Letters, 2014, 105 (12): 121901.
[76] Cai C, Mak C-M, Shi X. An extended neck versus a spiral neck of the Helmholtz resonator[J]. Applied Acoustics, 2017, 115: 74-80.
[77] Lee H, Yang B, Cho H. Noise Reduction Analysis Using Extended Neck of Helmholtz Resonator within Limited Engine Room[J]. International Journal of Applied Engineering Research, 2017, 12 (12): 3444-3447.
[78] Griffin S, Lane SA, Huybrechts S. Coupled Helmholtz resonators for acoustic attenuation[J]. 2001, 123:11-17.
[79] Yasuda T, Wu C, Nakagawa N, et al. Studies on an automobile muffler with the acoustic characteristic of low-pass filter and Helmholtz resonator[J]. Applied Acoustics, 2013, 74 (1): 49-57.
[80] Zhang H, Wei Z, Zhang X, et al. Tunable acoustic filters assisted by coupling vibrations of a flexible Helmholtz resonator and a waveguide[J]. Applied Physics Letters, 2017, 110 (17): 173506.
[81] Chen K, Chen Y, Lin K, et al. The improvement on the transmission loss of a duct by

adding Helmholtz resonators[J]. Applied Acoustics, 1998, 54 (1): 71-82.
[82] Selamet A, Dicky NS, Novak JM. Theoretical, computational and experimental investigation of Helmholtz resonators with fixed volume: lumped versus distributed analysis[J]. Journal of Sound and Vibration, 1995, 187 (2): 358-367.
[83] Zhao X, Cai L, Yu D, et al. A low frequency acoustic insulator by using the acoustic metasurface to a Helmholtz resonator[J]. AIP Advances, 2017, 7 (6): 065211.
[84] Maa D-Y. Theory and design of microperforated panel sound-absorbing constructions[J]. Scientia Sinica, 1975, 18 (1): 55-71. (In Chinese)
[85] Maa D-Y. Potential of microperforated panel absorber[J]. Journal of the Acoustical Society of America, 1998, 104 (5): 2861-2866.
[86] Atalla N, Sgard F. Modeling of perforated plates and screens using rigid frame porous models[J]. Journal of Sound and Vibration, 2007, 303 (1): 195-208.
[87] Rao KN, Munjal M. Experimental evaluation of impedance of perforates with grazing flow[J]. Journal of Sound and Vibration, 1986, 108 (2): 283-295.
[88] Lee D, Kwon Y. Estimation of the absorption performance of multiple layer perforated panel systems by transfer matrix method[J]. Journal of Sound and Vibration, 2004, 278 (4): 847-860.
[89] Asdrubali F, Pispola G. Properties of transparent sound-absorbing panels for use in noise barriers[J]. Journal of the Acoustical Society of America, 2007, 121 (1): 214-221.
[90] Li G, Mechefske CK. A comprehensive experimental study of micro-perforated panel acoustic absorbers in MRI scanners[J]. Magnetic Resonance Materials in Physics, Biology and Medicine, 2010, 23 (3): 177-185.
[91] Sakagami K, Morimoto M, Yairi M. Application of microperforated panel absorbers to room interior surfaces[J]. International Journal of Acoustics and Vibration, 2008, 13 (3): 120-124.
[92] Sakagami K, Morimoto M, Yairi M. A note on the effect of vibration of a microperforated panel on its sound absorption characteristics[J]. Acoustical science and technology, 2005, 26 (2): 204-207.
[93] Kang J, Fuchs HV. Predicting the absorption of open weave textiles and micro-perforated membranes backed by an air space[J]. Journal of Sound and Vibration, 1999, 220 (5): 905-920.
[94] Sakagami K, Morimoto M, Yairi M. A note on the relationship between the sound absorption by microperforated panels and panel/membrane-type absorbers[J]. Applied Acoustics, 2009, 70 (8): 1131-1136.
[95] Toyoda M, Mu RL, Takahashi D. Relationship between Helmholtz-resonance absorption and panel-type absorption in finite flexible microperforated-panel absorbers[J]. Applied Acoustics, 2010, 71 (4): 315-320.
[96] Lee Y, Lee E, Ng C. Sound absorption of a finite flexible micro-perforated panel backed by an air cavity[J]. Journal of Sound and Vibration, 2005, 287 (1): 227-243.
[97] Lee Y, Lee E. Widening the sound absorption bandwidths of flexible micro-perforated curved absorbers using structural and acoustic resonances[J]. International Journal of Mechanical Sciences, 2007, 49 (8): 925-934.
[98] London A. Transmission of reverberant sound through double walls[J]. Journal of the Acoustical Society of America, 1950, 22 (2): 270-279.
[99] Antonio J, Tadeu A, Godinho L. Analytical evaluation of the acoustic insulation provided by double infinite walls[J]. Journal of Sound and Vibration, 2003, 263 (1): 113-129.
[100] Chazot J-D, Guyader J-L. Prediction of transmission loss of double panels with a patch-mobility method[J]. Journal of the Acoustical Society of America, 2007, 121 (1): 267-

278.
[101] Wang T, Li S, Rajaram S, et al. Predicting the Sound Transmission Loss of Sandwich Panels by Statistical Energy Analysis Approach[J]. Journal of Vibration and Acoustics, 2010, 132 (1): 011004.
[102] Bolton JS, Green ER. Normal incidence sound transmission through double-panel systems lined with relatively stiff, partially reticulated polyurethane foam[J]. Applied Acoustics, 1993, 39 (1-2): 23-51.
[103] Bolton JS, Shiau N-M, Kang Y. Sound transmission through multi-panel structures lined with elastic porous materials[J]. Journal of Sound and Vibration, 1996, 191 (3): 317-347.
[104] Kang YJ, Bolton JS. A finite element model for sound transmission through foam-lined double-panel structures[J]. Journal of the Acoustical Society of America, 1996, 99 (5): 2755-2765.
[105] Liu Y, Daudin C. Analytical modelling of sound transmission through finite clamped double-wall sandwich panels lined with poroelastic materials[J]. Composite Structures, 2017, 172: 359-373.
[106] Liu Y, He C. Diffuse field sound transmission through sandwich composite cylindrical shells with poroelastic core and external mean flow[J]. Composite Structures, 2016, 135: 383-396.
[107] Chazot J-D, Guyader J-L. Transmission loss of double panels filled with porogranular materials[J]. Journal of the Acoustical Society of America, 2009, 126 (6): 3040-3048.
[108] Doutres O, Atalla N. Acoustic contributions of a sound absorbing blanket placed in a double panel structure: Absorption versus transmission[J]. Journal of the Acoustical Society of America, 2010, 128 (2): 664-671.
[109] Zielinski TG, Galland M-A, Ichchou MN. Fully coupled finite-element modeling of active sandwich panels with poroelastic core[J]. Journal of Vibration and Acoustics, 2012, 134 (2): 021007.
[110] Hu Y, Galland M-A, Chen K. Acoustic transmission performance of double-wall active sound packages in a tube: numerical/experimental validations[J]. Applied Acoustics, 2012, 73 (4): 323-337.
[111] Mead D. Wave propagation in continuous periodic structures: research contributions from Southampton, 1964-1995[J]. Journal of Sound and Vibration, 1996, 190 (3): 495-524.
[112] Wang J, Lu TJ, Woodhouse J, et al. Sound transmission through lightweight double-leaf partitions: theoretical modelling[J]. Journal of Sound and Vibration, 2005, 286 (4): 817-847.
[113] Smith RS. Sound transmission through lightweight parallel plates[D]. Edinburgh: Heriot-Watt University, 1997.
[114] Craik RM, Smith RS. Sound transmission through lightweight parallel plates. Part II: structure-borne sound[J]. Applied Acoustics, 2000, 61 (2): 247-269.
[115] Xin FX, Lu TJ. Sound radiation of orthogonally rib-stiffened sandwich structures with cavity absorption[J]. Composites Science and Technology, 2010, 70 (15): 2198-2206.
[116] Shen C, Xin FX, Cheng L, et al. Sound radiation of orthogonally stiffened laminated composite plates under airborne and structure borne excitations[J]. Composites Science and Technology, 2013, 84: 51-57.
[117] Shen C, Xin FX, Lu TJ. Sound transmission across composite laminate sandwiches: Influence of orthogonal stiffeners and laminate layup[J]. Composite Structures, 2016, 143: 310-316.
[118] Wang T, Sokolinsky VS, Rajaram S, et al. Assessment of sandwich models for the prediction of sound transmission loss in unidirectional sandwich panels[J]. Applied

Acoustics, 2005, 66 (3): 245-262.
[119] Zhou R, Crocker MJ. Sound transmission loss of foam-filled honeycomb sandwich panels using statistical energy analysis and theoretical and measured dynamic properties[J]. Journal of Sound and Vibration, 2010, 329 (6): 673-686.
[120] Tang YY, Robinson JH, Silcox RJ. Sound transmission through a cylindrical sandwich shell with honeycomb core[C], Reno: 34th AIAA Aerospace Science Meeting and Exhibit, AIAA-96-0877, 1996: 1-10.
[121] Jung J-D, Hong S-Y, Song J-H, et al. A study on transmission loss characteristics of honeycomb panel for offshore structures[J]. Journal of Applied Mathematics and Physics, 2015, 3: 172-176.
[122] Griese D, Summers JD, Thompson L. The effect of honeycomb core geometry on the sound transmission performance of sandwich panels[J]. Journal of Vibration and Acoustics, 2015, 137 (2): 021011.
[123] Rajaram S, Wang T, Nutt S. Sound transmission loss of honeycomb sandwich panels[J]. Noise Control Engineering Journal, 2006, 54 (2): 106-115.
[124] Rajarama S, Nutt S. Measurement of sound transmission losses of honeycomb partitions with added gas layers[J]. Noise Control Engineering Journal, 2006, 54 (2): 101-105.
[125] Shen C, Xin FX, Lu TJ. Theoretical model for sound transmission through finite sandwich structures with corrugated core[J]. International Journal of Non-Linear Mechanics, 2012, 47 (10): 1066-1072.
[126] Xin FX, Lu TJ. Effects of core topology on sound insulation performance of lightweight all-metallic sandwich panels[J]. Materials and Manufacturing Processes, 2011, 26 (9): 1213-1221.
[127] Bartolozzi G, Pierini M, Orrenius U, et al. An equivalent material formulation for sinusoidal corrugated cores of structural sandwich panels[J]. Composite Structures, 2013, 100: 173-185.
[128] Mu RL, Toyoda M, Takahashi D. Sound insulation characteristics of multi-layer structures with a microperforated panel[J]. Applied Acoustics, 2011, 72 (11): 849-855.
[129] Chang BJ, Wang XL, Peng F, et al. Prediction on the sound absorption performance of fibrous porous metals at high sound pressure levels[J]. Technical Acoustics, 2009, 28: 450-453. (In Chinese)
[130] Wu JH, Hu ZP, Zhou H. Sound absorbing property of porous metal materials with high temperature and high sound pressure by turbulence analogy[J]. Journal of Applied Physics, 2013, 113 (19): 194905.
[131] Zhang B, Chen T, Feng K, et al. Sound absorption properties of sintered fibrous metals under high temperature conditions[J]. Journal of Xi’an Jiaotong University, 2008, 42 (11): 1327-1331. (In Chinese)
[132] Umnova O, Tsiklauri D, Venegas R. Effect of boundary slip on the acoustical properties of microfibrous materials[J]. Journal of the Acoustical Society of America, 2009, 126 (4): 1850-1861.
[133] Zhang B, Chen T. Calculation of sound absorption characteristics of porous sintered fiber metal[J]. Applied Acoustics, 2009, 70 (2): 337-346.
[134] Umnova O, Attenborough K, Shin H-C, et al. Deduction of tortuosity and porosity from acoustic reflection and transmission measurements on thick samples of rigid-porous materials[J]. Applied Acoustics, 2005, 66 (6): 607-624.
[135] Liu HL, Hwang WR. Permeability prediction of fibrous porous media with complex 3D architectures[J]. Composites Part A: Applied Science and Manufacturing, 2012, 43 (11): 2030-2038.
[136] Tomadakis MM, Robertson TJ. Viscous permeability of random fiber structures:

comparison of electrical and diffusional estimates with experimental and analytical results[J]. Journal of Composite Materials, 2005, 39 (2): 163-188.
[137] Acoustics determination of sound absorption coefficient and impedance in impedance tubes-Part 2: transfer function method[S]. BS EN ISO 10534-2:1998.
[138] Lu TJ, Chen F, He D. Sound absorption of cellular metals with semiopen cells[J]. Journal of the Acoustical Society of America, 2000, 108 (4): 1697-1709.
[139] Chen F, Zhang A, He D. Control of the degree of pore-opening for porous metals[J]. Journal of Materials Science, 2001, 36 (3): 669-672.
[140] Li Y, Wang X, Wang X, et al. Sound absorption characteristics of aluminum foam with spherical cells[J]. Journal of Applied Physics, 2011, 110 (11): 113525.
[141] Cheng G, He D, Shu G. Underwater sound absorption property of porous aluminum[J]. Colloids and Surfaces A: Physicochemical and Engineering Aspects, 2001, 179 (2): 191-194.
[142] Maa D-Y. Microperforated-panel wideband absorbers[J]. Noise Control Engineering Journal, 1987, 29 (3): 77-84.
[143] Stinson MR, Shaw E. Acoustic impedance of small, circular orifices in thin plates[J]. Journal of the Acoustical Society of America, 1985, 77 (6): 2039-2042.
[144] Bolton JS, Yoo T, Olivieri O. Measurement of normal incidence transmission loss and other acoustical properties of materials placed in a standing wave tube[J]. Bruel and Kjaer Technical Review, 2007, 1: 1-44.
[145] Conner BP, Manogharan GP, Martof AN, et al. Making sense of 3-D printing: Creating a map of additive manufacturing products and services[J]. Additive Manufacturing, 2014, 1: 64-76.
[146] Levy GN, Schindel R, Kruth J-P. Rapid manufacturing and rapid tooling with layer manufacturing (LM) technologies, state of the art and future perspectives[J]. CIRP Annals-Manufacturing Technology, 2003, 52 (2): 589-609.
[147] Vaezi M, Seitz H, Yang S. A review on 3D micro-additive manufacturing technologies[J]. The International Journal of Advanced Manufacturing Technology, 2013, 67 (5-8): 1721-1754.
[148] Guo N, Leu MC. Additive manufacturing: technology, applications and research needs[J]. Frontiers of Mechanical Engineering, 2013, 8 (3): 215-243.
[149] Melchels FP, Domingos MA, Klein TJ, et al. Additive manufacturing of tissues and organs[J]. Progress in Polymer Science, 2012, 37 (8): 1079-1104.
[150] Maa D-Y. General theory and design of microperforated-panel absorbers[J]. Acta Acustica, 1997, 22: 385-393.
[151] Zhang Z, Gu X. The theoretical and application study on a double layer microperforated sound absorption structure[J]. Journal of Sound and Vibration, 1998, 215 (3): 399-405.
[152] Takahashi D. Sound transmission through single plates with absorptive facings: Improved theory and experiment[J]. Journal of the Acoustical Society of America, 1990, 88 (2): 879-882.
[153] Toyoda M, Takahashi D. Reduction of acoustic radiation by impedance control with a perforated absorber system[J]. Journal of Sound and Vibration, 2005, 286 (3): 601-614.
[154] Toyoda M, Tanaka M, Takahashi D. Reduction of acoustic radiation by perforated board and honeycomb layer systems[J]. Applied Acoustics, 2007, 68 (1): 71-85.
[155] Kumar S, Feng L, Orrenius U. Predicting the sound transmission loss of honeycomb panels using the wave propagation approach[J]. Acta Acustica united with Acustica, 2011, 97 (5): 869-876.
[156] Randeberg RT. Perforated panel absorbers with viscous energy dissipation enhanced by orifice design[D]. Trondheim: Norwegian University of Science and Technology, 2000.

Appendix   Summary of the Genetic Algorithm Method

The genetic algorithm (GA) method is composed of eight parts, which can be schematically shown as:

$$\mathrm{GA} = \left(C, E, G_0, N, \Phi, \Gamma, \Psi, T\right) \tag{A1}$$

Here, C is the encoding method of the individual, which mostly adopts the binary coding method as the encoding method to form a string. Then the GA method can be favorably started with a population of strings. E is the fitness evaluation function, whose value decides the probability of individuals contributing to the next generation. G_0 is the initial population, which is generated randomly at first. The number of the population size N usually ranges from 20 to 100. The reproduce operator Φ is produced by creating a roulette wheel, where each string has an assigned proportion to its fitness value. The proportion decides the probability of each string to be selected as parent generation for the next generation, which can be calculated as:

$$P_i = \frac{f_i}{\sum_{i=1}^{m} f_i} \tag{A2}$$

After reproduction, the sixth term Γ represents the crossover operator and proceeds as follows (as schematically illustrated in Fig. A1): first, mated individuals are generated randomly in the mating pool; afterwards a crossing point should be chosen, the codes after which are then exchanged; as a consequence, a new generation can be favorably born. In this process, the probability of the crossover generally ranges from 0.4 to 0.99.

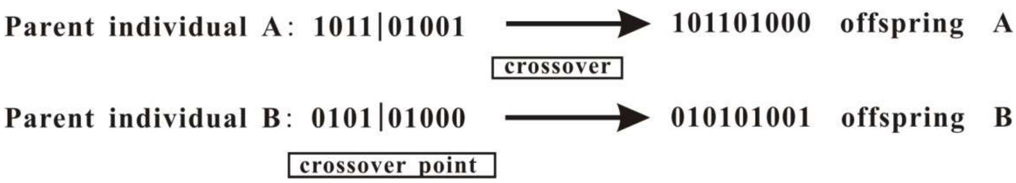

Fig. A1   Schematic diagram of crossover in GA method

The seventh term Ψ denotes the mutation operator, which defines the occurrence of the mutation to follow the mutation probability in the encoding string randomly, and then the codes are changed at the mutation points. When the binary coding method is applied, the mutation simply produces negate at the mutation point. The probability of the mutation generally ranges from 0.0001-0.1. The mutation is depicted in Fig. A2.

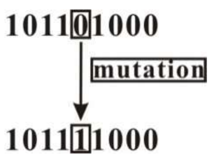

Fig. A2   Schematic diagram of mutation in GA method

The finial term T signifies the terminating conditions. There are many terminating conditions for the GA method in terms of the maximum number of generations, maximum execution time, the fitness value reaching the required threshold and so on.

Publications During PhD Study

Journal paper

[1] **Meng H**, Galland MA, Ichchou M, et al. Small perforations in corrugated sandwich panel significantly enhance low frequency sound absorption and transmission loss[J]. Composite Structures, 2017, 182: 1-11.

[2] **Meng H**, Ren SW, Xin FX, et al. Sound absorption coefficient optimization of gradient sintered metal fiber felts[J]. Science China: Technological Sciences, 2016, 59 (5): 699-708.

[3] **Meng H**, Yang X, Ren SW, et al. Sound propagation in composite micro-tubes with surface-mounted fibrous roughness elements[J]. Composites Science and Technology, 2016, 127: 158-168.

[4] **Meng H**, Ao Q, Ren SW, et al. Anisotropic acoustical properties of sintered fibrous metals[J]. Composites Science and Technology, 2015, 107: 10-17.

[5] **Meng H**, Xin FX, Lu TJ. Sound absorption optimization of graded semi-open cellular metals by adopting the genetic algorithm method[J]. Journal of Vibration and Acoustics, 2014, 136 (6): 061007.

[6] **Meng H**, Ao Q, Tang HP, et al. Dynamic flow resistivity based model for sound absorption of multi-layer sintered fibrous metals[J]. Science China Technological Sciences, 2014, 57 (11): 2096-2105.

[7] **Meng H**, Xin FX, Lu TJ. External mean flow effects on sound transmission through acoustic absorptive sandwich structure[J]. AIAA Journal, 2012, 50 (10): 2268-2276.

[8] **Meng H**, Xin FX, Lu TJ. Acoustical properties of honeycomb structures filled with fibrous absorptive materials[J]. Scientia Sinica: Physica, Mechanica & Astronomica, 2014, 44 (6): 599-609. (In Chinese)

[9] **Meng H**, Galland MA, Ichchou M, et al. On the low frequency sound absorption and transmission loss of multifunctional honeycomb sandwich panels with micro-perforated face plates: modelling and parametric survey, 2017, Composites Science and Technology (under review)

[10] Ren SW, **Meng H**, Xin FX, et al. Ultrathin multi-slit metamaterial as excellent sound absorber: Influence of micro-structure[J]. Journal of Applied Physics, 2016, 119 (1): 014901.

[11] Tang YF, Ren SW, **Meng H**, et al. Hybrid acoustic metamaterial as super absorber for broadband low-frequency sound[J]. Scientific Reports, 2017, 7: 43340.

[12] Ren SW, Ao Q, **Meng H**, et al. A semi-analytical model for sound propagation in sintered fiber metals[J]. Composites Part B: Engineering, 2017, 126: 17-26.

[13] Ye CZ, **Meng H**, Xin F X, et al. Transfer function method for acoustic property study of underwater anechoic layer[J]. Chinese Journal of Theoretical and Applied Mechanics, 2016, 48(1): 213-224. (In Chinese)

[14] Ren SW, **Meng H**, Xin FX, et al. Vibration analysis of simply supported curved sandwich

panels with square honeycomb cores[J]. Journal of Xi’an Jiaotong University, 2015, 49(3): 129-135. (In Chinese)

Conference paper

[1] **Meng H**, Ren S W, Xin FX, et al. Acoustic anisotropy of sintered fibrous metals [c]. 23rd International Conference on Noise and Fluctuations. Xi’an: 2015.
[2] **Meng H**, Xin FX, and Lu TJ. Theoretical investigation of sintered metal fibers [c]. Chinese Congress of Theoretical and Applied Mechanics-2013. Xi’an: 2013. (In Chinese)
[3] **Meng H**, Xin FX, and Lu TJ. Influence of mean flow on transmission loss of sandwich structure with porous material core [c]. The 23rd International Congress of Theoretical and Applied Mechanics. Beijing: 2012.
[4] Ren SW, **Meng H**, Xin FX and Lu TJ. Sound absorption of thin multi-slit structures[c]. 23rd International Conference on Noise and Fluctuations. Xi’an: 2015.
[5] Xin FX, **Meng H**, Shen C, et al. Noise radiation of periodical sandwich structures[c]. The 23rd International Congress of Theoretical and Applied Mechanics, Beijing: 2012..
[6] Ye CZ, **Meng H**, Xin FX, et al. Noise Reduction Analysis of an Underwater Anechoic Layer[c. 23rd International Conference on Noise and Fluctuations. Xi’an: 2015.